The Dissertation Committee for Jingsi Li certifies that this is the approved version of the following dissertation:

Distributed Feedback Lasers and Integrated Laser Arrays for Wavelength-Division Multiplexing Systems

Committee:

Julian Cheng, Supervisor

Seth R. Bank

Mikhail A. Belkin

Edward T. Yu

Chan-Long Shieh

Distributed Feedback Lasers and Integrated Laser Arrays for Wavelength-Division Multiplexing Systems

by

Jingsi Li, B.S., B.Eco., M.S.E., M.E.

Dissertation

Presented to the Faculty of the Graduate School of

The University of Texas at Austin

in Partial Fulfillment

of the Requirements

for the Degree of

Doctor of Philosophy

The University of Texas at Austin

May, 2014

Dedication

I dedicate this dissertation to my wife, Heng Zhong, my mother, Liping Wu, and my father, Qianyin Li. Their constant support and endless love make everything happen.

I also dedicate this dissertation to my late grandparents, Shuxian Wang and Qingyuan Wu.

Acknowledgements

I am deeply indebted to my adviser Professor Julian Cheng. This work was possible only because of the unconditional support from him. He is the most knowledgeable person I have ever meet in my life. Discussions with him are always very helpful and fruitful. Advice and encouragement from him is a most important part of the successful completion of my work.

I would like to thank facility members and my friends in Microelectronics Research Center, the University of Texas at Austin. The advanced facility and well equipped cleanroom here offered me great freedom in realizing whatever I wanted.

I am greatly thankful to my family for their love and support. My parents are always the most strong backing in my life. Married to my wife is the most beautiful thing happened in my life.

Jingsi Li

Austin, Texas

February, 2014

Distributed Feedback Lasers and Integrated Laser Arrays for Wavelength-Division Multiplexing Systems

Jingsi Li, Ph.D.

The University of Texas at Austin, 2014

Supervisor: Julian Cheng

Distributed Feedback (DFB) lasers and integrated laser arrays are of great importance in Wavelength-Division Multiplexing (WDM) systems in fiber optic communication systems. High-performance, low-cost DFB lasers and laser arrays are highly desirable for applications in intra-datacenter transport and in local access networks. This dissertation is focused on the design, fabrication and achievement of high-performance, low-cost DFB Lasers and Integrated DFB Arrays for WDM Systems. It investigates the use of a novel sampled grating approach, called the equivalent phase shift method, to achieve integrated DFB laser arrays with single-mode lasing at uniformly-spaced and precisely-positioned wavelengths. First, laterally-Coupled DFB (LC-DFB) lasers with first-order sidewall gratings are realized, with gratings fabricated by optical interference lithography instead of e-beam. Then, LC-DFB lasers and LC-DFB laser arrays with sampled gratings and equivalent phase shifts are proposed, numerically analyzed and experimentally demonstrated. Each LC-DFB laser with an equivalent quarter-wave phase

shift is shown to lase at the pre-specified wavelength in a single longitudinal mode, with good side-mode suppression ratio (SMSR) over a very wide range of injection currents. Integrated LC-DFB laser arrays with five uniformly-spaced wavelength channels are demonstrated, in close agreement with the design. For better performance, buried heterostructure (BH)-DFB laser and laser arrays are also demonstrated using the same sampled-grating technology. A 6-wavelenth laser array with a 300 μm cavity length and a 8-wavelength laser array with 250 μm cavity length are successively demonstrated, each showing precisely positioned lasing wavelengths, good SMSR, and uniformly good lasing characteristics under a wide range of operating currents and temperatures. Finally, it is demonstrated that the wavelength of a monolithic WDM laser array can be continuously tuned over a very wide wavelength range of nearly 40 nm. The proposed method offers a practical and cost-effective solution for the manufacture of high-performance, monolithic multi-wavelength DFB laser arrays as well as widely wavelength-tunable DFB lasers for integrated WDM systems.

Table of Contents

List of Tables

List of Figures

Chapter 1: Introduction

1.1 Photonic Integrated Circuits and WDM Systems.

The photonic integrated circuits (PIC) concept was first introduced by Stewart E. Miller in 1969 [1]. However, the first commercial application with ~100 devices was achieved by Infinera around 2005 [2], which is 36 years later [3]. The Moore's law for CMOS ICs and PICs is shown in Figure 1. One of the key differences between progress in electronic and photonic integration is that active photonic devices are based binary, ternary and quaternary materials that are much harder to control than Silicon [3]. Therefore, great efforts have been put into the study of active devices and their integration with other optical components. Laser and laser arrays, as active devices converting electrical signal into optical signal, play an important role in optical communication systems, which act as the heart and engine of the whole system. Also, in optical fiber communication systems, the wavelength (or frequency) spectrum offers an additional degree of freedom in transmitting multiple signals simultaneously through the fiber channel, giving rise to wavelength-division multiplexing (WDM) technology [4], which multiplexes optical carrier signals with different wavelengths onto a single optical fiber without interference with each other. WDM technology is widely used in long-haul communication. For fiber optic telecommunication systems, two typical wavelength ranges are used: 1.3 μm and 1.55 μm. The former for their lower dispersion, the latter for the lowest loss in optical fiber, respectively [5].

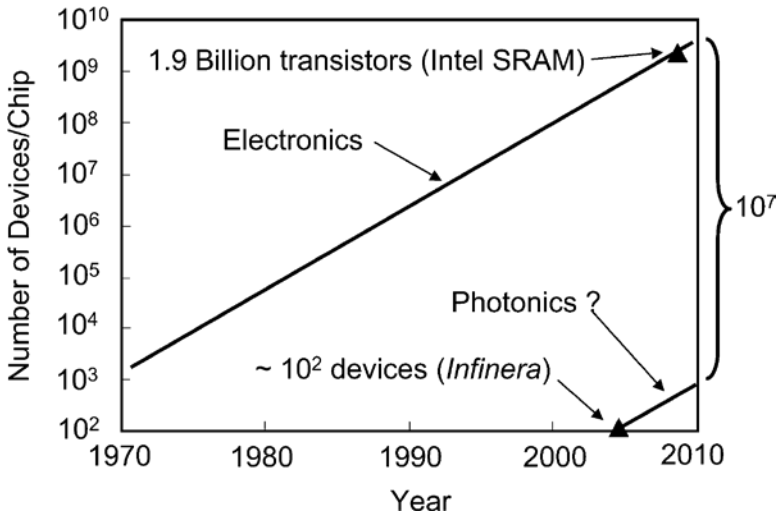

Figure 1. Moore's Law for CMOS ICs and PICs. (Adopted from [3].)

According to International Telecommunication Union (ITU) Telecommunication (ITU-T) Standardization [6], Coarse WDM (CWDM) systems use uncooled lasers, relaxed laser wavelength selection tolerances, and wide passband filters. The nominal central wavelengths range from 1271 nm to 1611 nm with a spacing of 20 nm [6] (18 channels in total, Figure 2 [7]). Due to the optical gain properties of the semiconductor materials, CWDM laser arrays with 4 or more channels (whose wavelength span is 60 nm or more) are very hard to be integrated monolithically using the same gain profile. One solution is to use selective area growth (SAG). Using different width of the covering mask (usually SiO_2), the growth rate and composition of the III-V materials are different, resulting in different gain peak wavelengths [8]. However, the maximum number of CWDM wavelengths that can be integrated is very limited due to the large wavelength spacing (20 nm). Therefore, in most commercial CWDM products, the lasers are still discrete devices,

which are selected from different wafers and packaged together. Packaging cost represents a large part of the total cost of fiber optic devices.

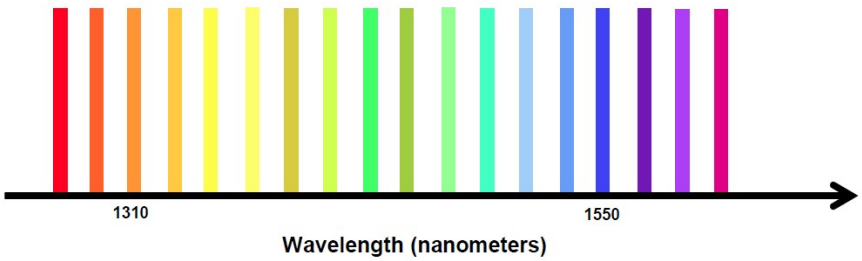

Figure 2. CWDM Wavelengths. 18 channels from 1271 nm to 1611 nm with 20 nm channel spacing. (Adopted from [7].)

Dense WDM (DWDM) has a narrower channel spacing than CWDM, with frequency grid spacings of 12.5 GHz, 25 GHz, 50 GHz, and 100 GHz [9]. (An illustration of DWDM systems is shown in Figure 3, adopted from [7]). The approximate wavelength difference for these four DWDM grids are 0.1 nm, 0.2 nm, 0.4 nm and 0.8nm at λ = 1550 nm, and are 0.07 nm, 0.14 nm, 0.28nm and 0.57 nm at λ = 1310 nm. To accurately control the wavelength of the DWDM system to an accuracy at the picometer level is very difficult. For 25 GHz / 50 GHz / 100 GHz channel spacings, the allowable frequency deviations are 1.25 GHz / 7.5 GHz / 20 GHz, respectively, corresponding to a wavelength deviation of ~10 pm / ~ 60 pm / ~160 pm at 1550nm, and ~7 pm / ~40 pm / ~120 pm at 1310 nm [10]. The wavelength shifts due to changes of laser current and case temperature are acceptable for a 100 GHz channel spacing. However, for 50 GHz channel spacing, additional efforts are necessary to lock in the wavelength [10], such as a wavelength monitor (which includes

a Fabry-Perot (FP) etalon and a photodiode). For 25 GHz spacing or below, a FP etalon is not even easy to integrate. Methods using a prism as beam splitter have been reported [11].

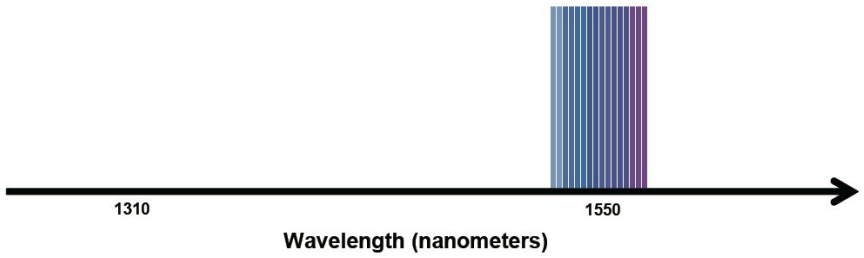

Figure 3. An example of DWDM system wavelength spacing. (Adapted from [7].)

A WDM system with channel spacing smaller than for CWDM, but larger than for a DWDM system are also useful. On one hand, a channel spacing smaller than CWDM can squeeze more channels into the same package for a higher aggregate transmission data rate. On the other hand, a channel spacing larger than DWDM systems does not require complicated technology for wavelength control, therefore reducing the cost substantially. An example of this type of WDM system is one with a 800 GHz channel spacing. In some places, 400 GHz, 600 GHz and 800 GHz channel spacings are called LAN WDM [12]. The passband is set to half of the inter-channel spacing and is centered at the nominal wavelength [12]. The 400 GHz / 600 GHz / 800 GHz channel spacings correspond to a wavelength separation of 3.2 nm / 4.8 nm / 6.4 nm at an operation wavelength of 1550 nm, and 2.3 nm / 3.5 nm / 4.6 nm at an operation wavelength of 1310 nm, respectively. To control wavelength at the nanometer level is much easier compared to the picometer level. Some commercially available 100 Gb/s and 40 Gb/s transceivers use 4 by 25 Gb/s and 4

by 10 Gb/s LAN-WDM systems, respectively, with 4 lasers operating at a relatively large wavelength spacing compared to DWDM.

Figure 4 [13] is an illustration of a WDM system. This WDM system uses lasers with different wavelengths, which are multiplexed together and coupled into a single fiber. After transmission, a demultiplexer is used to separate the wavelengths and sent different receivers.

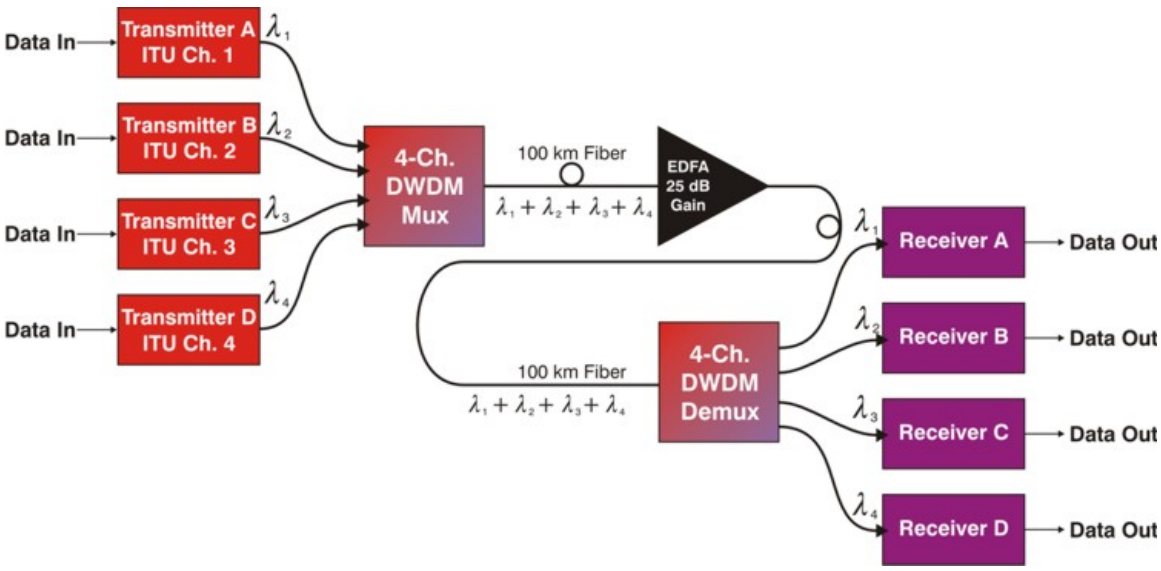

Figure 4. Illustration of WDM system networks. (adopted from [13])

1.2 TUNABLE LASERS

Tunable lasers are lasers whose wavelength can be adjusted in a controlled manner. In fiber optic communications, tunable lasers are of great interest for many reasons [14-16], such as wavelength-routed networks in combination with tunable filters, wavelength conversion, photonic switching, reconfigurable optical add-drop multiplexers (ROADMs), etc. One way to continuously tune the wavelength is to use a laser array, with coarse

wavelength tuning achieved by switching on the appropriate laser channel and fine tuning the wavelength by adjusting the temperature [17]. A WDM laser array design with the right wavelength spacing and channel count can be a candidate for a wavelength-tunable laser, making the study of an integrated WDM laser array more meaningful.

1.3 SEMICONDUCTOR LASERS

Semiconductor lasers are ideal candidates for optical fiber communications due to their small footprint, low power dissipation, long lifetime, etc. There are mainly three types of semiconductor lasers used in optical fiber communication systems: Fabry-Perot (FP) lasers, Vertical-cavity surface-emitting lasers (VCSEL) and Distributed Feedback (DFB) Lasers.

Semiconductor lasers for fiber optical communications primarily use the Indium Phosphide (InP) or Gallium Arsenide (GaAs) materials system, depending on the needed wavelengths, which means the lasers are based on InP or GaAs substrate with mostly matched epi-structure.

850 nm and 980 nm lasers (usually VCSELs) are usually ternary compound semiconductor devices, normally grown on GaAs substrate and with GaAs/AlGaAs and GaAs/InGaAs active regions, respectively (green and red dash lines in Figure 5). VCSELs require Distributed Bragg Reflector (DBR) mirrors. For 850 nm and 980 nm VCSELs, the DBR mirrors are comprised of of AlGaAs/GaAs material, which provides a large index contrast (e.g. 3.1 to 3.65). Therefore, fewer DBR pairs are needed to provide the very high reflection (strong optical feedback) that leads to lasing.

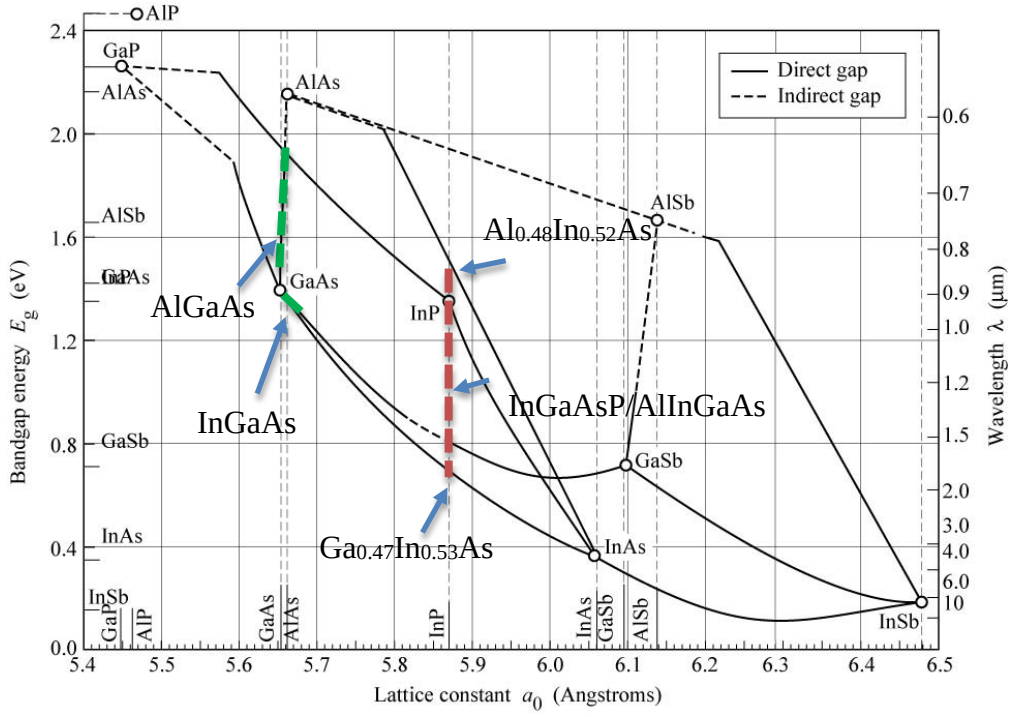

Figure 5. Bandgap energy and lattice constant of various III-V semiconductors at room temperature (online source [18] with added notes, originally adopted from Tien, 1988).

VCSELs have many advantages, including low cost, high yield, low power dissipation, on-wafer testing, etc. It is widely used in data communication networks and datacenter networks for short distance transmission. Very low cost gives VCSELs an unique advantage, but VCSELs usually have a lower output power and weaker lateral mode control ability compared to DFB lasers, and are less suitable than DFB lasers for long-haul communications systems.

The 1310 nm and 1550 nm lasers (*e.g.*, FP and DFB lasers) are usually composed of quaternary compound semiconductors grown on an InP substrate, with an InGaAsP or AlInGaAs active region (red dash line in Figure 5). The epi-growth can be done either by

Metalorganic vapor phase epitaxy (MOVPE), or by Molecular beam epitaxy (MBE), both of which are commercially employed.

The InGaAsP/AlInGaAs/InP material systems have a much smaller index contrast (*i.e.*, 3.17 *vs*. 3.4) compared to AlGaAs/GaAs materials systems (2.95 *vs*. 3.5), so this material system is not very suitable for making DBR mirrors for VCSELs due to the large number of DBR pairs needed and the thick mirrors that must be grown.

Al-contained InP lasers (AlInGaAs/InP) have band offset that is 70% in the conduction band and 30% in the valance band. Al-free InP lasers (InGaAsP/InP) have bandgap offset that are 40% in the conduction band and 60% in the valence band [19]. The main material parameter controlling current leakage is the conduction band offset due to the light weight of the electron effective mass. A larger bandgap offset in the conduction band (ΔE_c) gives rise to the better confinement of electrons. So Al-containing InP lasers can have a better performance at high temperature compared to Al-free InP lasers. But Aluminum also brings about other problems. Due to the aluminum oxidation, Al-containing InP lasers sometimes suffer from sudden failure.

For any WDM system, wavelength selection and wavelength stability is always the key factor. Single mode lasing in both longitudinal and transverse directions is desired. Single longitudinal mode is achievable by means of Bragg reflections (e.g., in distributed feedback (DFB) lasers and distributed Bragg reflector (DBR) lasers). Single transverse mode is usually achieved by controlling the physical dimension (ridge waveguide lasers) or controlling of the index profile of the active region of the device (buried heterostructure lasers).

The FP lasers are edge-emitting lasers which can offer high power and are relatively easy to fabricate compared to DFB lasers. FP lasers operate in a single transverse and lateral mode, which is confined by the ridge waveguide, but due to lack of longitudinal confinement, FP lasers have multiple longitudinal modes. The FP laser therefore suffers from severe chromatic dispersion even in single mode fiber transmission. The wavelength spectrum of a FP laser is usually exceeds 10 nm, so it is not usable in WDM systems due to the lack of longitudinal mode control.

DFB lasers are the predominant optical sources for single-mode optical fiber communication systems, due to their single longitudinal mode lasing operation, compact size, and monolithic integrability, etc.[20-26]. DFB lasers offer the best mode control ability in both longitudinal and transverse directions, as well as high output power, and are the best candidate for WDM systems from the perspective of wavelength selection and transmission distance.

1.4 DISTRIBUTED FEEDBACK LASERS

The wavelength control mechanism for DFB lasers is the wavelength selectivity of distributed Bragg reflections. The photons at the Bragg wavelength are strongly reflected by the coherent reflections from the DFB grating under the phase matched condition. At each index change of the grating, a small amount of light is reflected. The coherent reflection at the phase-matched wavelength gives rise to constructive interference, and produces a large reflection amplitude. The reflections at a non-resonant wavelength is not in-phase and is therefore destructive, making the grating seem “transparent”. Therefore the DFB grating offer a basic mechanism for wavelength selection.

In DFB lasers, light propagation is in-plane with the grating layer. Light can be treated as propagating in one dimension (either going forward or going backward). In a DFB laser, the Bragg wavelength is decided simply by grating pitch and effective refractive index:

$$\lambda_B = 2 \cdot n_{eff} \wedge$$

Eqn. 1

where λ_B is the Bragg wavelength, n_{eff} is the effective refractive index of the grating layer, which is typically around 3.22 for 1.31 μm lasers and 3.2 for 1.55 μm lasers, and Λ is the grating pitch. By adjusting the grating pitch, different Bragg wavelength can be obtained. The grating pitch is typically around 203 nm for 1.31 μm lasers and 242 nm for 1.55 μm lasers. Usually, the grating pitch in a DFB laser is fixed. But sometimes for special needs, the grating pitch can be varied along the laser cavity, leading to a "chirped" grating profile. This dissertation mainly focused on DFB lasers with fixed grating pitch. DFB lasers with chirped gratings are not discussed here.

DFB lasers can be fabricated using a ridge-waveguide (RWG) structure (Figure 6) [20, 21, 25, 26] with the grating layer embedded into semiconductor layers. The grating layer can be either below or above the active regions. In the early stage DFB laser development, gratings below the active region are used mainly to avoid waste of epi-growth due to the low yield problem of grating fabrication. Nowadays, in most cases, the grating layer lies above the active region, while the epi-layers including the buffer layer, lower cladding layer, active region, and grating layers are grown in the first epitaxial growth. The grating fabrication process is then performed to pattern and etch gratings into

the grating layer. A second epi-growth is performed to grow the grating cover layer, ridge etch stop layer, upper cladding layer and contact layers. So normally two epitaxial growths are required for RWG DFB lasers.

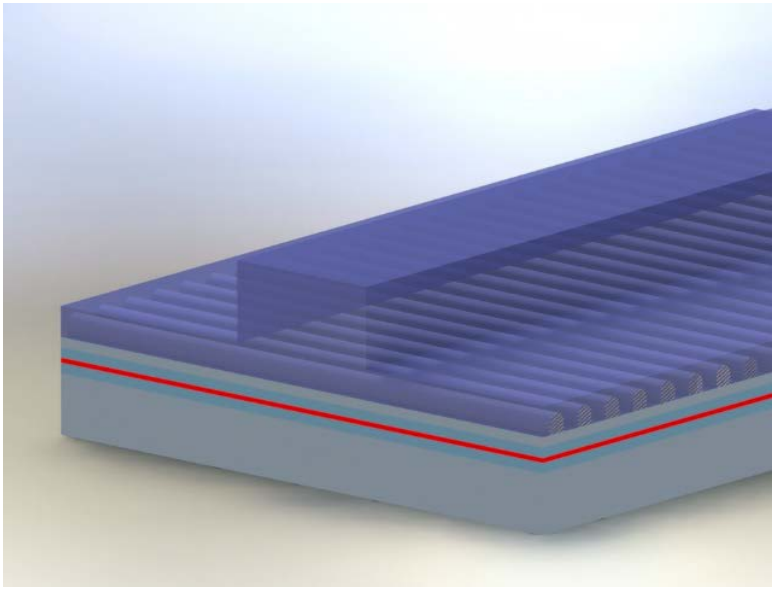

Figure 6. Illustration of RWG DFB laser with embedded grating layer above active region.

In most cases, the grating layers in the first growth structure are etched by a wet chemical etch, since dry etching is prone to inducing more surface damage, resulting in defects in the regrown materials.

DFB lasers can also be made using a buried heterostructure (BH) [24, 27-30] (Figure 7). Such a laser has its active region buried in either an p-n-p-n type junction [27, 30] or in an Fe-doped semi-insulating layer [28, 29, 31]. BH lasers usually have the first growth to the grating layers (same as RWG lasers). After grating is patterned, a photolithography step is used to define the active region stripe and wet etch is performed

to remove the regions on both sides of the active region stripe. Bromine Methanol is usually used as an non-selective etchant for this step (non-selective between InP and InGaAsP). Without removing the etch mask (SiO_2 in most cases), a second selective-area growth of the electrical isolation layers is performed. After the oxide etch mask is removed following regrowth, the wafer is sent to the MOCVD reactor for a third growth of the upper cladding and contact layers. Therefore the BH lasers require at least three epitaxial growth runs, including two regrowths.

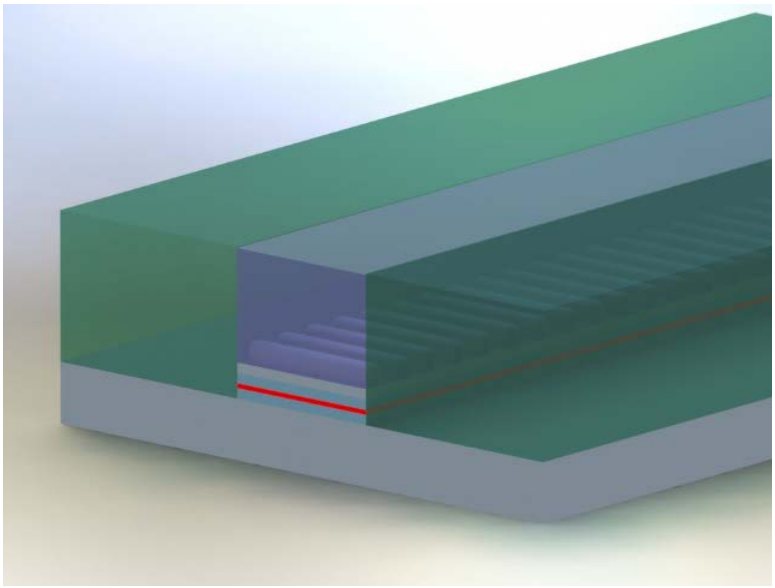

Figure 7. Illustration of BH DFB laser with buried active region and grating layer.

BH lasers have some unique advantages such as better confinement, lower threshold current, lower operation current, stable single-mode lasing, high output power, high operation temperature, low relative intensity noise (RIN), narrow linewidth, and

potentially high modulation speed (with Fe blocking layer), etc. [29]. However, BH lasers also have some common drawbacks. BH Lasers with p-n-p-n type current blocking layers suffer from high parasitic capacitance surrounding the active region [31], which limits the direct modulation (DM) bandwidth. BH lasers with Fe-doped semi-insulating isolation layer are able to operate at high DM speed, but due to the low solubility limit of Fe doping [32], excess Fe atoms tend to segregate along the regrowth interface, which can lead to current leakage problem.

Besides RWG and BH lasers, Miller, *et.al*., proposed a regrowth-free DFB laser in which the gratings are made only on the surface of the III-V materials surrounding a mesa or ridge [33], which was later termed “laterally coupled” DFB (LC-DFB) laser (Figure 8). Subsequently, LC-DFB lasers with non-planar lateral gratings have been widely investigated, including GaAs/InGaAs lasers [33-35], InAs/InGaAs Quantum Dot Lasers [36], InP/InGaAsP lasers [37, 38], GaInNAs lasers [39], InGaSbAs/AlGaSbAs lasers [39], InP/AlGaInAs lasers [23, 40, 41], etc.

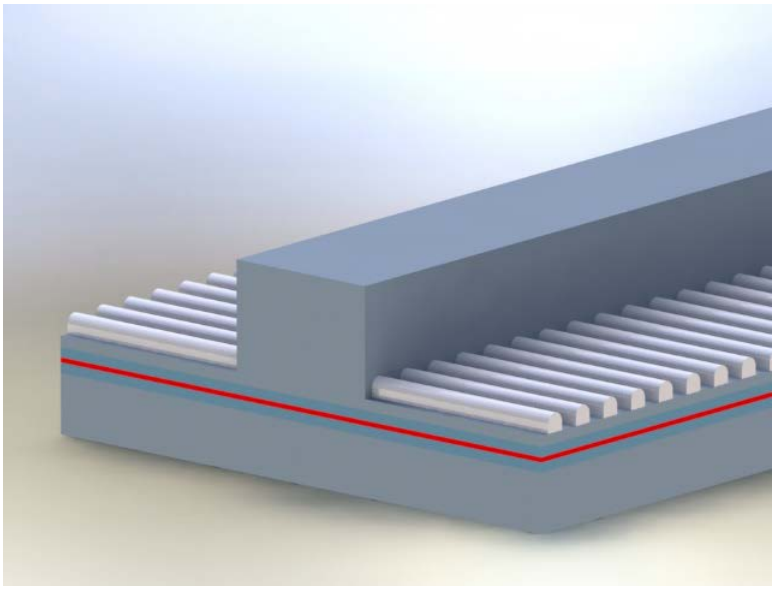

Figure 8. Illustration of LC-DFB laser. Only one growth is needed. Grating is fabricated on the surface of the semiconductors.

LC-DFB lasers do not require epitaxial regrowth. The regrowth process is expensive and complicated, with critical demands on wafer cleanliness and surface morphology. Also, LC-DFB lasers have the gratings made on the surface of the epi-wafer, which is easy to be monolithically integrated with other on-chip optical components. So, LC-DFB lasers aroused a lot of interest in low-cost DFB laser fabrication, and in photonic integration research and manufacture.

1.5 DFB LASER ARRAYS

Integrated multi-wavelength laser arrays are of tremendous interest and great importance in parallel optical interconnects (POIs) and WDM systems [42]. As a core element of PICs, distributed feedback (DFB) laser arrays play an important role in meeting the rapidly growing bandwidth requirement of long-haul communications and datacenter

networks. Monolithically integrated multi-wavelength DFB laser arrays with small footprint, low cost, low power dissipation and precise wavelength control are ideal candidates for the POIs and WDM systems. Also, monolithic laser arrays are able to greatly reduce packaging cost, which can be up to 80% of the total cost [43].

Many approaches have been reported to obtain a DFB laser array, such as using lasers with direct e-beam written gratings using e-beam lithography (EBL) [17, 44, 45], by changing ridge width with gain-coupled gratings [46], by selective area growth (SAG) [8, 47], or with tunable laser arrays [48], etc. However, EBL is an expensive and time-consuming process with low throughput, which is not scalable for high-volume manufacturing. Only some high-end DFB laser and laser arrays are made with EBL gratings. Changing the ridge width [46] is not a practical way to accurately control the effective refractive index. Lasers with different ridge width but the same cavity length have different active region size, which also leads to different threshold currents. With different ridge widths, the performance of the laser varies a lot due to changes in mode confinement, injection current density, *etc*. In considerations for making LC-DFB lasers, the coupling efficiency changes dramatically with ridge width, and the laser may not even lase when the ridge is too wide. Selective Area Growth (SAG) using a mask with different stripe widths has the same effect as changing the ridge width. A summary of using SAG for multi-wavelength DFB laser array fabrication can be found in [8]. Since growth does not take place on strip mask (usually SiO_2), group III species diffuse above SiO_2 mask to the SAG region, thus enhancing the growth rate. Thicker quantum wells due to enhanced growth rate, along with higher indium due to higher sticking coefficient of indium to gallium, result

in the gain peak shift in the SAG region towards longer wavelength. The amount of shift is determined by the ratio of mask width over mask opening [8]. So by SAG technology, the gain of different channels may be able to get separately adjusted. So for CWDM laser arrays, the gain of individual laser channels may be separately adjusted and aligned to the lasing wavelength as described in [8].

Tunable lasers usually need four electrodes for the front mirror, phase tuning region, gain region, and the back mirror. Tunable lasers also need a digital feedback control system for lasing mode selection, which is much more complicated compared to one-electrode DFB laser.

This dissertation is focused on developing DFB lasers and laser arrays with high performance and accurate wavelength control by a specially designed sampled grating method, using conventional and mass-production-compatible methods. Laterally coupled DFB laser and laser arrays and BH DFB laser and laser arrays have been proposed, theoretically analyzed and experimentally demonstrated.

Chapter 2: Theory

2.1 Uniform Grating DFB Laser

DFB semiconductor lasers are of great interest and have been extensively utilized for their high-bit-rate transmission performance in long-haul optical fiber communication systems. However, there are still some unsolved problems and improvements needed in their properties.

A DFB laser with uniform index-coupled gratings normally realized using interference lithography (IL), which intrinsically has two degenerate lasing modes [49]. At the Bragg wavelength, the optical mode is anti-resonant, which means the wavelength is forbidden for lasing. By numerical calculation, it can be seen that lasing is most likely to occur at two resonant modes that are symmetrically positioned on both sides of the Bragg wavelength, which are degenerate. But due to the arbitrary phases at the cleaved facets, the effect of facet coating, non-uniform gain distribution, *etc.*, degeneracy may sometimes be destroyed, then the laser is able to lase in a single longitudinal mode. However, this uncertainty can result in problems such as low yield, an uncontrolled lasing wavelength, multi-mode lasing, mode-hopping, *etc*. Also, in high-speed modulation, the side mode suppression ratio may be limited.

Figure 9 shows a typical laser cavity, which has a cavity length L, a gain region, and two mirrors with complex reflection coefficient r_1 and r_2. At the lasing threshold, the possible lasing mode should be able to reproduce itself in both amplitude and phase in a complete round trip:

$$r_1 r_2 e^{-j\beta 2L} = 1$$

Eqn. 2

where β is the complex propagation constant, whose real part is equals to $2\pi n_{eff}/\lambda$ and whose imaginary part is proportional to the gain or loss; n_{eff} is the effective index and λ is the wavelength of the propagation mode.

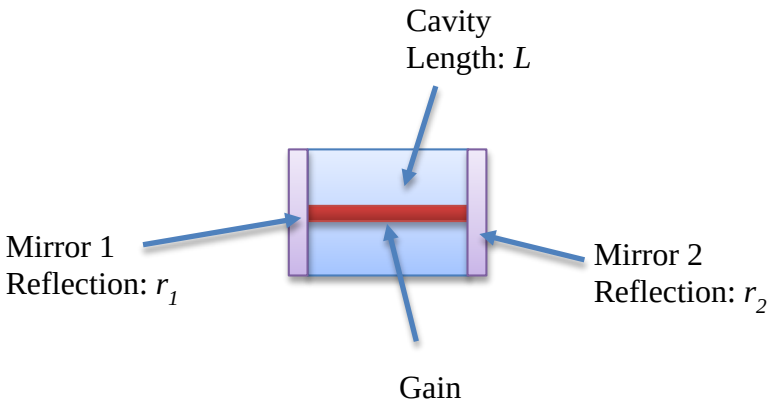

Figure 9. Laser cavity of a typical edge-emitting laser.

In a uniform grating DFB laser (grating layer shown in Figure 10) at threshold, a small section at the center of the cavity with a length of half the grating pitch can be investigated as the laser cavity, and the two sections on both sides can be treated as mirrors with gain: r_{g1} and r_{g2} (Figure 11).

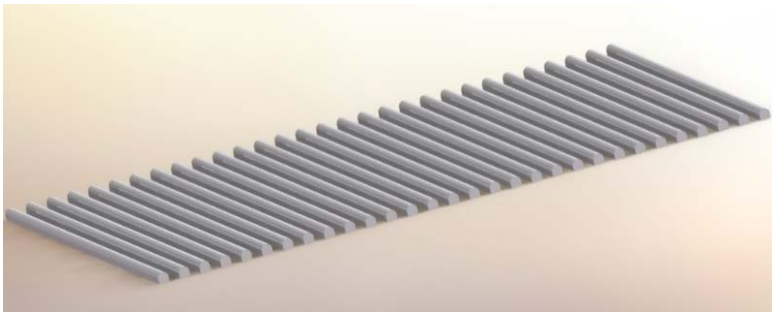

Figure 10. Illustration of grating layer in uniform DFB lasers.

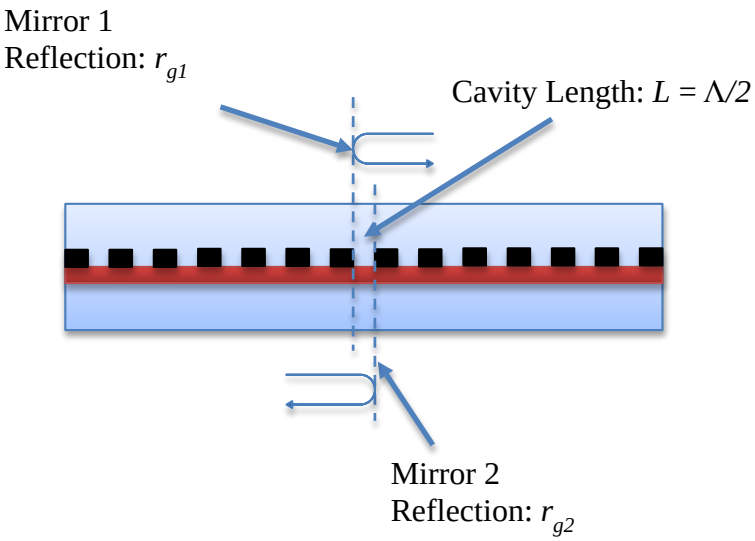

Figure 11. Investigation of DFB laser cavity with uniform gratings

where Λ is the grating pitch.

By substituting the center section cavity length Λ/2 into Eqn. 2, the threshold lasing condition for a uniform DFB laser is obtained as:

$$r_{g1}r_{g2} = -1$$

Eqn. 3

The Bragg wavelength is defined as:

$$\lambda_{Bragg} = 2n_{eff}\Lambda$$

Eqn. 4

Eqn. 3 has no solution at the Bragg wavelength, which results in the aforementioned anti-resonant cavity. By numerically solving Eqn. 3, there are always two modes equally spaced on both sides of Bragg wavelength, which result in uncertainty of the lasing wavelength, modulation problems, and possibly two lasing modes (illustration shown in Figure 12).

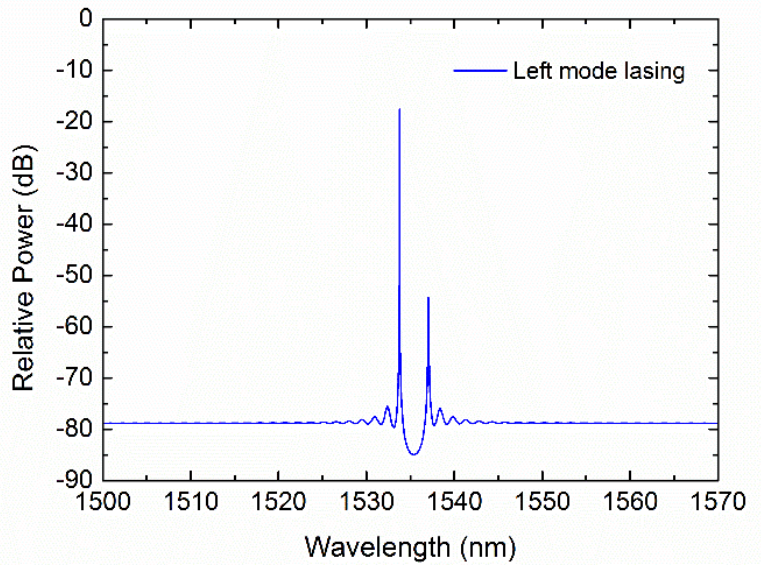

Figure 12.

Figure 12. continued

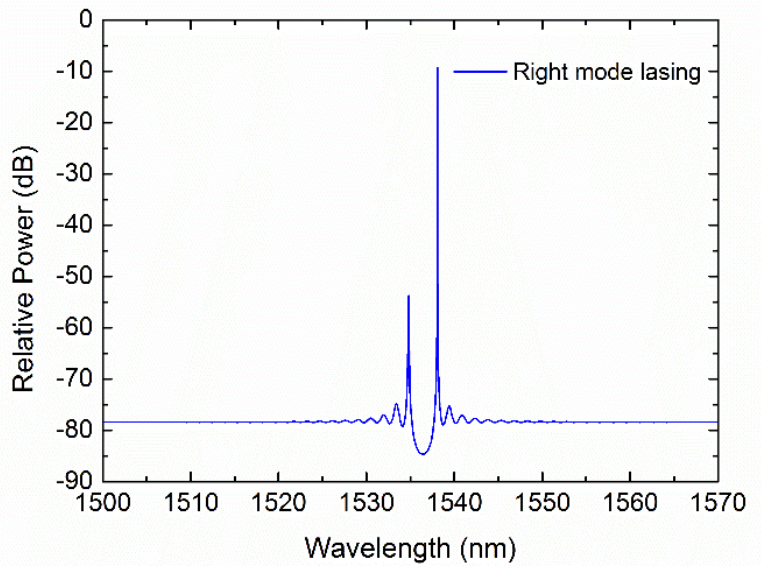

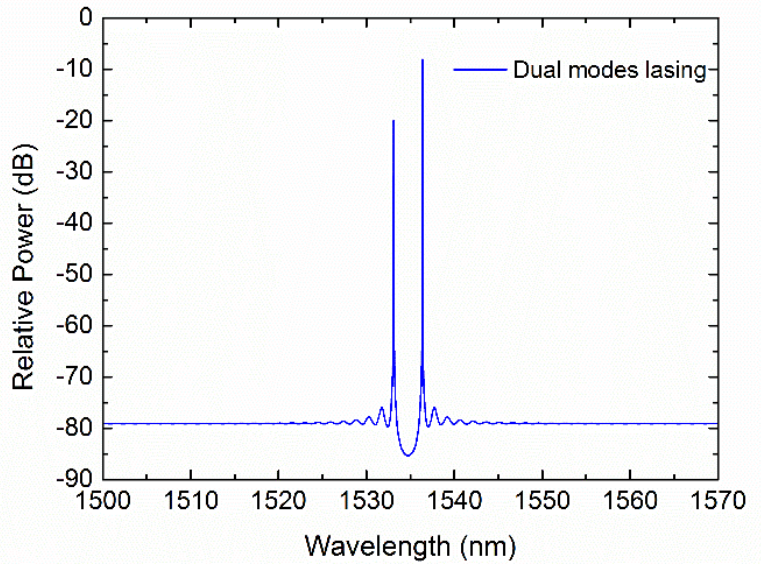

Figure 12. Illustrations of uniform grating DFB lasers with uncertain lasing modes: (Upper: left mode is lasing; Middle: right mode is lasing; Lower: both modes are lasing)

2.2 PHASE-SHIFTED GRATING DFB LASERS

One solution to the degenerate modes problem is to insert a phase-shift into the gratings at the center of the laser cavity by increasing the grating pitch with an additional half a grating pitch [50] (Figure 13):

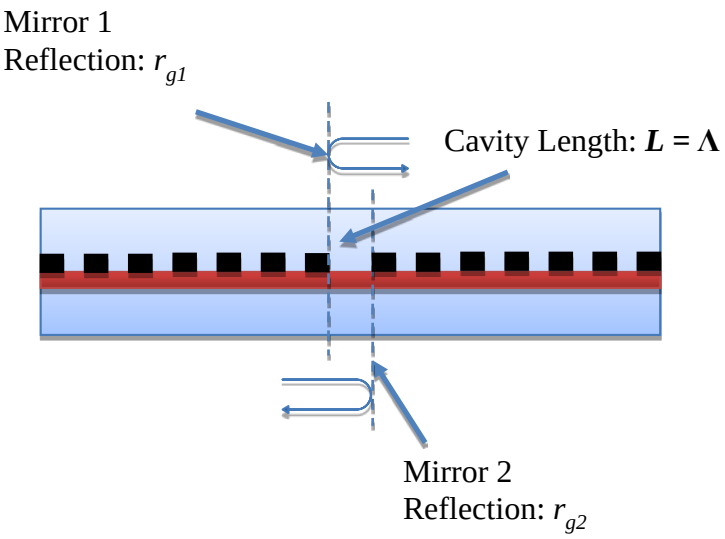

Figure 13. DFB laser cavity of a quarter wave phase shift.

By solving $r_1 r_2 e^{-j\beta 2L} = 1$

Eqn. 2 with cavity length L = Λ, we obtain:

$$r_{g1} r_{g2} = 1$$

Eqn. 5

The Bragg wavelength is now an analytic solution for the equation. With the insertion of the so called quarter-wave phase shift region, the optical mode now has a strong

resonance at the Bragg wavelength. The Bragg wavelength will be the only lasing mode for such a laser, which is very stable and is strongly wavelength selective.

The grating layer with quarter-wave phase shift is shown in Figure 14.

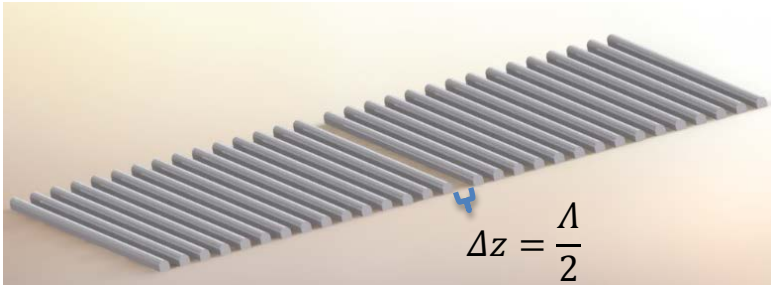

Figure 14. Grating layer with quarter-wave phase shift.

Figure 15 shows the illustration of lasing spectrum of phase-shifted DFB laser, which occurs right in the middle of the Bragg wavelength stopband.

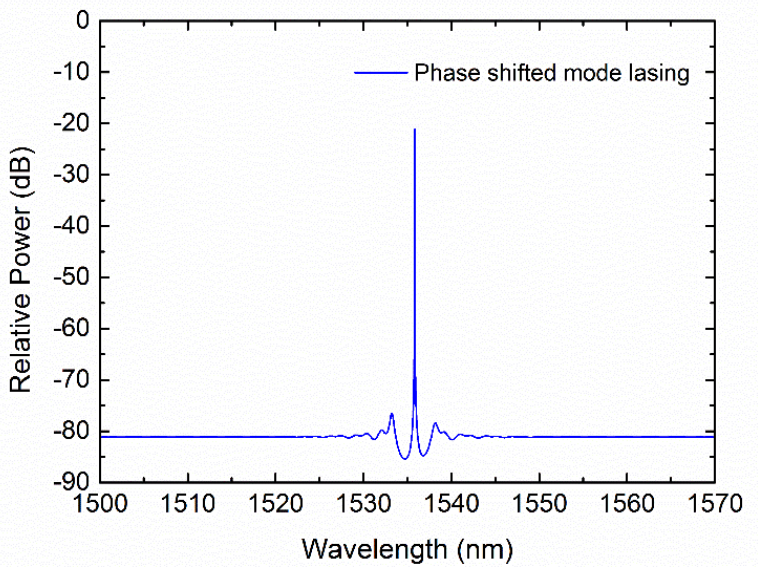

Figure 15. Illustration of lasing spectrum of phase-shifted DFB lasers.

Phase-shifted DFB lasers always have better performance compared to uniform grating DFB lasers. However, although there are some reports discussing possible ways to achieve phase shift without EBL [51, 52], the insertion of an exact quarter-wave phase shift is not achievable by any means but EBL. In industry, the widely used interference lithography (IL) is only capable of providing uniform gratings. To the best of my knowledge, most major DFB laser providers are still using IL to pattern and make uniform gratings for DFB lasers, although the yield is usually quite low.

Also, by using IL, the wavelength of individual lasers are fixed due to the fixed grating pitch in the IL patterned grating. It's hard to change the wavelength of individual lasers, therefore it is very hard to fabricate DFB-WDM laser arrays. A method is needed for the fabrication of DFB laser array using IL.

2.3 PHASE-MATCH CONDITION FOR UNIFORM GRATINGS

A look at how Bragg grating works is from the phase match condition. Figure 16 describes the phase match condition of uniform Bragg gratings (with/without phase-shift). When the wave vector of the Bragg gratings, k_{Bragg}, is equal to twice the wave vector of the lightwave, k_{wave}, the light will be redirected to the opposite direction, and Bragg reflection happens. However, the wave vector of Bragg grating is fixed by the grating pitch, leading to a fixed reflection wavelength, Bragg wavelength λ_{wave}. Multiple wavelengths cannot be achieved in this way.

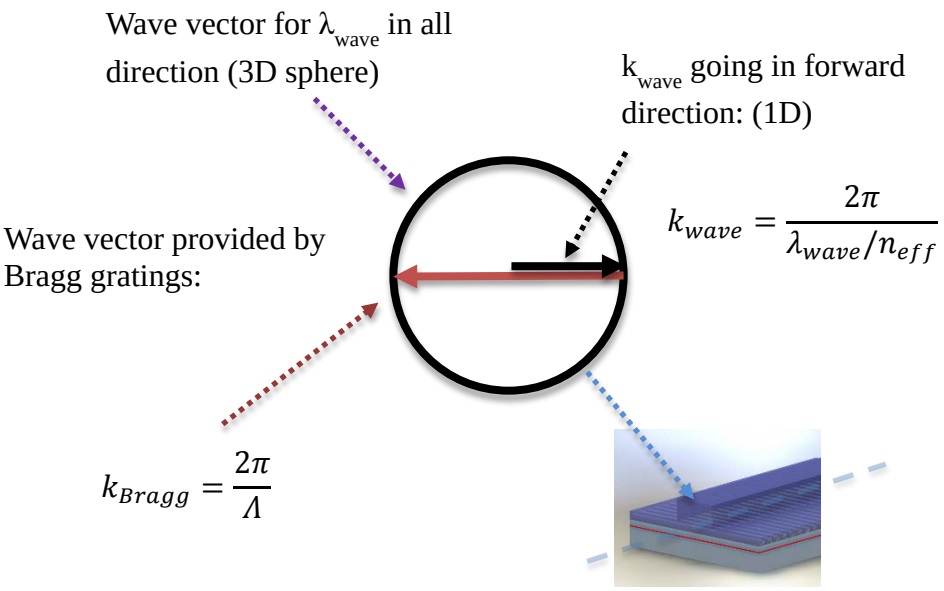

Figure 16. Illustration of phase match condition for uniform Bragg gratings.

2.4 Phase-Match Condition for Sampled Gratings

The sampled grating (Figure 17) method was first proposed by Eggleton *et.al*, in optical fibers [53], which essentially offers an additional wave-vector to obtain additional resonance channels other than the Bragg wavelength channel.

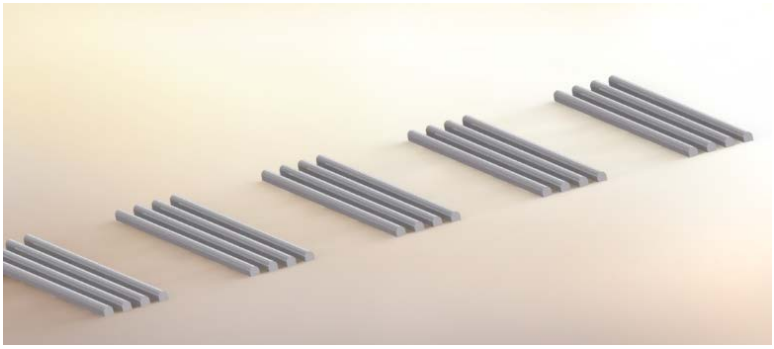

Figure 17. Illustration of a Sampled grating layer.

If the grating pitch is large (such as in optical fibers due to the low refractive index), the grating and the sampling can be made in one step. If the grating pith is small (such as in semiconductor devices due to the high refractive index), the sampling function can be applied to the uniform gratings using an extra photolithography step in additional to IL. During this photolithography step, the sampling pitch P can be individually defined on photo masks, which leads to an adjustable wave-vector, $k_{sampling}$, and a variable phase-matching condition for the reflection channels. The possibility of varying the resonance wavelength by varying the sampling parameters provides the basic mechanism for achieving multi-wavelength DFB laser arrays.

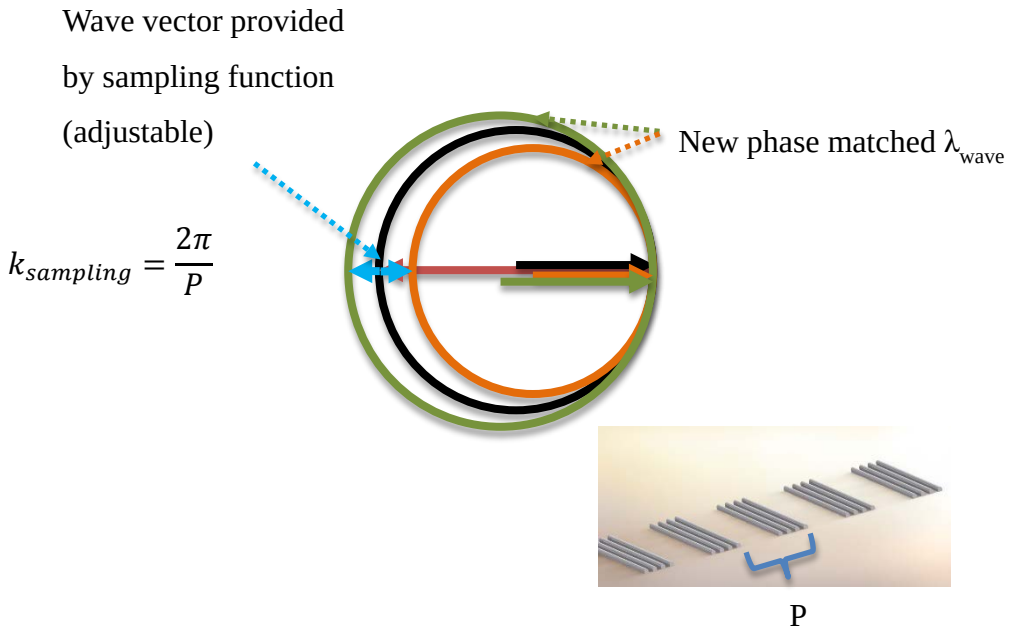

Figure 18. Illustration of Phase match condition for a sampled Bragg gratings.

2.5 SAMPLED GRATING WITH EQUIVALENT PHASE SHIFTS

Sampled gratings can provide the desired chirping functions [54, 55], which gave rise to the concept of an Equivalent Phase Shift (EPS) method that is able to offer a phase shift by using a uniform IL grating (without real phase shift) together with an imposed sampling function. Several devices have been reported using this method, such as fiber Bragg gratings [56], silicon waveguides [57, 58], fiber lasers [59] and conventional RWG lasers [26].

Fourier analysis method is an efficient tool in analyzing periodic structures, and is used here for analyzing Bragg gratings and sampled structures.

In an index-coupled DFB laser, the index changes along the laser cavity with two effective index (n_{high} and n_{low}).

n_{high} is the effective refractive index where the grating is of higher index material. It's typically an InGaAsP quaternary material with a photoluminescence (PL) spectrum peak at 1.1 μm to 1.2 μm for 1310 nm lasers, (which is usually called 1.1Q or 1.2Q, where Q stands for quaternary), or 1.2Q to 1.4Q for 1550 nm lasers. The composition of lattice matched 1.1Q, 1.2Q, 1.3Q and 1.4Q InGaAsP are $In_{0.85}Ga_{0.15}As_{0.33}P_{0.67}$, $In_{0.78}Ga_{0.22}As_{0.48}P_{0.52}$, $In_{0.72}Ga_{0.28}As_{0.61}P_{0.39}$ and $In_{0.66}Ga_{0.34}As_{0.26}P_{0.74}$, respectively.

n_{low} is the effective index at where the grating layer is etched. If a regrowth happens, the etched part is usually filled with InP which has a lower index. An important thing to notice is that the effective refractive index is the total index an optical mode sees. The material seen by the optical mode are mostly the same, except for the grating layer. Since the grating layer is usually very thin, the total index change ($n_{high} - n_{low}$) in usually in the

order of 0.01 for semiconductor materials. Here we define an average index n_{ave} = (n_{high} + n_{low}) / 2, which is around 3.22 for 1310 nm lasers and 3.20 for 1550 nm lasers. And we define an index difference n_{diff} = (n_{high} – n_{low}) / 2, which is in the order of 0.01. Then along the laser cavity, the effective refractive index n(z) can be expressed as:

$$n(z) = n_{ave} + n_{diff} \cdot \Delta n(z)$$

Eqn. 6

where Δn(z) stands for the variation along z, and is in [-1, 1] range, and n(z) = n_{high} when Δn(z) = 1, and n(z) = n_{low} when Δn(z) = -1.

In a device with uniform grating layer, the index modulation (Δn) can be described using Eqn. 7:

$$\Delta n_0(z) = e^{\frac{2j\pi z}{\Lambda}}$$

Eqn. 7

It should be mentioned that, here only the real part of the index modulation is considered. The subscript 0 stands for 0th order channel (Bragg wavelength channel) to distinguish from the other channels discussed later about sampled gratings.

z is the position along the cavity, which is in the same direction of the wave vector of gratings. In a phase-shifted grating structure, assuming a phase shift, Δz, is inserted at z = z_o, the index modulation is then described by Eqn. 8:

$$\Delta n_0(z) = \begin{cases} e^{\frac{2j\pi z}{\Lambda}} \ (z < z_0) \\ e^{(\frac{2j\pi z}{\Lambda} - \frac{2j\pi \Delta z}{\Lambda})} \ (z > z_0) \end{cases}$$

Eqn. 8

From Eqn. 8, a phase shift is obtained as:

$$\theta_0 = 2\pi \frac{\Delta z}{\Lambda}$$

Eqn. 9

It can be seen from Eqn. 9 that, when $\Delta z = \Lambda/2$, a phase shift of $\theta_0 = \pi$ is obtained, which is well known π phase shift, or quarter wave ($\lambda/4$) phase shift. From Eqn. 4 it can be seen that a full wave in materials (λ/n_{eff}) equals 2Λ, thus $\Lambda/2$ is a quarter wave.

In a sampled grating, the sampling function can be described as s(z), where s(z)=1 in the regions containing gratings, and s(z)=0 in the regions without gratings. So the index modulation can be defined as s(z) imposed onto original grating index modulation shown in Eqn. 7:

$$\Delta n(z) = s(z) e^{\frac{2j\pi z}{\Lambda}}$$

Eqn. 10

By Fourier transform, the sampling function can be expressed as Eqn. 11:

$$s(z) = \Sigma_m F_m e^{\frac{2jm\pi z}{P}}$$

Eqn. 11

By putting Eqn. 11 back into Eqn. 10:

$$\Delta n_m(z) = F_m e^{\frac{2jm\pi z}{P}} e^{\frac{2j\pi z}{\Lambda}}$$

Eqn. 12

where m is the order of the Fourier expansion, and F_m is its Fourier coefficient. To insert an EPS at $z = z_0$, the sampling function is to be increased by P/2 (Figure 19):

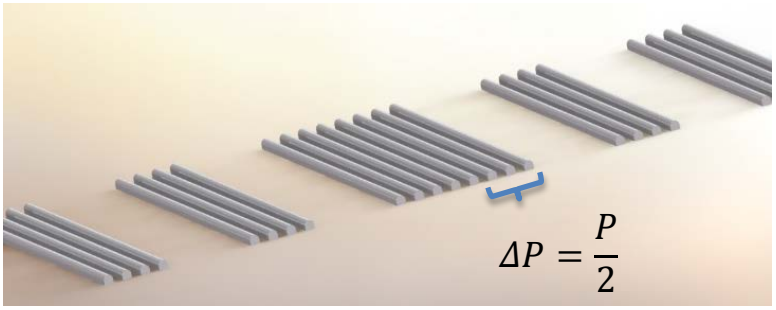

Figure 19. Illustration of grating layer with Equivalent Phase Shift.

Then Eqn. 12 has a discrete change at $z=z_0$:

$$\Delta n_m(z) = \begin{cases} F_m e^{(\frac{2j\pi z}{\Lambda} + \frac{2jm\pi z}{P})} & (z < z_0) \\ F_m e^{(\frac{2j\pi z}{\Lambda} + \frac{2jm\pi z}{P} - \frac{2jm\pi\Delta P}{P})} & (z > z_0) \end{cases}$$

Eqn. 13

Here only the 1st channel is considered, which is the only channel to be used as the resonant channel in design and fabrication of the proposed lasers. When m=1, an equivalent phase shift can be obtained in the 1st channel as:

$$\theta_1 = 2\pi \frac{\Delta P}{P}$$

Eqn. 14

Comparing Eqn. 14 to Eqn. 9, it can be seen that, by using the EPS method, the phase shift is obtained by changing of the sampling period, size of which is usually in micrometer level (typically 1.5 μm to 5 μm), however, a real phase shift is in 100 nm level

(which is usually around 100 nm to 120 nm). Thus EPS method is potentially very help in greatly reducing the difficulty of device fabrication.

One more thing should be mentioned regarding the sampled grating is the grating efficiency of the sampling structures. The grating efficiency corresponds to the Fourier coefficient of the sampled gratings. Also, it can be expressed as [59]:

$$F_m = \frac{1}{P}\int s(z)\cdot e^{-im\pi z/(\frac{P}{2})}\cdot dz$$

Eqn. 15

Where z goes from 0 to P. by scanning s(z), the grating efficiency can be plotted. Figure 20 shows the sampled grating efficiency compared to uniform gratings. The 1st, 2nd, and 3rd order sampling channels (m = 1, m = 2, and m = 3) have been plotted. It can be seen that, the maximum efficiency that a sampled grating can reach in new resonant wavelength is at m = 1 (1st channel) and duty cycle = 50%, where the maximum efficiency is 0.3183 (which equals $1/\pi$). Also, it should be noted that, when duty cycle equals 50%, the grating efficiency of the 2nd channel is 0, which means no resonance occurs.

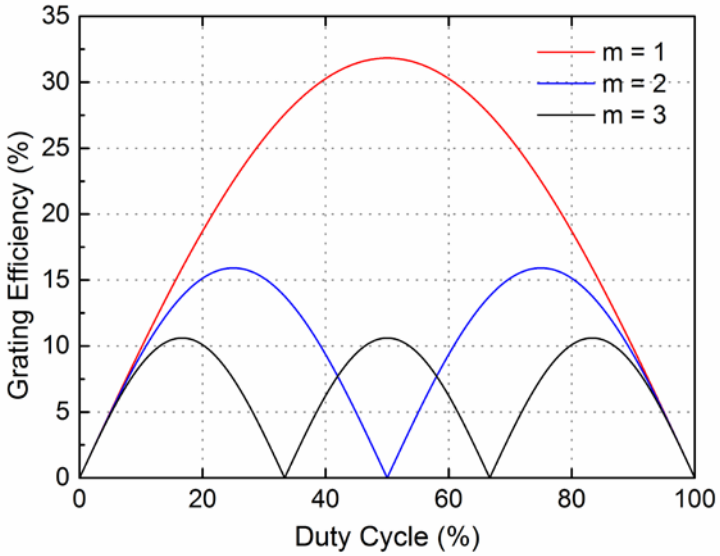

Figure 20. Sampled grating efficiency *vs.* duty cycle, regarding the 1st, 2nd, and 3rd channels.

The efficiency plot of sampled grating is similar to 1st order and high order Bragg gratings. With first order Bragg gratings, highest efficiency can be reached. 2nd order grating has no grating efficiency when duty cycle is 50%. In some early report, when it is hard to make first order gratings, third order gratings are used, with 50% duty cycle. When the resonance happens, the needed grating pitch is 3 times of first order gratings, but efficiency is 1/3.

2.6 Lasers and Laser Arrays with Equivalent Phase Shift

Based on wave vectors described in Figure 17 and Figure 18, phase match condition for the 1st channel (where Fourier coefficient equals 1) can be expressed as Eqn. 16:

$$k_{Bragg} + k_{sampling} = 2 \cdot k_{wave}$$

Eqn. 16

Plug in the parameters, a more straight forward equation can be obtained as Eqn. 17:

$$\frac{1}{\Lambda} + \frac{1}{P} = \frac{n_{lase}}{\lambda_{lase}}$$

Eqn. 17

Where λ_{lase} is the refractive index of the resonant wavelength for lasing, and n_{lase} is the refractive index at this wavelength.

Also, the Bragg wavelength of the grating can be determined. Assuming a linear refractive index dispersion of Δ (which is usually of the order of 10^{-4} / nm), the Bragg wavelength can be obtained as:

$$\lambda_{Bragg} = \frac{2\Lambda\,(n_{lase} - \lambda_{lase}\Delta)}{1 - 2\Lambda\Delta}$$

Eqn. 18

A more general expression for the sampled grating phase match condition is shown in Eqn. 19:

$$\frac{1}{\Lambda} + \frac{1}{mP} = \frac{n_{lase}}{\lambda_{lase}}$$

Eqn. 19

Same as before, m denotes the channel order of the sampled gratings.

Figure 21 shows an illustration of the lasing spectrum happening in 1st order channel of sampled gratings with equivalent phase shift.

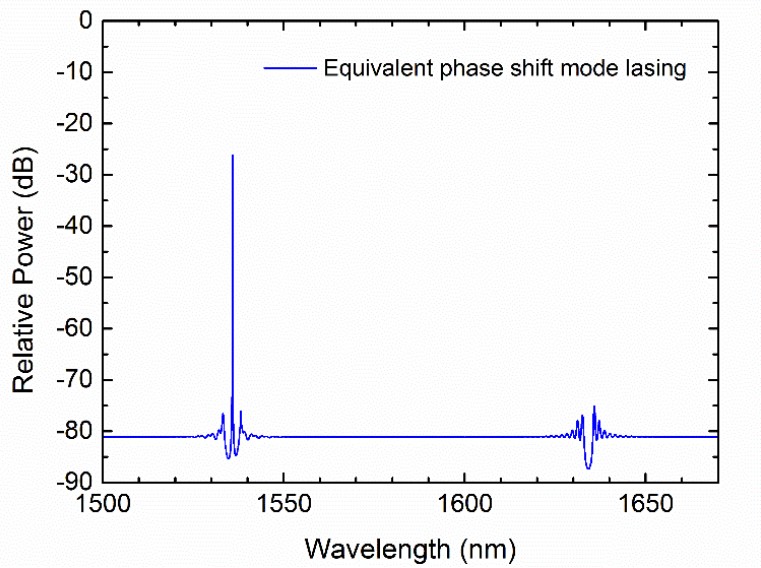

Figure 21. Illustration of lasing spectrum of DFB lasers with EPS. The lasing wavelength is at ~1535 nm, with a quarter-wave phase shift. The Bragg wavelength is at ~1635 nm, which is far away from the gain, and therefore lasing is suppressed.

By fixing the Bragg wavelength but changing the sampling period P on a laser bar, a laser array with different lasing wavelength can be achieved. Also each laser contains an equivalent phase shift to ensure single mode lasing and accurate lasing wavelength positioning. An illustration of the grating layer of a 4-wavelength laser array is shown in Figure 22.

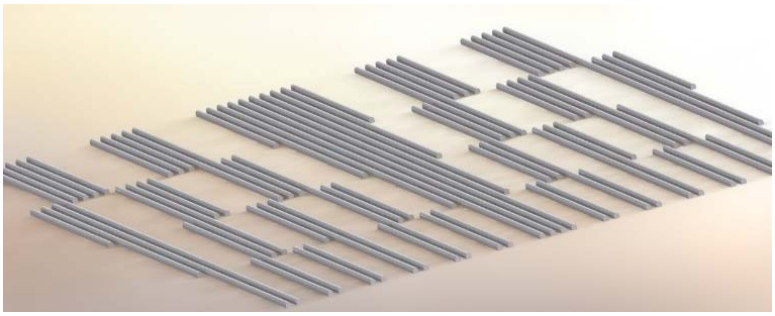

Figure 22. Illustration of a grating layer of a 4-wavelength laser array. 4 lasers share the same bass Bragg gratings (same grating pitch by IL), but each one has an individually designed sampling pitch (designed on sampling photomask).

Based on this principle, a WDM laser array can be designed. Details of designing a WDM laser array is to be discussed in Chapter 3.

Chapter 3: Design, Simulation and Setup

3.1 Design of DFB Lasers and Laser Arrays with Equivalent Phase Shift (EPS)

Lasers and laser arrays can be designed using Eqn. 16. In the laser design, several aspects should be considered.

Firstly, a typical multiple-quantum-well (MQW) epi-structure, the photoluminescence (PL) spectrum has a full width at half maximum (FWHM) around 60 nm. In most cases the center 30 nm has sufficient modal gain for a good semiconductor laser. Therefore, λ_{lase} should be located within this 30 nm wide gain region for good lasing performance.

Secondly, the possibility of lasing at the Bragg wavelength should be eliminated. The optical gain in a MQW epi-structure has a steep drop at the longer wavelengths, where the photon energy is near the bandgap, and it has a gradual drop on the shorter wavelength side, where the phonon energy is larger than the bandgap. From this perspective, it is better to set λ_{Bragg} at the longer wavelength side of λ_{lase}. Based on this reasoning, the green wave vector sphere is chosen for the phase-matching condition in Figure 18, where $k_{sampling}$ is added to k_{Bragg}, and the "+" sign is chosen for the phase matching condition in Eqn. 16 and Eqn. 17. Also, the index m is set to 1 in Eqn. 11, Eqn. 12, and Eqn. 13 equals 1, for the 1st-order lasing channel at λ_{lase}. Also, by choosing a Bragg wavelength that is longer than the lasing wavelength, the Bragg grating pitch can be larger, which makes the grating fabrication easier.

It is also possible to choose the orange sphere in Figure 18 as the phase match condition, and the Bragg wavelength is on the shorter wavelength side of the lasing

wavelength at the phase-matched condition. The sign in Eqn. 16 and Eqn. 17 is then "-", and m = -1 in Eqn. 11, Eqn. 12, and Eqn. 13. This is called the -1st channel. But due to the higher possibility of lasing at shorter wavelengths, this phase matching condition is not selected in fabrication of the devices.

Thirdly, for practical reasons in sampled grating fabrication, the Bragg wavelength cannot be too far away from the lasing wavelength, due to the limited length of the sampling period. Using contact photolithography method, the minimum controllable opening (unsampled region width) is around 1.5 μm. The sampling duty cycle is optimized at 50%, so the sampling pitch *P* should not be significantly smaller than 3 μm. With a 3 μm sampling pitch, the Bragg wavelength is estimated to be around 110 nm to 120 nm away from the lasing wavelength. In other words, with a lasing wavelength at 1530 nm, the Bragg wavelength can be at around 1650 nm.

To design a laser array, the first step it to select the channel numbers and their desired wavelengths. The second step is to estimate the effective refractive index of each channel. The next step is to adjust the grating pitch for the whole array and simultaneously calculate the sampling period and Bragg wavelength. When the Bragg wavelength is far enough from the gain peak, and the smallest sampling period is within the resolution limit of contact photolithography, the optimized design parameters can be incorporated into the photo-mask layout.

Table 1 is an example of the design parameters of an 8-wavelength layer DFB array by the EPS method. The wavelength spacing is 800 GHz per channel (corresponding to $\Delta\lambda \approx 6.4$ nm per channel). The wavelength span is from 1535 nm to 1580 nm (195.2 THz to

189.6 THz), and is centered at 1558 nm. The grating pitch is selected to be 255.5 nm. The refractive index dispersion $\Delta = d_{neff} / d\lambda$ is calculated to be ~2.5×10^{-4} / nm, with n_{eff} at λ=1550 nm set at 3.206 by grating design. The sampling periods are then calculated to be from 3.76 μm to 7.61 μm. By Eqn. 18, the Bragg wavelength is calculated to be 1651.2 nm, which is sufficiently far removed from the material gain peak at around 1550 nm.

No.	Frequency (THz)	λ (nm)	N_{eff}	Sampling Period (μm)	Half Period (μm)
1	195.2	1535.82	3.209544	**3.764**	**1.882**
2	194.4	1542.14	3.207964	**4.057**	**2.028**
3	193.6	1548.51	3.206371	**4.399**	**2.199**
4	192.8	1554.94	3.204765	**4.804**	**2.402**
5	192	1561.42	3.203145	**5.292**	**2.646**
6	191.2	1567.95	3.201512	**5.890**	**2.945**
7	190.4	1574.54	3.199865	**6.640**	**3.320**
8	189.6	1581.18	3.198204	**7.608**	**3.804**

Table 1. Design of an 8-wavelength laser array with Equivalent Phase Shifts.

Table 2 is an example of the same WDM laser array designed achieved with EBL gratings.

No.	Frequency (THz)	λ (nm)	N_{eff}	E-beam Pitch(nm)	Half Pitch (nm)
1	195.2	1535.82	3.209544	**239.259**	**119.629**
2	194.4	1542.14	3.207964	**240.361**	**120.181**
3	193.6	1548.51	3.206371	**241.475**	**120.737**
4	192.8	1554.94	3.204765	**242.598**	**121.299**
5	192	1561.42	3.203145	**243.732**	**121.866**
6	191.2	1567.95	3.201512	**244.877**	**122.438**
7	190.4	1574.54	3.199865	**246.032**	**123.016**
8	189.6	1581.18	3.198204	**247.199**	**123.599**

Table 2. Design of the same 8-wavelength using E-beam lithography.

It can be seen that for this 8-wavelength laser array with a 800 GHz channel spacing, the EPS method requires a sampling period change of 0.3 μm (from channel 1 to 2) to 1 μm (from channel 7 to 8). The EPS region length varies from 1.9 μm to 3.8 μm, which can be controlled very accurately using photomask technology and photolithography methods. But by using the EBL method, the phase shift region dimension is around 120 nm, and the grating pitch difference is 1.1 nm between adjacent channels. It is very difficult to achieve dimension control to a 1 nm accuracy in fabrication, even by using EBL.

Now, let's look deeper into the design of the laser array with EPS under variable parameters.

Photo-mask fabrication technology is very mature today. In the manufacture of masks, errors in the sampling period are negligible. Errors in duty-cycle should likewise be very small, and in any case this can be corrected by the photolithography process. So any deficiency due to mask technology will not be discussed further here.

In real fabrication, the grating pitch can have errors compared to the original design, which directly contribute to errors in the resonant wavelengths of a laser array. Using the sampling periods calculated in Table 1, the lasing wavelengths are plotted in Figure 23, with the grating pitch varying from 254.5 nm to 256.5 nm:

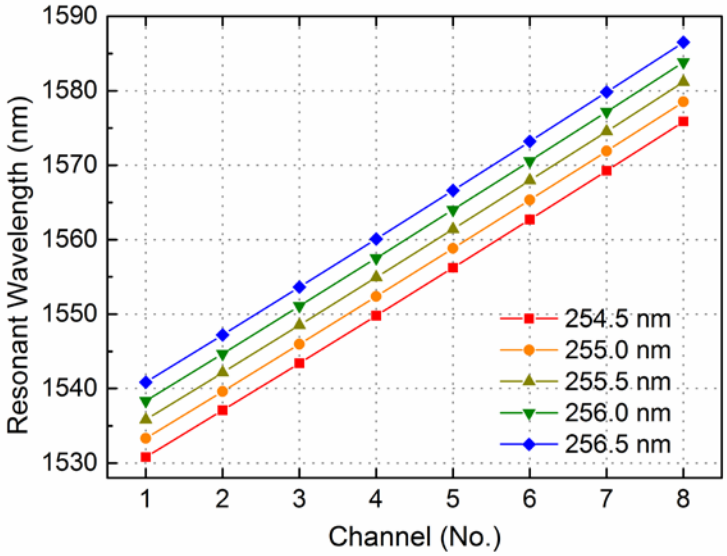

Figure 23. Resonant wavelength shifting with fixed sampling period but changing grating pitch.

The resonant wavelength shift rate with grating pitch is at roughly 5 nm / nm. This shifting rate is smaller compared to the shift rate $2\times n_{eff}$ ($\approx$6.4), which is due to refractive index dispersion Δ of the semiconductor material.

Material dispersion Δ has a significant influence in designing laser arrays. Assuming the fabricated grating pitch is the same as the design, but the estimation of Δ is off, the wavelength channel spacing will change. Figure 24 shows the calculated resonant wavelengths for different values of Δ. When $\Delta = 2.5 \times 10^{-4}$ /nm is used in the design for a

800 GHz channel spacing, a larger dispersion of $\Delta = 5 \times 10^{-4}$ /nm results in a channel spacing of ~722 GHz / channel (~5.8 nm / channel), when a zero dispersion ($\Delta = 0$) results in a channel spacing of 897 GHz / channel (7.3 nm /channel).

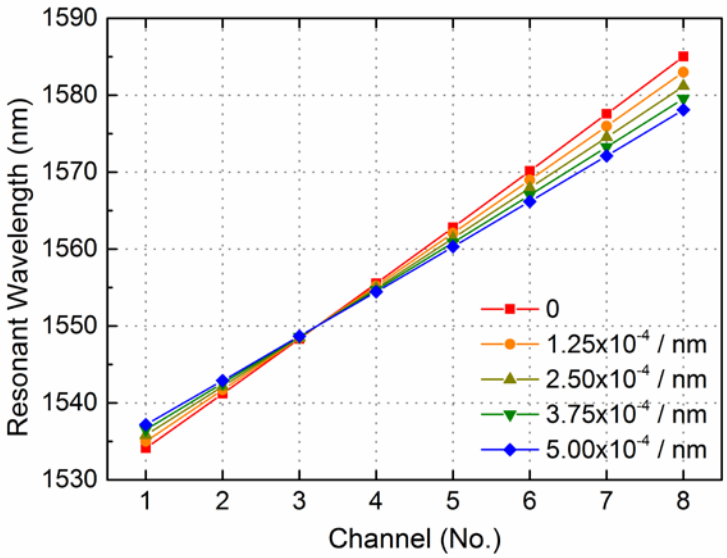

Figure 24. Resonant wavelength with refractive index dispersion changing from 0 to 5×10^{-4} / nm, with same sampling structure design and grating pitch.

The different dispersion lines in Figure 24 intersect at $\lambda = 1550$ nm, which is due to the assumption that n_{eff} is fixed at 3.206 at 1550 nm. Since linear dispersion is used in the design, the deviation from real n_{eff} to estimated n_{eff} results in a linear shift of the wavelength of the whole array.

When the experimental results differ from the designed parameters, errors can be fitted by grating pitch, dispersion parameters, and effective index, which makes the future design interaction more reliable.

3.2 SIMULATION OF THE DFB DEVICES

When dealing with DFB lasers, the coupling constant κ is an important factor to consider [60]. In index-coupled DFB lasers, distributed feedback is provided by the variation of the refractive index modulation (Eqn. 7). For a sinusoidal shape grating layer, κ can be defined [60] by:

$$\kappa = \pi n_{diff}/\lambda$$

Eqn. 20

For a rectangular shape grating layer, κ is 4/π of Eqn. 20 [49], which is:

$$\kappa = 4n_{diff}/\lambda$$

Eqn. 21

κ measures the backward Bragg scattering strength and the amount of feedback per unit length by the structure. There are different estimates for the optimized κ for DFB lasers, but generally a good κ is between 1 and 2.

For the LC-DFB lasers discussed in this dissertation, an AlGaInAs/InP epi-wafer is used, which was grown by Metalorganic Vapor Phase Epitaxy (MOVPE) in a single growth run on a (100) n-InP substrate. The InP substrate used was doped with sulfur to the level between 2×10^{18} and 8×10^{18} cm^{-3} for a high conductivity. The epilayer structure contains an n-InP buffer layer (500 nm, Si-doped), followed by an n-InP cladding layer (500 nm, Si-doped, doped to 10^{18} cm^{-3}), an active region, a p-InP cladding layer (1.8 μm, Zn-doped, doped to 10^{18} to 1.5×10^{18} cm^{-3}) and a contact layer (200 nm, containing a 25 nm 1.3Q InGaAsP layer doped to 3×10^{18} cm^{-3}, a 25 nm 1.5Q InGaAsP layer doped to 3×10^{18}

cm^{-3} and 150 nm InGaAs layer doped to 1×10^{19} cm^{-3}). The active region consists of an undoped Graded-Index (GRIN) separate confinement heterostructure (SCH), in which an AlGaInAs multi-quantum well gain region is bounded between p-doped and n-doped GRIN layers, respectively. An un-doped InAlAs hole confinement layer and an n-doped InAlAs electron confinement layer are placed below and above the active region, respectively. The gain region contains five undoped AlGaInAs quantum wells (QWs), each well containing a 1% compressively-strained AlGaInAs active layer and tensile-strained AlGaInAs barrier layer. The thicknesses of the wells and barriers are 6 nm and 9 nm, respectively.

The peak of the photoluminescence (PL) spectrum is at ~1535 nm. The refractive index profile of the epi-wafer used is plotted in Figure 25:

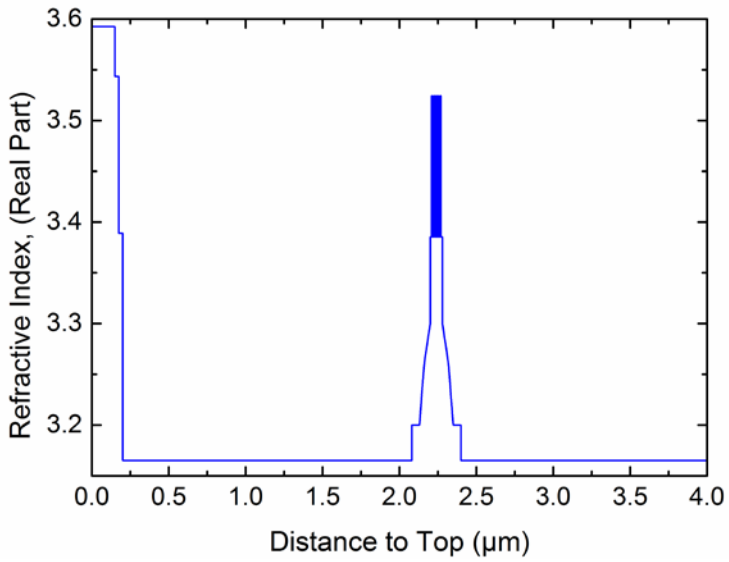

Figure 25. Refractive index (real part) of the AlInGaAs/InP epi-wafer.

The detail of refractive index (real part) around the QW region is shown in Figure 26:

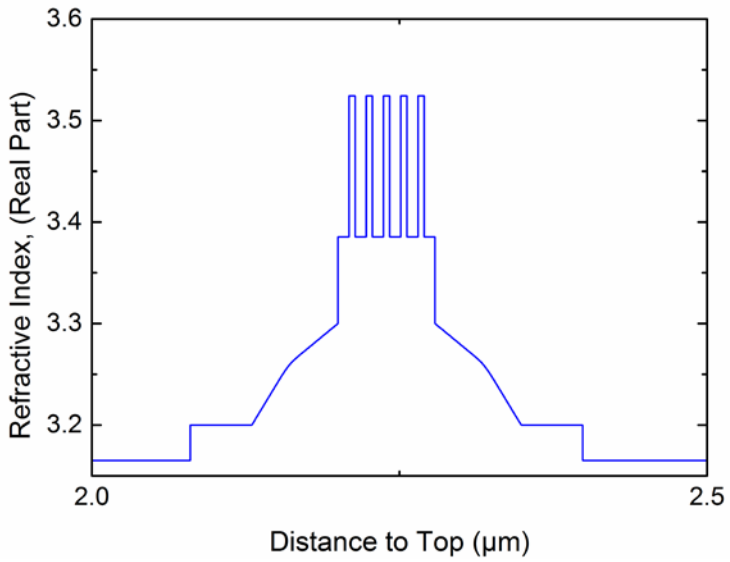

Figure 26. Refractive index (real part) of the AlInGaAs/InP epi-wafer around the quantum well region.

Figure 27 shows the illustration of the cross section of a laterally-coupled DFB laser, assuming the lateral gratings are on both sides of the ridge. The ridge, with a width of W_{ridge}, is etched to a depth of D_{etch}. Gratings with a lateral width of $W_{grating}$ are etched on both sides of the ridge. So the total width of the ridge plus gratings on both sizes is $W_{ridge}+ 2\times W_{grating}$. Then a SiO_2 layer with a thickness of W_{SiO2} is used to cover the surface of the semiconductor for electrical isolation. W_{SiO2} is chosen to be 500 nm in both simulations and experiments. The epi-wafer used (shown in Figure 26) has an active region at ~2.2 μm below the semiconductor surface. The lateral gratings have a duty cycle of 50%

to maximize the coupling efficiency. So the optimization of the device is focused on the parameters W_{ridge}, $W_{grating}$, and D_{etch}.

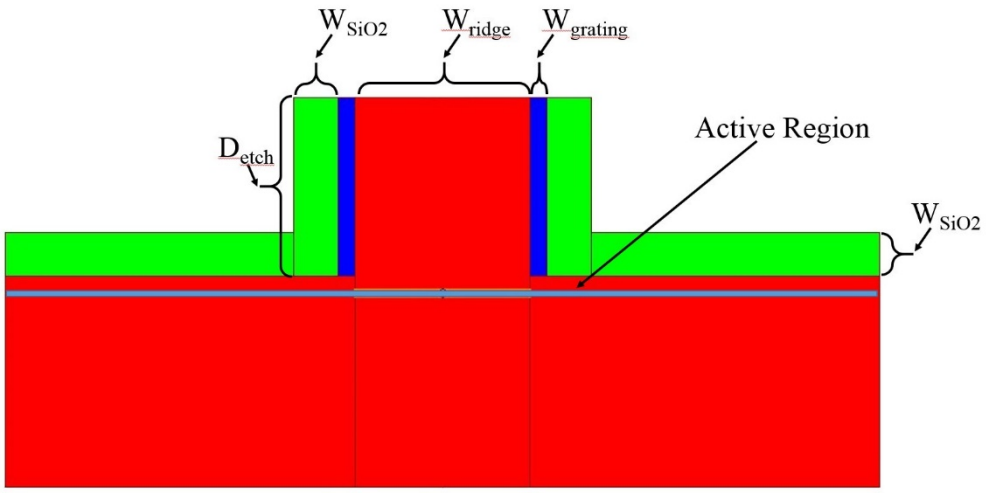

Figure 27. Illustration of the cross section of a laterally-coupled DFB laser.

A simulated average transverse mode is shown in Figure 28. (Calculation parameters: D_{etch} = 2.05 μm, W_{ridge} = 2 μm, $W_{grating}$ = 200 nm, W_{SiO2} = 500 nm.)

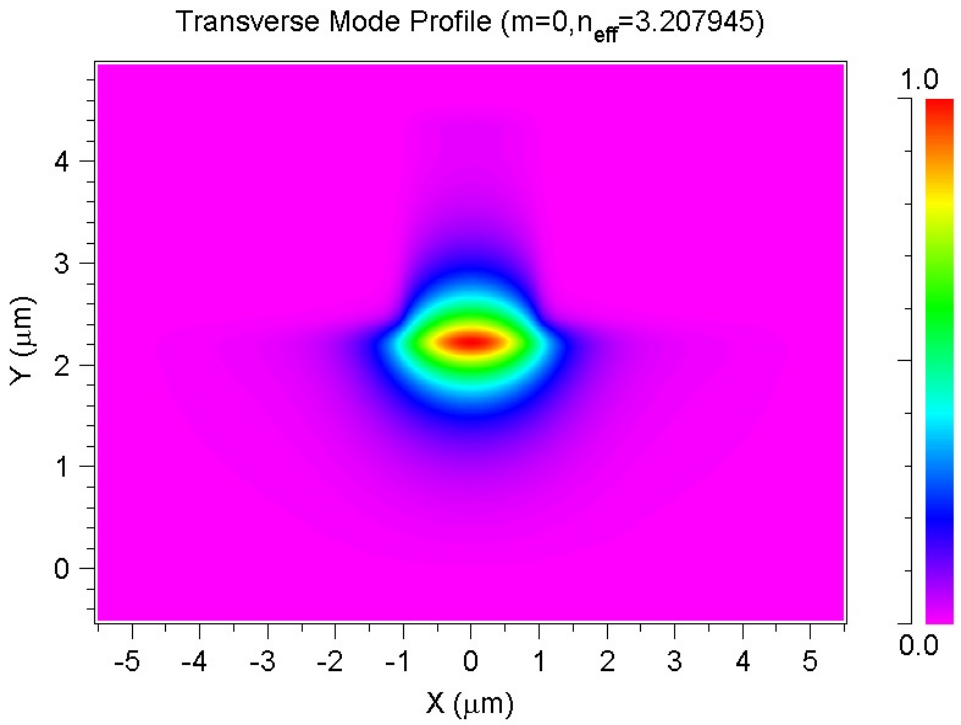

Figure 28. Example of Calculated average mode profile in the proposed LC-DFB laser.

RSoft components: BeamProp, GratingMod, and FullWave are used in the simulation.

LC-DFB lasers intrinsically have a lower coupling efficiency compared to conventional grating-coupled RWG and BH lasers, in which the grating resides in close proximity to the gain region either below or above. The LC-DFB laser has gratings only on the lateral and lower surfaces, so the overlap of the modal optical field to the grating index modulation is reduced, occurring mostly at the corners of the ridge. The coupling efficiency *vs.* ridge width, etch depth, and grating width have been investigated, along with the effects of the average effective refractive index and the overlap factor for the QWs.

3.2.1 Coupling efficiency *vs.* ridge width

How strong the optical mode is confined by the ridge is a critical factor. By changing the ridge width (W_{ridge}), for devices with $W_{grating}$ = 100 nm, 200 nm, and 300 nm, while fixing other parameters, the coupling constant κ have been calculated and are shown in Figure 29.

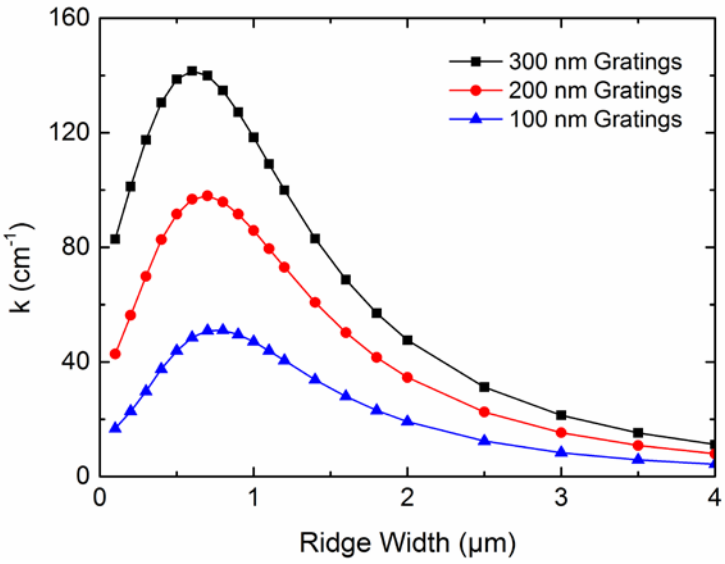

Figure 29. Calculated κ *vs*. ridge width with different grating width.

It can be seen that κ peaks at around 0.7 μm ridge width. When the ridge width is narrower, the optical mode is the upper cladding is compressed and pushed downward, which causes the coupling between gratings and optical field to drop dramatically. But as the ridge width is increased beyond 0.7 μm, the optical field becomes more confined in the ridge, and the optical field seen by the gratings is reduced, leading to a lower overlap and coupling efficiency. However, the weakly index-guided RWG laser is different from a pure

optical waveguide. As the ridge width is narrowed, lateral current spreading is reduced and the active region width also becomes smaller. Also, it is very difficult to make good electrical contact to a very narrow ridge, which may result in excessively high contact resistance.

The change in average effective refractive index with ridge width is shown in Figure 30.

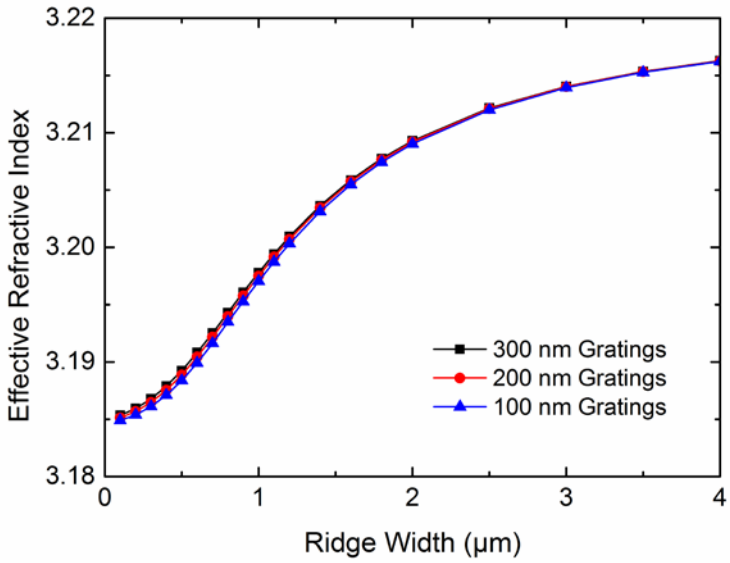

Figure 30. Calculated average refractive index *vs*. ridge width with different grating width.

Devices with different grating width have very similar refractive indices, which means the lateral grating has a very small influence on the *total* refractive index. As the ridge width decreases, the effective refractive index drops, due to the aforementioned reason, i.e., changes in the distribution of the modal optical field. As the optical field shifts

downward, it contains larger contributions from the low index materials, causing the total effective refractive index to decrease.

The calculated overlap factor (Γ) as a function of ridge width is shown in Figure 31. Here Γ is only considered in the lateral and transverse directions.

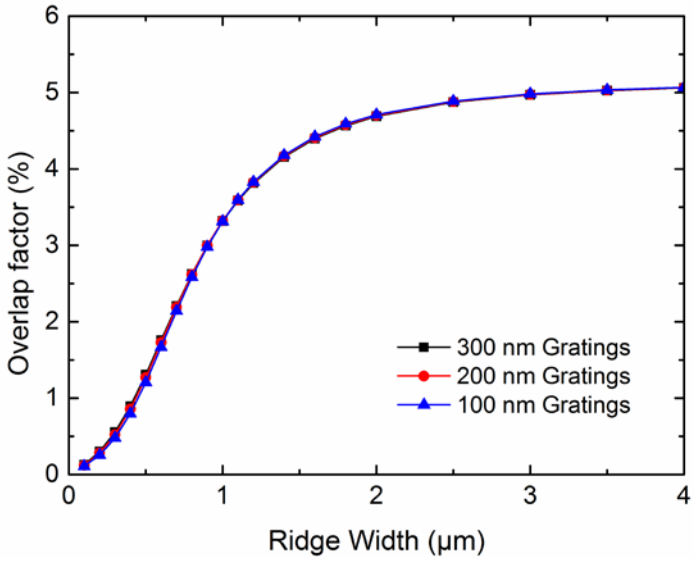

Figure 31. Calculated overlap factor *vs.* ridge width with different grating width.

The overlap factor also drops with decreasing ridge width. When the ridge is over 2 μm wide, the overlap factor changes slowly, with a typical value of 5% for a 5-QW laser structure. From Figure 31, it is clear that the ridge width cannot be too small, since a very low overlap factor results in a drop in amplified spontaneous emission and the stimulated emission process.

3.2.2 Coupling efficiency *vs*. etch depth

The etch depth is also a very important factor that affects the coupling parameter κ. By fixing other parameters while changing the etch depth (D_{etch}), devices with $W_{grating}$ = 100 nm, 200 nm, and 300 nm have been calculated. The coupling constant κ is shown in Figure 32.

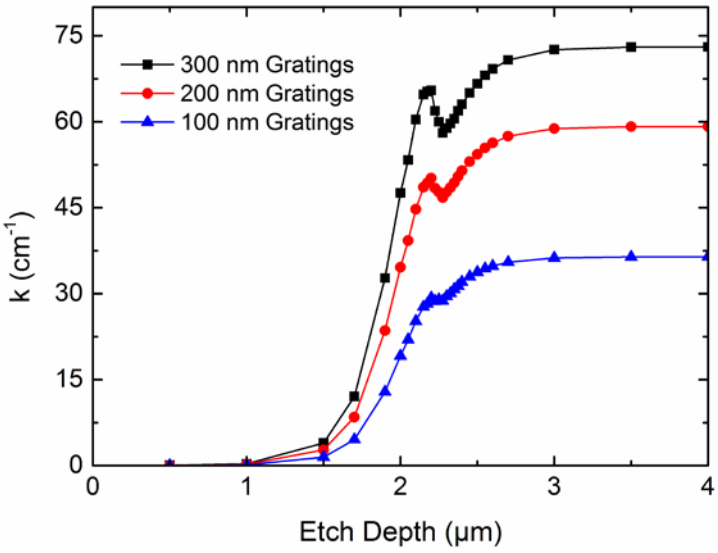

Figure 32. Calculated κ *vs*. etch depth with different grating width.

When the etch depth is below 1 μm, κ is negligible. When etch goes within 300 nm above QWs, κ goes up dramatically. Also, κ achieves a peak value when the etch depth D_{etch} = 2.2 μm, *i.e.*, when it reaches the center position of the MQWs (Figure 33). The other parameters are the same as in Figure 28.

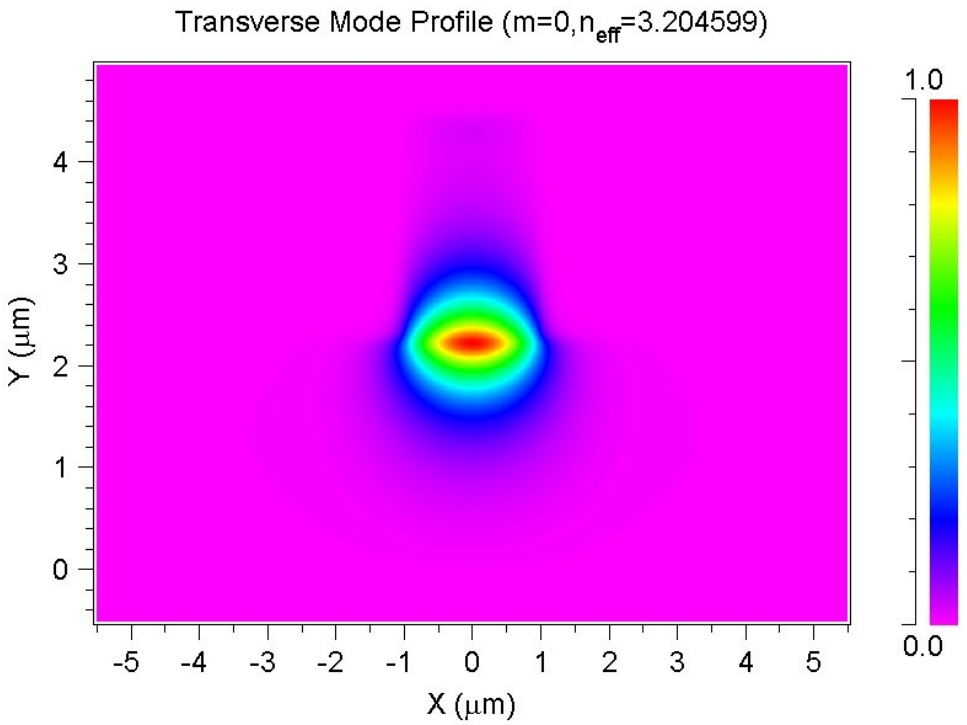

Figure 33. Calculated optical mode profile at an etch depth of 2.2 μm (at MQWs).

The value of κ drops slightly after etching through the MQWs to around 100 nm below the MQWs. The simulated optical mode profile for D_{etch} = 2.275 μm is shown in Figure 34. This drop in κ is possibly due to the very strong confinement of the MQW region by the ridge, which causes the optical field distribution to narrow compared to that is Figure 33, resulting in a weaker field overlap with the lateral gratings.

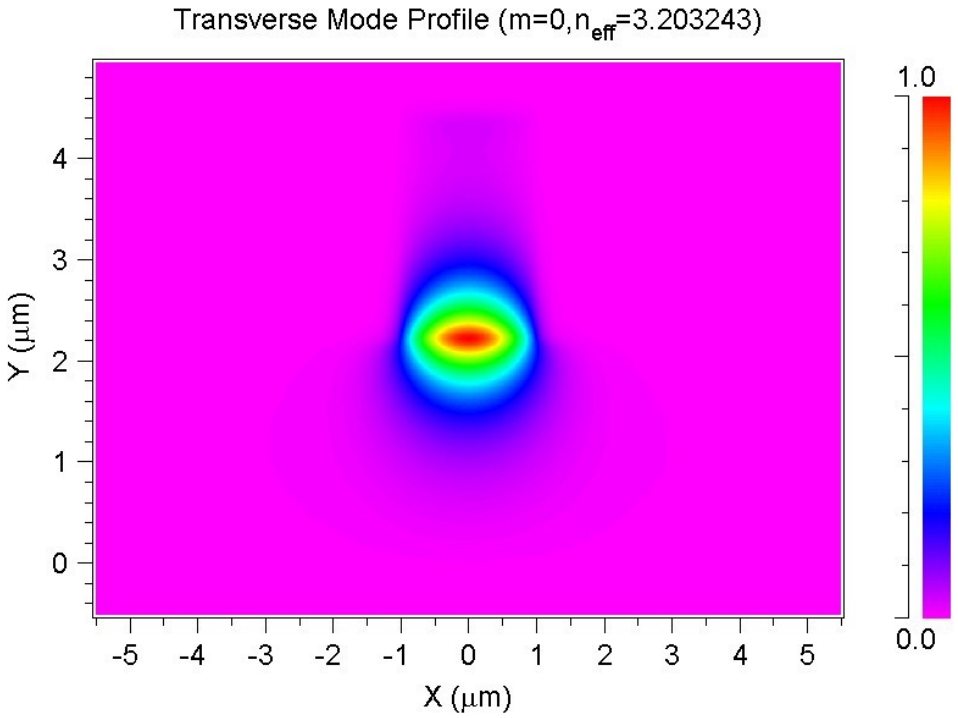

Figure 34. Calculated optical mode profile at the etch depth of 2.275 μm (below QWs).

When the etch depth goes beyond 3 μm (well through the MQWs region), κ reaches its maximum value and remains constant as the etching goes deeper. This is due to the total index confinement of the optical field by the etched ridge Figure 35.

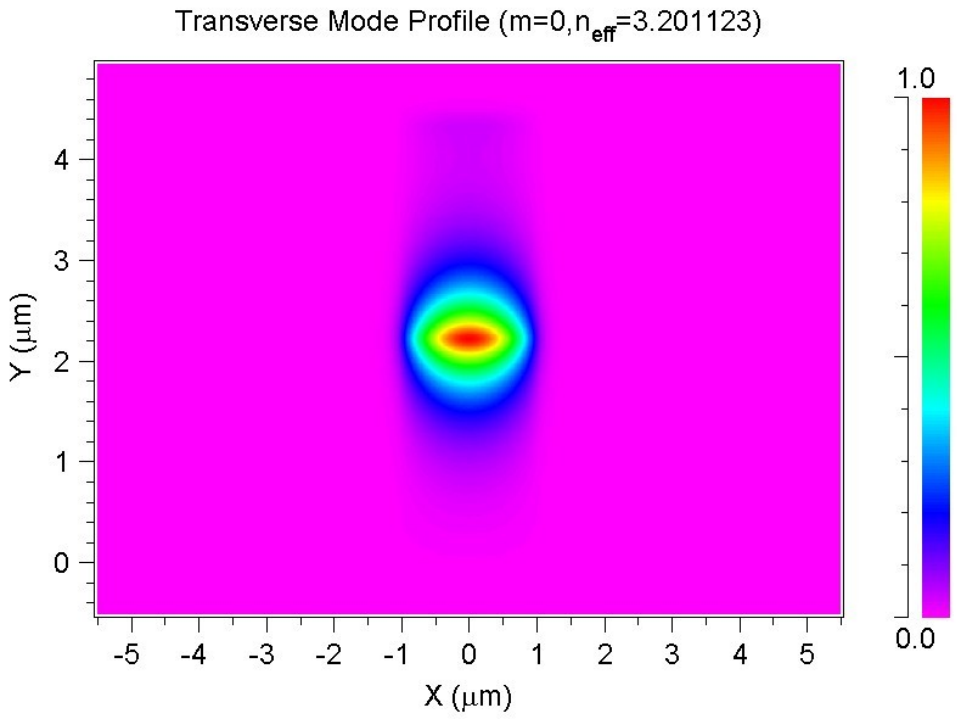

Figure 35. Calculated optical mode profile at the etch depth of 4 μm (totally etch through QWs active region).

In designing a real laser, some other aspects should be considered. Firstly, it is never a good idea to etch through the QWs. Dry etching can produce surface defects, which can subsequently propagate into the active region as dark spot defects (DSD) and dark line defects (DLD), and cause permanent catastrophic failure of the devices [61]. Also, the etching of lateral gratings to a depth of 4 μm is not a trivial matter, which will be discussed later in the chapter on fabrication.

The effect of the etch depth on the effective refractive index is shown in Figure 36. The refractive index stays constant when the etch depth is below 1 μm, where the optical confinement from ridge is very weak. As the etch depth increases, and eventually reaches

below active region, the effective refractive index decreases dramatically (especially for D_{etch} in the 1.5 μm to 2.2 μm range). After etching through the QWs, the effective index becomes stable again, since the optical field is almost totally confined by the etched ridge waveguide.

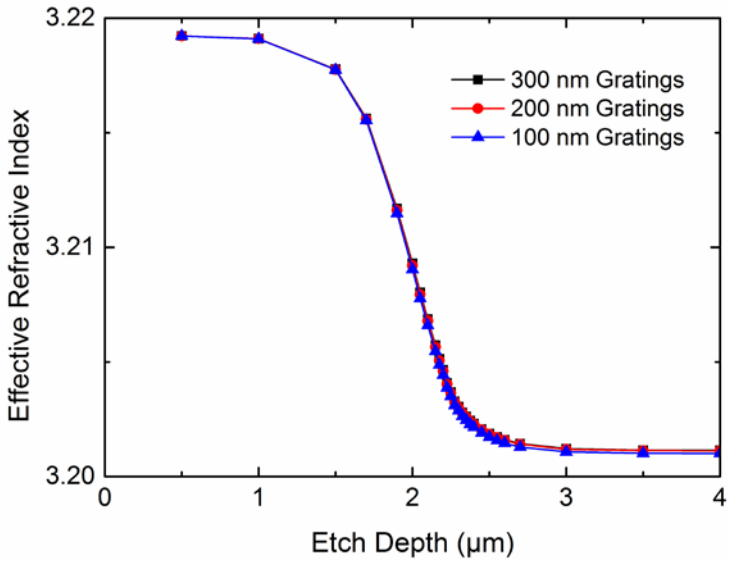

Figure 36. Calculated average refractive index *vs.* etch depth with different grating width.

The effect of the etch depth on the overlap factor has aslo been studied. The overlap factor increases when the etch depth is over 1.5 and stops growing after etching through the QWs. Only the optical field overlap with the current injection region contributes to stimulated emission. When the ridge etch depth is shallow, a large portion of the optical field is not confined (anti-guided) in the effective current injection region (the optical field is gain-guided), leading to a smaller overlap factor. In this regime, devices with different lateral grating widths show almost identical overlap factors.

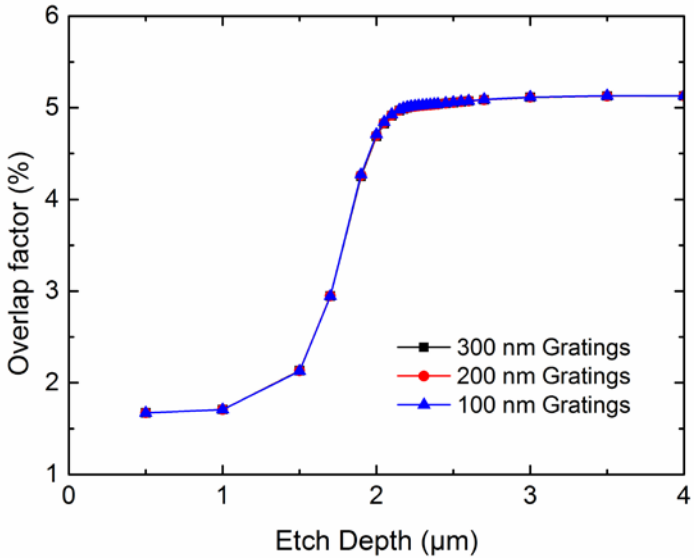

Figure 37. Calculated overlap factor *vs.* etch depth with different grating width.

Also, with respect to device design, the ridge needs to be etched to within 200 nm above active region to realize good index coupling (index confinement and grating coupling) while minimizing lateral current spreading. If the etch stops far above the active regions, the optical mode is confined entirely by injection current (gain coupling) rather than by index, which leads to a gain-guided device.

Therefore, based on all the above-mentioned factors, an optimized etch depth is 100 nm to 200 nm above active region.

3.2.3 Coupling efficiency *vs.* grating width

The dependence of the coupling efficiency on the lateral grating width has also been investigated. Different ridge widths with W_{ridge} equal 1.6 μm, 1.8 μm and 2.0 μm, respectively, were studied, with grating width $W_{grating}$ varying up to 1 μm on both sides.

The calculated κ *vs.* grating width is shown in Figure 38. It can be seen very straight-forwardly that as the grating width (*i.e.*, lateral grating depth) increases, κ goes up with κ increasing more slowly as the grating gets wider.

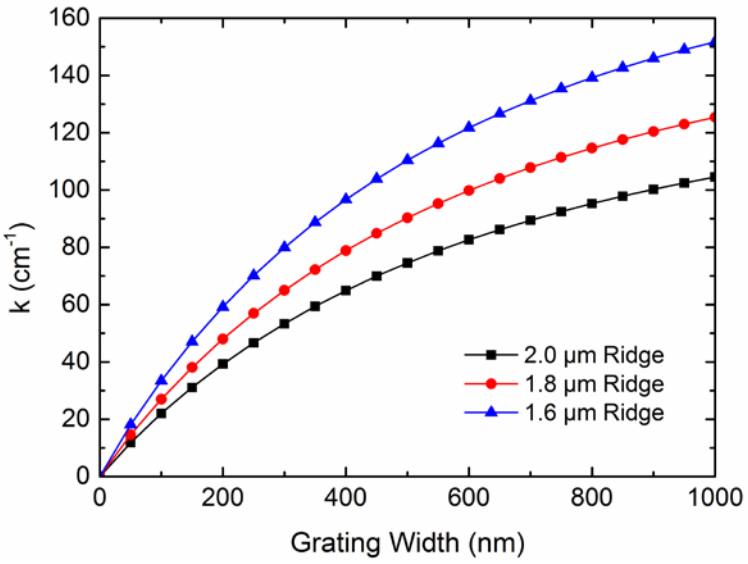

Figure 38. Calculated κ *vs.* grating width with different grating width.

The effects on grating width on the effective refractive index and the overlap factor have also been calculated.

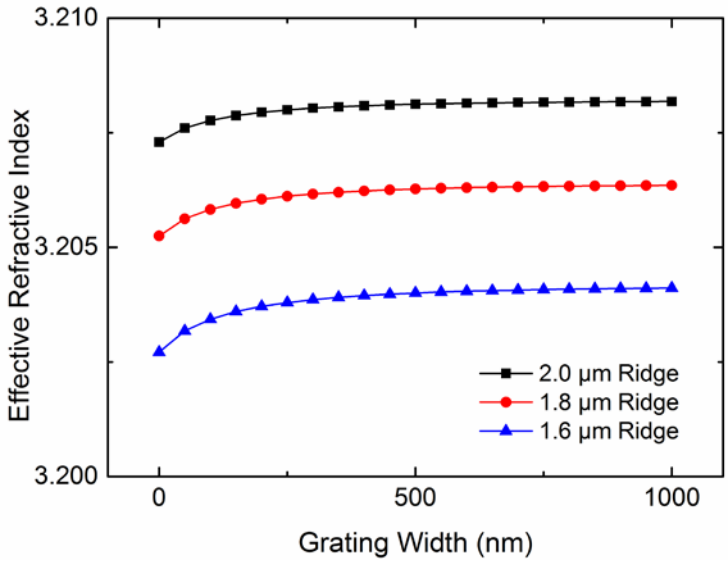

Figure 39. Calculated average refractive index *vs.* grating width with different grating width.

Figure 39 shows the calculated results of average refractive index *vs.* grating width. It can be seen that the grating width has a very small influence on effective refractive index (when assuming a fixed grating duty cycle of 50%), especially when gratings are wider than 300 nm. The optical mode is more confined by ridge waveguide without gratings. The effective index increases with etch depth due to the higher degree of real index confinement of the optical mode.

Figure 40 shows the overlap factor changing with different grating width.

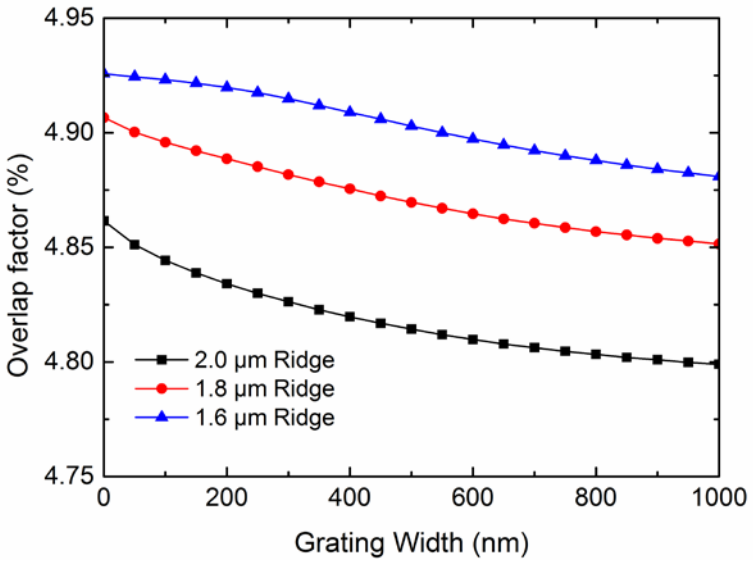

Figure 40. Calculated overlap factor *vs*. grating width with different grating width.

Grating width also has only a small influence on the overlap factors, which changes by less than 0.1% as the grating width varies from 0 to 1 μm.

How wide the lateral grating should be also depends on the ridge fabrication technology and subsequent processing. Generally, a lateral grating width between 200 nm to 300 nm is good enough for a DFB laser design.

In design considerations for a LC-DFB laser with EPS sampled grating, the coupling efficiency discussed in this section should be multiplied by 0.3183 reduction factor, as shown in Figure 20 (assuming a 1st order channel is used). Lasers with EPS sampled gratings have a lower coupling efficiency, and thus have a higher requirements for lasing performance.

3.2.4 Simulation of BH-DFB Lasers

An unique advantage of a BH laser is the mode shape. The BH lasers have an active region totally surrounded by low-index and high-bandgap InP material. InP materials that are undoped, Fe-doped, p-doped or n-doped have a very small difference in refractive index [62, 63], compared to the index difference between InP and other quaternary InAlGaAs or InGaAsP layers, or between InP and dielectric layers (i.e. Silicon Dioxide, Silicon Nitride, or Silicon Oxi-nitride).

Doping induced free carriers are the main factor affecting refractive index in that free carrier plasma reduces refractive index [64]. Also, due to the low effective mass of electrons, the free-carrier effect on index is much stronger in n-doped materials in III-V compounds. Fe-doped InP is a semi-insulating material, which doesn't introduce additional carriers, so it has a similar refractive index as un-doped InP.

The active region of a BH laser is completely surrounded by InP material (irrespective of doping). The surrounding InP has almost the same lower index, resulting in a more symmetrical *near-field* optical mode shape for a BH laser. Figure 41 shows a calculated optical mode profile of a BH laser, which has a nearly round shape compared to the one shown in Figure 28 for a LC-DFB RWG laser, which has an irregular mode shape due to the index-guided ridge structure.

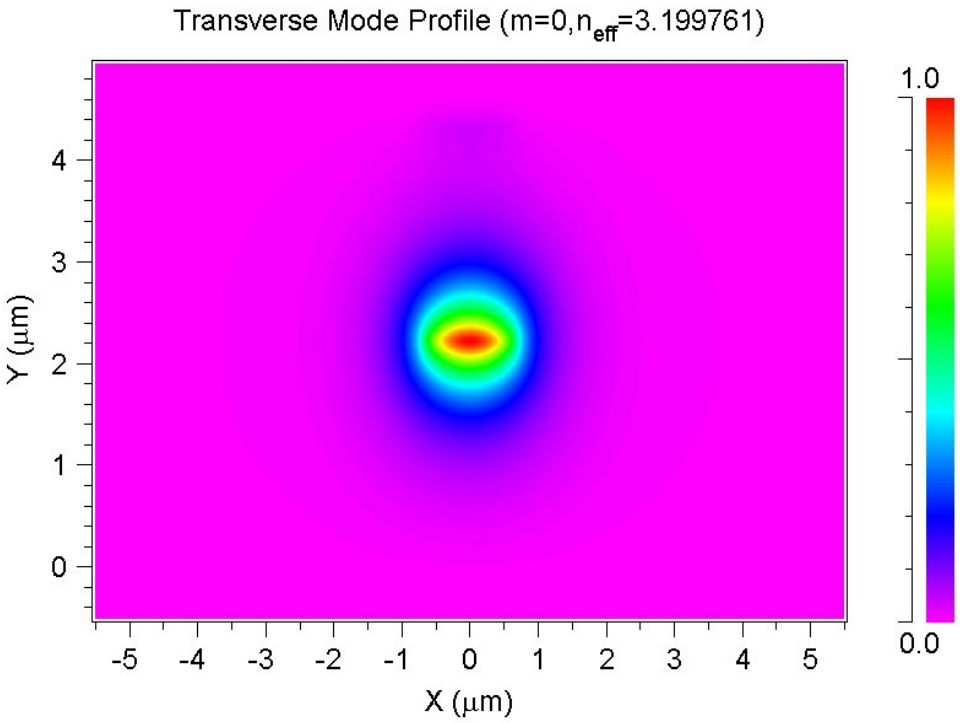

Figure 41. Calculated optical mode profile of BH lasers with active region width of 1.4 μm.

The design of κ in BH-DFB lasers is more straightforward compared to LC-DFB lasers. There are mainly three factors affecting κ: the distance of the grating layer to the active region, the thickness and shape of the grating layer, and the material compositions and index contrast of the grating layer. The coupling κ is larger when the grating layer is closer to the active region, and is thicker or has higher index contrast. When the quaternary layer has a longer photoluminescence wavelength,, the refractive index contrast is also higher, and κ is larger. So κ can be adjusted and calculated easily for a desired purpose.

3.3 Setup and Process of Interference Lithography

To fabricate DFB lasers without EBL, an optical interference lithography (IL) tool was set up, and a whole set of processing procedures for IL grating fabrication and etching was developed.

Figure 42 shows the Lloyd's mirror setup for IL tools [65]. The semiconductor sample to be exposed is positioned on a sample stage, which is set at a 90° angle with respect to an aluminum mirror (>90% reflection, λ/10 flatness). A coherent He-Cd UV laser beam is projected onto the 90° sample-and-mirror geometry, at an angle θ relative to the aluminum mirror, which is adjustable.

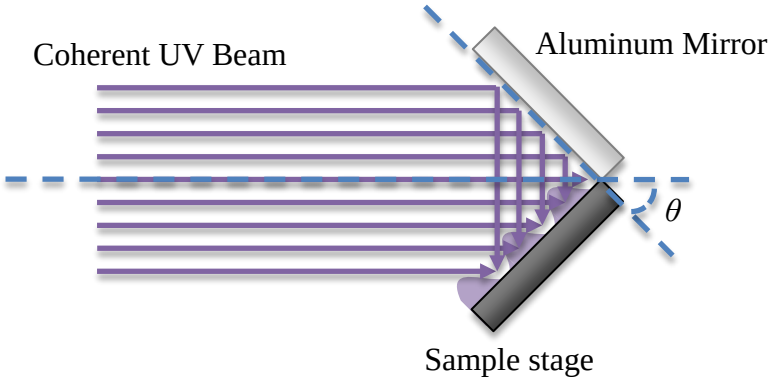

Figure 42. Lloyd's mirror setup for interference lithography.

Light reflected from the mirror is added to the light directly incident on the sample stage, and coherently form an interference pattern. The interference pitch can be calculated using Eqn. 22:

$$\Lambda = \frac{\lambda_{UV}}{2 \sin \theta}$$

Eqn. 22

A Kimmon Helium-Cadimium UV laser is used, which produces a constant 50 mW CW TEM_{00} output power at a 325 nm wavelength. The grating pitch needed for 1550 nm laser emision is Λ~ 240 nm. The stage rotation angle needed (from Eqn. 22) is around 45º, which is optimized for a balanced interference beam (the two interfering beams are compatible in amplitude).

The physical layout of the lithography setup is shown in Figure 43:

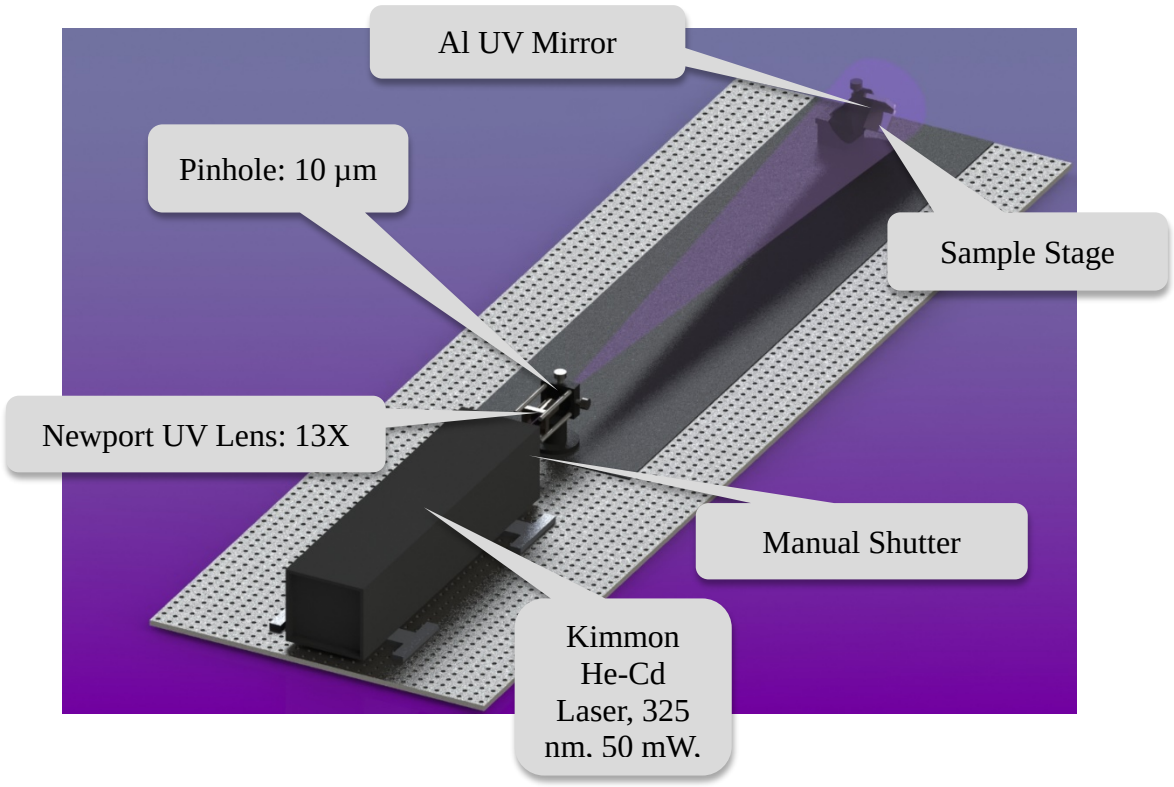

Figure 43. Illustration of interference lithography setup.

To fabricate Bragg gratings, the photoresist has to meet some key requirements. Firstly, since a 325 nm laser is used as light source, the photoresist should have good sensitivity at this wavelength. Secondly, the thickness of the photoresist to be patterned is very critical. Photoresist is to be patterned for ~100 nm features, and the interfering optical field intensity is sinusoidal in shape. So the photoresist should be thin enough for this purpose, since the exposure in power-limited, which is further exacerbated when the beam is expanded for large-area exposure. However, the photoresist used here must also be sufficiently thick to transfer the exposure pattern to a SiO_2 layer, which serves as a hard mask for subsequent grating etching. Thirdly, the exposure and develop times should be controllable.

Several different photoresists have been considered for the grating fabrication, *e.g*., SU-8 2002, Futurrex NR9-250P, AZ 5209, *etc*. After investigation, diluted AZ-5214E-IR with image reversal process is used for the grating fabrications. AZ-EBR is used for dilution to reduce the thickness of the photoresist.

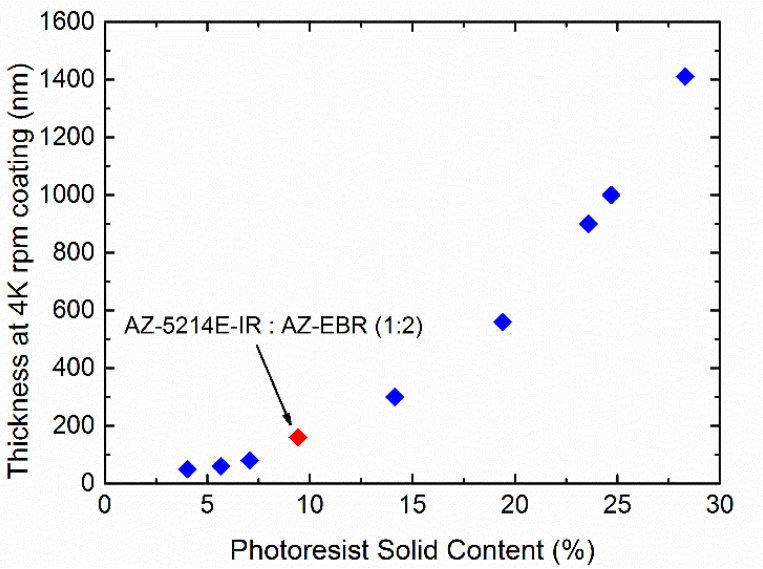

Figure 44. Photoresist thickness with different solid content.

Figure 44 shows the photoresist thickness with dilution. AZ-5214E-IR : AZ-EBR at 1: 2 diluted solution is used. The film thickness of diluted photoresist is 160 nm, and the solid content is 9.43%. The process flow for grating fabrication is shown in Table 3.

Photoresist	AZ-5214E-IR: AZ-EBR (1:2)
Thickness	160 nm
Spin Coating	40s at 3000 rpm
Pre-bake	1 min at 110 ºC
Exposure	60s using customized setup
Post-bake	2 min at 120 ºC
Flood Exposure	1 min using MJB 4 or MA 6
Develop	15s in AZ 726 MIF

Table 3. Process flow for interference lithography grating fabrication.

The exposure time under the IL setup is ~60 s. Since the exposure time is sufficiently long, shuttering is manually controlled. The image reversal process is used to partially compensate the effect of a sinusoidal light distribution on the exposed resist profile. The development time using AZ 726 MIF is ~ 15s, which is manually controllable. For a better control, a diluted developer can be used.

Figure 45 and Figure 46 show the scanning electron microscope (SEM) images of the patterned gratings on photoresist using this method, which is of much better quality than some reports from industry [66].

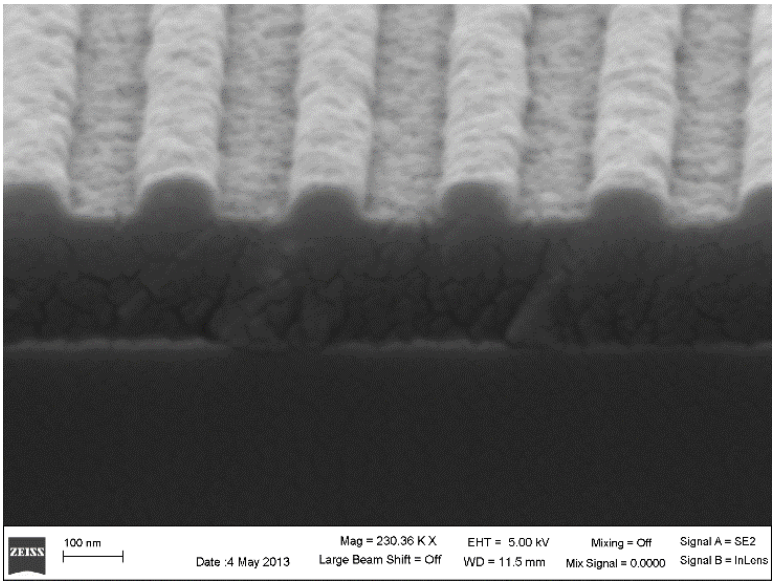

Figure 45. SEM photo of grating on photoresist (side view)

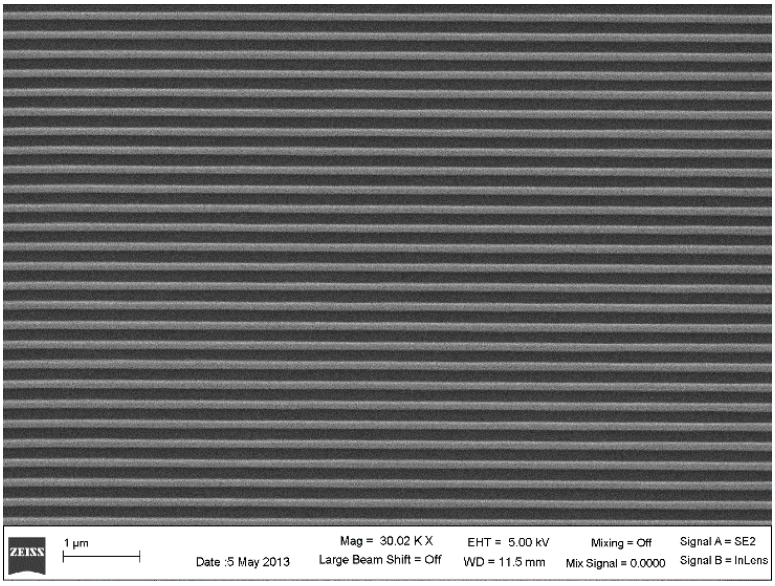

Figure 46. SEM photo of grating on photoresist (top view)

Also, a grating patterned by non-image-reversal process is shown in Figure 47. The sinusoidal shape grating is very obvious compared to Figure 45.

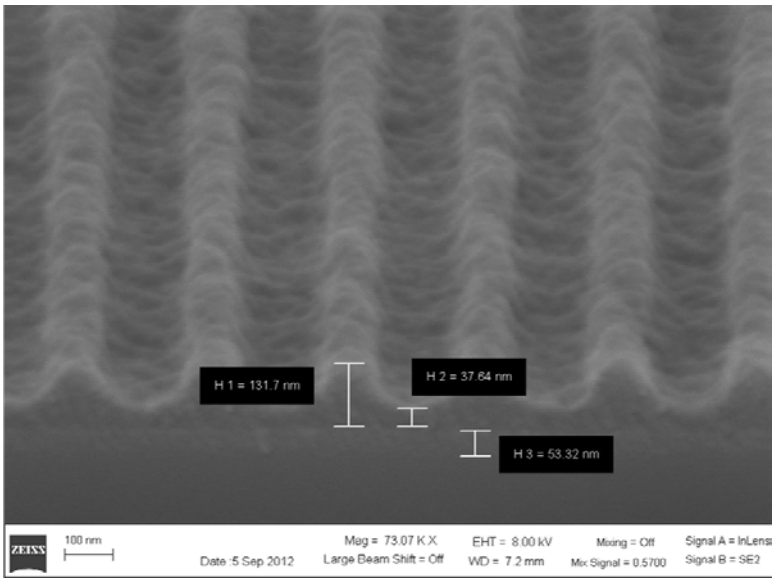

Figure 47. SEM photo of gratings on photoresist without image reversal process

The quality of the gratingtransferred to a SiO_2 hard mask is also investigated. The side view and top view of a SiO_2 grating are shown in Figure 48 and Figure 49, respectively.

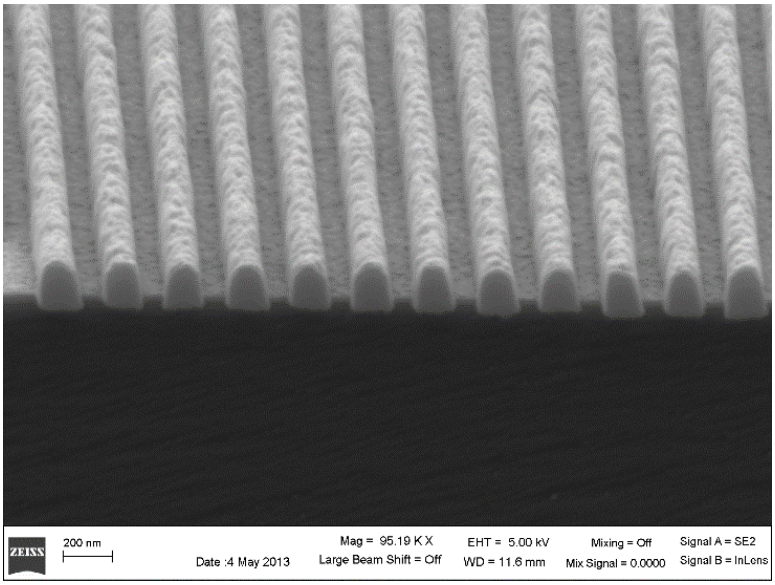

Figure 48. SEM photo of gratings on SiO_2 hard mask (side view).

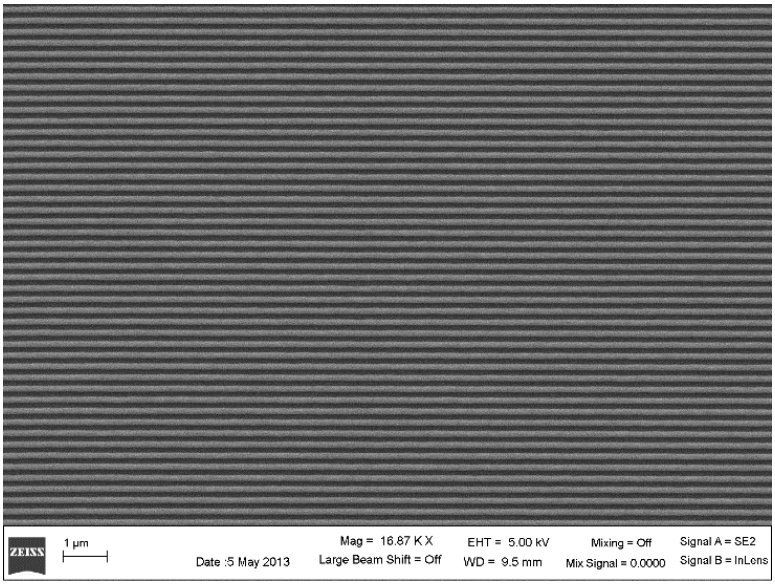

Figure 49. SEM photo of gratings on SiO_2 hard mask (top view).

An important advantage of the IL process is its ability to pattern gratings across a large area simultaneously. Figure 50 shows a sample, 1 cm by 1 cm in size, which is patterned with uniform gratings by IL. The blue color is the diffraction color from the gratings. Only the edge of the sample has some area that without gratings due to photoresist edge bead pile-up.

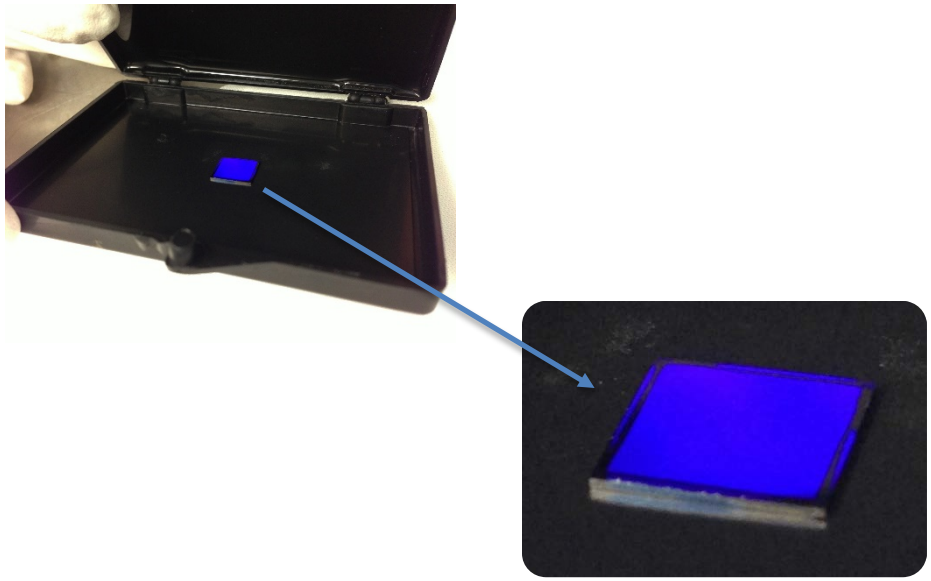

Figure 50. IL Gratings patterned on 1 cm by 1 cm samples.

Grating pitch of the setup has been calibrated for the wavelength span from 1530 nm to 1650 nm.

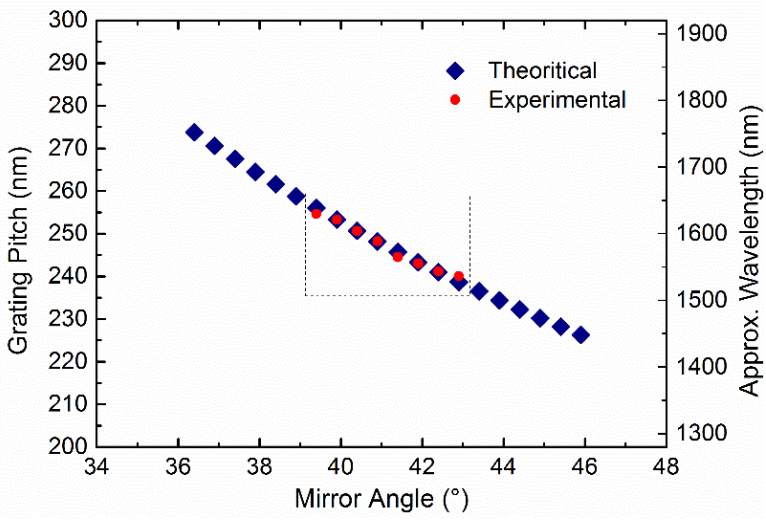

Figure 51. Grating pitch calibration. experimental results (red dots) compared to theoretical value (blue diamond).

Some slight deviation is observed in the experimental grating pitch compared to the theoretical design value, which is attributed to error induced by manual adjustment of the rotation stage, which is used to adjust θ for the sample holder according to Eqn. 22. For better accuracy, a more precise mechanical rotation stage is needed. In my experiment, the grating pitch is calibrated every time before fabrication on the actual device wafers.

One more thing should be mentioned is that the light from the setup shown in Figure 43 is not strictly a collimated (parallel) beam. So it may induce errors due to parallax when the beam is expanded for larger scale.. But from the calculation discussed in [67], the total beam angle α is ~ 0.8º, corresponding to an error of -0.0024%, which is negligible compared the manual stage manipulation errors.

Chapter 4: Laterally-Coupled DFB Lasers

4.1 Fabrication of LC-DFB Lasers

The fabrication of BH lasers has been studied and implemented by in industry for many year. This section will focus on the fabrication of LC-DFB lasers.

Among the reported LC-DFB lasers, grating definition has been achieved using e-beam lithography (EBL) [23, 33, 34, 39, 68], optical interference lithography (IL) [37, 69], stepper technology [38, 40], or nanoimprint lithography (NIL) [35, 41]. To the best of our knowledge, LC-DFB lasers with first-order gratings have only been fabricated by using EBL [23, 39, 68]. However, EBL is an expensive and time-consuming process with low throughput, which is not scalable for high-volume manufacturing [25, 26, 37]. In contrast, conventional optical interference lithography is low-cost, has high throughput, is more suitable for and is widely used in mass production.

But unlike EBL, stepper technology, or NIL, optical interference lithography is good for patterning uniform features in one dimension over a large surface area, and has limited capability for patterning arbitrary features in two dimensions due to its inherent mechanism. In addition, optical interference lithography is incapable of patterning gratings on non-planar surfaces, such as the sidewalls or corners of a ridge waveguide laser, due to the lack of mechanical precision and the limited depth of field of optics.

One potential solution is to etch a ridge first, and then expose interference grating on ridge sidewalls and at the trench bottom. But if ridge is etched first, the coating of photoresist on a non-planar surface topography tends to be very non-uniform, as shown in

Figure 52. Photoresist thickness at ridge sidewall will pile up, and can be several times thicker compared to the flat regions, which will cause severe exposure problems.

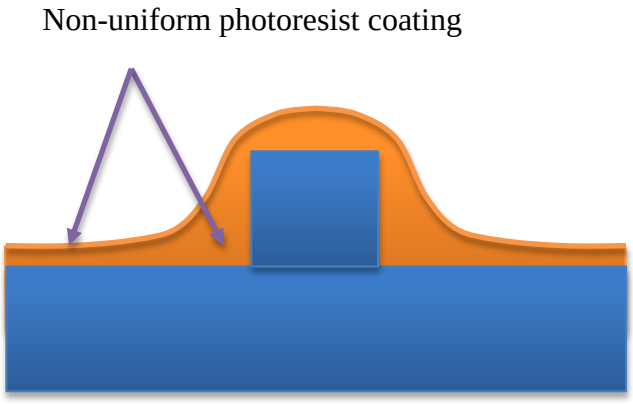

Figure 52. Illustration of photoresist coating on non-uniform surface.

Figure 53 shows the SEM image of gratings patterned after ridge etching. No gratings exist in the regions close to ridge sidewalls, also a pattern distribution perpendicular to grating directions is observed which is due to the constructive and destructive reflection patterns resulting from the variations in photoresist thickness.

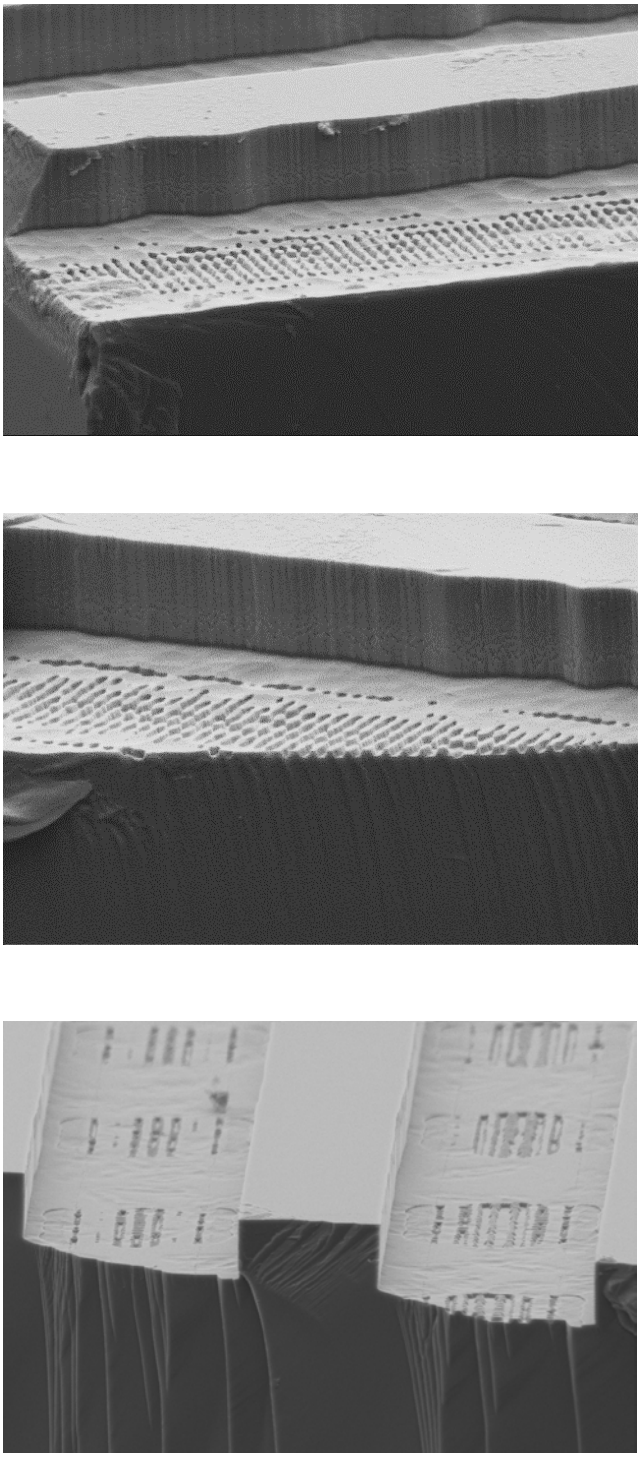

Figure 53. Gratings patterned after etching ridge. Non-uniform photoresist spun causes great problem in patterning interference gratings.

Another potential solution is to pattern the first-order grating on the top planar surface, and then transfer to the semiconductor via anisotropic dry etching. However, it is very difficult to etch gratings with the ultra-high aspect ratio (20:1) required [35]. The etching of deep, and narrowly enclosed submicron features is severely limited by the diffusion and transport of reactants and reaction by-products through deep and narrow channels. By adjusting etching recipe, the deepest etch for first order gratings the author reached is ~ 800 nm (shown in Figure 54, top), which shows similar result as reported in [70]. It can be seen that the etch channel is closed, and the barriers between channels are very thin. If etching is continued, the barrier will be etched through and the hard mask will eventually peel off (shown in Figure 54, bottom), resulting in a total failure.

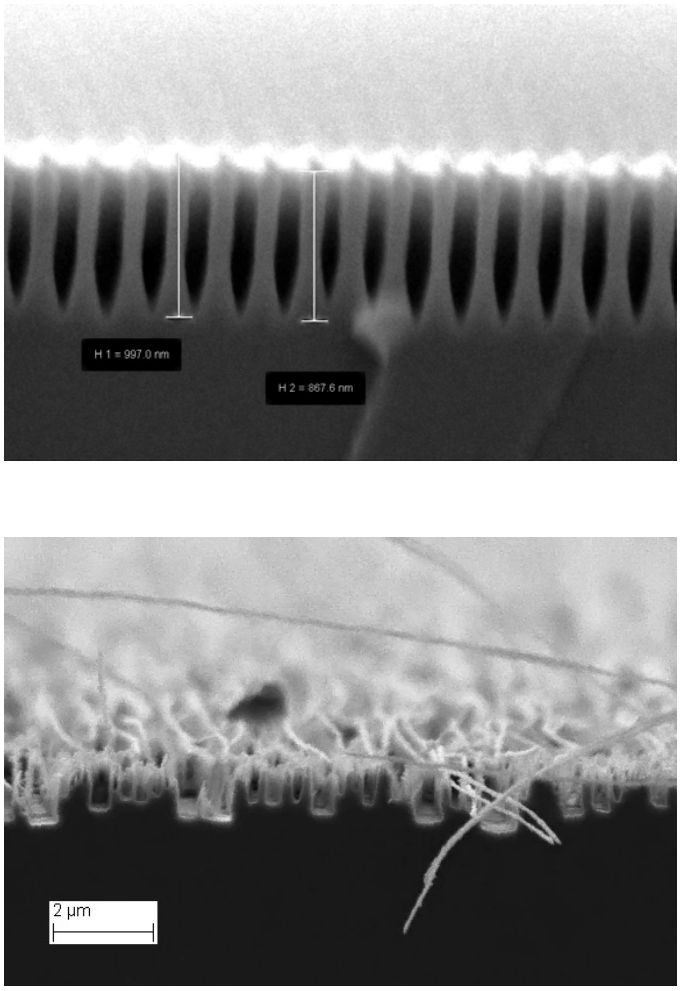

Figure 54. Gratings directly etch from top surface of III-V epi-wafer. Left: deepest etch reached: 800 nm; right: after continued etching of the same sample.

Among all LC-DFB lasers reported to date that are not based on EBL, only higher-order Bragg gratings have been achieved (*e.g.*, second order gratings with non-1:1 aspect ratio [69], third-order gratings [33, 35, 38, 41], or fifth-order gratings [33]). Higher-order gratings have much longer pitches, which are much easier to fabricate, but the grating coupling efficiency is greatly reduced [40, 68, 71]. So far, no first-order lateral gratings or LC-DFB lasers has been realized by optical interference lithography.

To solve the aforementioned problem, a brand new method is developed in this dissertation to fabricate laterally-coupled gratings.

To fabricate the lateral gratings, a very high quality grating mask is needed. To obtain a SiO_2 hard mask layer, a SiO_2 layer is first deposited at 270 ºC on the surface of the III-V epi-wafer by plasma-enhanced chemical vapor deposition (PECVD). PECVD films usually have higher quality when deposited at higher temperature. Choosing 270 ºC as depositing temperature is because InP materials tends to start decomposing at 300 °C. Details of SiO_2 PECVD deposition conditions are as follow :

Tool	Plasma-Therm 790 PECVD
Temperature	270 ºC
Pressure	300 mTorr
RF Control	By power, 50 mW
Gas flow: N_2O	42
Gas flow: SiH_4	21
Deposition rate	45 nm / min
Notes:	(Sample size: < 2 cm * 2 cm)

Table 4. SiO_2 PECVD deposition conditions.

The SiO_2 PECVD deposition rate is related to sample size. A larger sample results in a slower rate. Film thickness and index parameters are fitted by using a J.A. Woollam Ellipsometer. The refractive index at 1550 nm is 1.4507, with Cauchy coefficients of B: 1.447175; C: 0.00221419 /μm^2; D: 8.11198 × 10^{-5} /μm^4 [72]. The deposition rate is ~ 45 nm /min. For electrical isolation purpose, the thickness of the dielectric is not critical.

Next, the optical interference lithography setup is used to pattern the photoresist on top of the SiO_2, which resides on a planar surface. The gratings are then etched into the SiO_2 mask by reactive-ion etching (RIE) (Figure 55 (a)). The recipe for reactive ion etching (RIE) of SiO_2 is shown in Table 5. In this step, fluorine reacts with SiO_2 to form the volatile SiF_4 as reaction byproduct.

Tool	Oxford PlasmaLab 80 Plus
Temperature	Room temperature
Pressure	15 mTorr
RF Power	100 mW
Gas flow: SF_6	3
Gas flow: CHF_3	20
Gas flow: Ar	15
Etch rate	15 nm / min
Notes:	Sample size not critical

Table 5. SiO_2 RIE etch process using Oxford PlasmaLab 80.

The RIE etch rate ratio of SiO_2 compared to photoresist is around 3:1. So the photoresist layer of over 100 nm is thick enough to cover a 300 nm SiO_2 layer. The etch rate ratio of III-V semiconductor (here InP/InGaAsP/AlInGaAs) to SiO_2 is over 10:1, so the thickness of the SiO_2 mask is chosen to be 250 nm.

The next step is to pattern the ridge waveguide using another photoresist layer (Figure 55 (b)). This is a critical step in the whole process for several reasons. The photoresist used here forms a mask layer for later patterning and etching of the ridge trench, so a robust resist layer is needed. This resist layer cannot be too thick, because the pattern

linewidth is ~ 2 μm, and needs to be very accurate. Also, this photoresist layer should be able to withstand a relatively high temperature, since the dry etching of III-V material is at a substrate temperature of 60 ºC.

Negative photoresist SU-8 2002 is used for this step. For good adhesion, a layer of Omnicoat is first applied before SU-8. Details of ridge patterning is listed in Table 6:

Photoresist: 1st layer	Omnicoat
Coating process	100 rpm / s ramp up to 500 rpm
	5 s at 500 rpm
	300 rpm / s ramp up to 3000 rpm
	30 s at 3000 rpm
Bake	1 min at 200 ºC
Estimate thickness	10 to 20 nm (not critical)
Photoresist: 2nd layer	SU-8 2002
Coating process	100 rpm / s ramp up to 500 rpm
	5 s at 500 rpm
	300 rpm / s ramp up to 3000 rpm
	30 s at 3000 rpm
Pre-bake	2 min at 95 ºC
Exposure	MA 6, 13s, vacuum contact
Post-bake	2min at 95 ºC
Develop	SU-8 developer, 60 s
Cleaning	IPA
Thickness	2 μm

Table 6. Process flow of ridge photoresist patterning.

When using SU-8, a gradual ramp-up in spin coating is very important, or the thickness will be much thinner than expected. No hard curing is performed. Here, SU-8 is used as an etch mask, and no obvious difference is observed with or without a hard cure.

Another $CHF_3/SF_6/Ar$ RIE process (Table 5) is used to remove the SiO_2 gratings from the uncovered areas of the photoresist (Figure 55 (c)), exposing the III-V surface for etching of the ridge trenches. Next, a pure oxygen RIE process is used to partially etch away a certain thickness of photoresist from each edge of the ridge photoresist mask, thereby exposing a center width of SiO_2 gratings along each sidewall of the ridge (Figure 55 (d)). The oxygen RIE etch rate of photoresist is very constant, so the lateral width of the SiO_2 gratings exposed can be controlled precisely. Also, it is a self-aligned process that does not depend on the photo mask and photolithography, but by the control of the photoresist edge removal. This process results in the formation of a two-layer mask (Figure 55 (d)): the remaining SU-8 photoresist now acts as a mask for etching the ridge in the region without gratings, while the narrow but exposed SiO_2 gratings provide a mask for etching the deep lateral grating into both sidewalls as the trenches are etched.

Inductively-Coupled Plasma (ICP) etching with $Cl_2/CH_4/H_2$ is used for the anisotropic etching of the III-V InP/InGaAsP semiconductor materials (Table 7). The substrate is pre-heated to 60 ºC.

Tool	Oxford PlasmaLab System 100
Temperature	60 ºC
Pressure	4 mTorr
RF Power	175 mW
ICP Power	2000 mW
Gas flow: Cl_2	8
Gas flow: CH_4	4
Gas flow: H_4	7
Etch rate	~ 2 µm per 90 s
Notes:	Sample size critical

Table 7. ICP dry etch process for InP/InGaAsP materials.

The ICP etch rate is sensitive to both substrate temperature and sample size. According to this process, the etch rate rises eventually with etch time, so multiple runs are helpful when the etch depth is critical. Another thing is, aluminum-containing materials are very sensitive to oxygen in the etching environment. So a tiny amount of oxygen in the etching gas can be used for selective etching. When etching reaches the aluminum-containing layers, the aluminum tends to oxidize, which greatly slows down etching rate.

Since the ICP etch is highly directional, the pattern on the SiO_2 mask can be transferred to a great depth, while the narrow lateral width of the gratings largely eliminated the reactant transport problems, since the trench is totally open, which enables reactants and byproducts to laterally access the narrow grating regions.

The ridge and gratings can be etched to a depth of over 2 µm, (Figure 55 (e)). Then the photoresist is removed by a RIE process using pure oxygen. The SiO_2 grating masks

are then removed by a Buffered Oxide Etch (BOE), which consists of a Hydrofluoric Acid/water solution with a HF : H_2O (1:6) ratio, leaving the etched ridge with gratings on both sidewalls of the ridge waveguide (Figure 55 (f)). It should be noted that BOE attacks aluminum-based materials. So if the wafer contains aluminum, a photoresist protection layer is needed at SiO_2 removal step.

To make a LC-DFB laser, another SiO_2 layer of 500-1000 nm thickness is deposited by PECVD for electrical isolation, followed by opening of the contact window on top of the ridge (Figure 55 (g)). SiO_2 has a thermal expansion coefficient of 5×10^{-7} / ºC, which is smaller than that of InP (4.6×10^{-6} / ºC). So stress exists at the interface between the two materials. SiN_x has a thermal expansion coefficient of 3.2×10^{-6} / ºC, which is more closely matched to InP. However, the quality of SiN_x that can be deposited here is not as good as that of SiO_2, so it is not used in device fabrication. Mixed films such as SiO_xN_y with zero stress can also be used for this purpose. By adjusting the percentage of oxygen and nitride in the film, zero stress films can be achieved.

The metallization is then performed on both the top and bottom sides of the wafer (Figure 55 (h)). The N-contact contains a 10 nm titanium adhesion layer and a 250 nm gold contact layer. The P-contact contains a 10 nm titanium adhesion layer, a 10 nm platinum blocking layer, and a 250 nm gold contact layer. The platinum blocking layer serves as barrier against gold migration into the active region. After cleaving the wafer into dies, the fabrication process is almost complete, but for the facet coating layer.

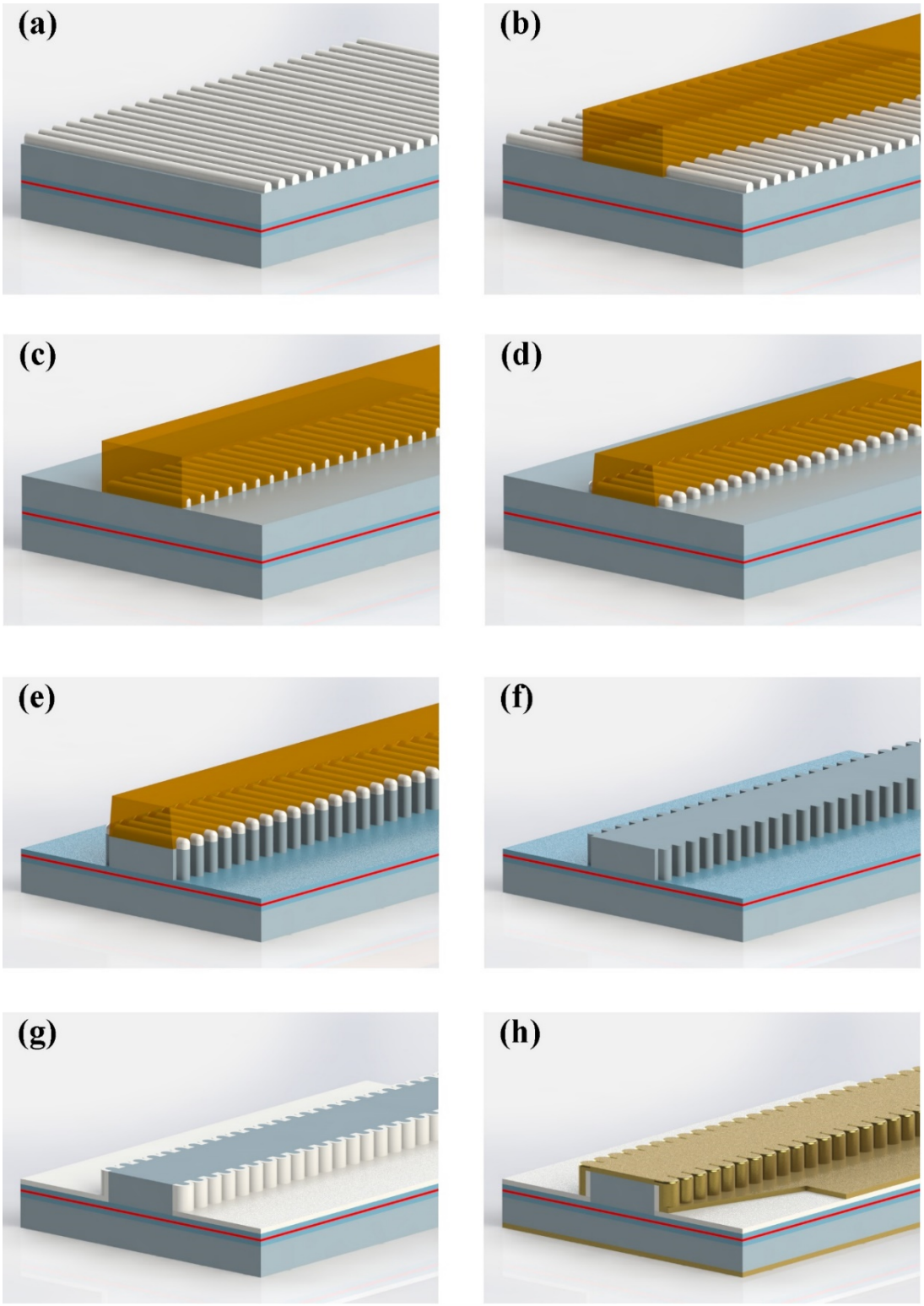

Figure 55.

Figure 55. Illustration of the fabrication process of the proposed first-order lateral gratings and LC-DFB lasers. (a) SiO_2 grating mask on the planar epi-wafer surface; (b) The ridge patterned on photoresist; (c) Removal of SiO_2 on open ridge trench area; (d) Oxygen RIE removal of photoresist to expose the SiO_2 grating mask on sidewalls of ridge; (e) ICP etch of ridge and sidewall gratings; (f) Photoresist and SiO_2 grating mask removal; (g) SiO_2 electric isolation and contact window opening; (h) Metallization.

Figure 56 and Figure 57 shows the SEM images with two stacked layer of masks, which corresponds to Figure 55 (d). It can be seen that the lateral SiO_2 gratings have been exposed on both sides of the ridge, which act as etching masks for the LC-grating etching. This test sample is fabricated on a Silicon substrate. So when semiconductor etching occurs through the open regions of the SiO_2 gratings, the gratings are partially transferred into the silicon wafers, leading to a visible shallow gratings in the open region.

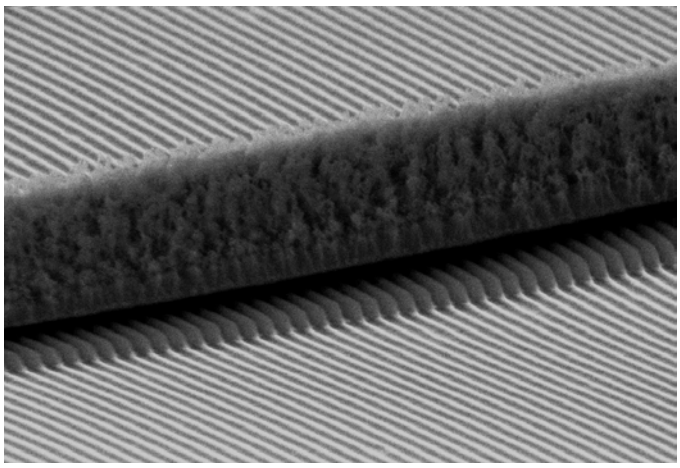

Figure 56. Side view SEM images of sample wafer after fabrication of the two-layer self-aligned mask (corresponding to Figure 55 (d)).

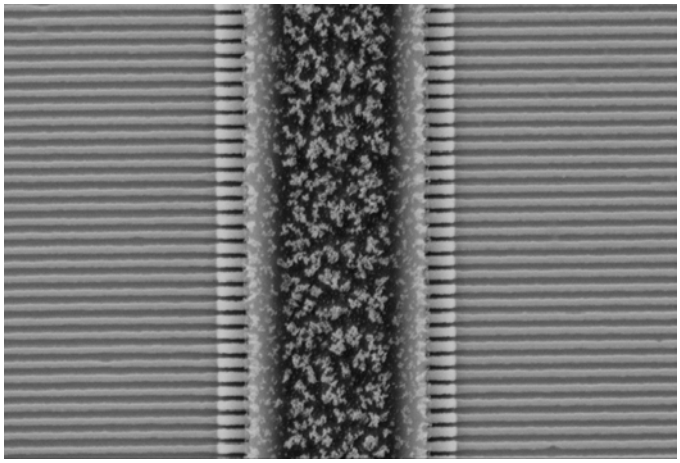

Figure 57. Top view SEM images of sample wafer after fabrication of the two-layer self-aligned mask (corresponding to Figure 55 (d)).

Using this proposed method, first-order lateral gratings have been fabricated using optical interference lithography and a (cannot be photomask free when you have two mask layers) self-aligned etching process using two stacked layers of masks (Figure 58). The grating width can be precisely controlled by the RIE patterning of the photoresist mask. Figure 58 (a) shows the ridge waveguide fabricated without photoresist removal by RIE (Figure 55 (d)). It can be seen clearly that, only some shallow remnants of gratings are formed on the III-V ridge surface, and no grating is transferred to the bottom of the ridge waveguide. Figure 58 (b) to (e) show lateral gratings with the lateral width of 100 nm, 200 nm, 300 nm and 500 nm, respectively.

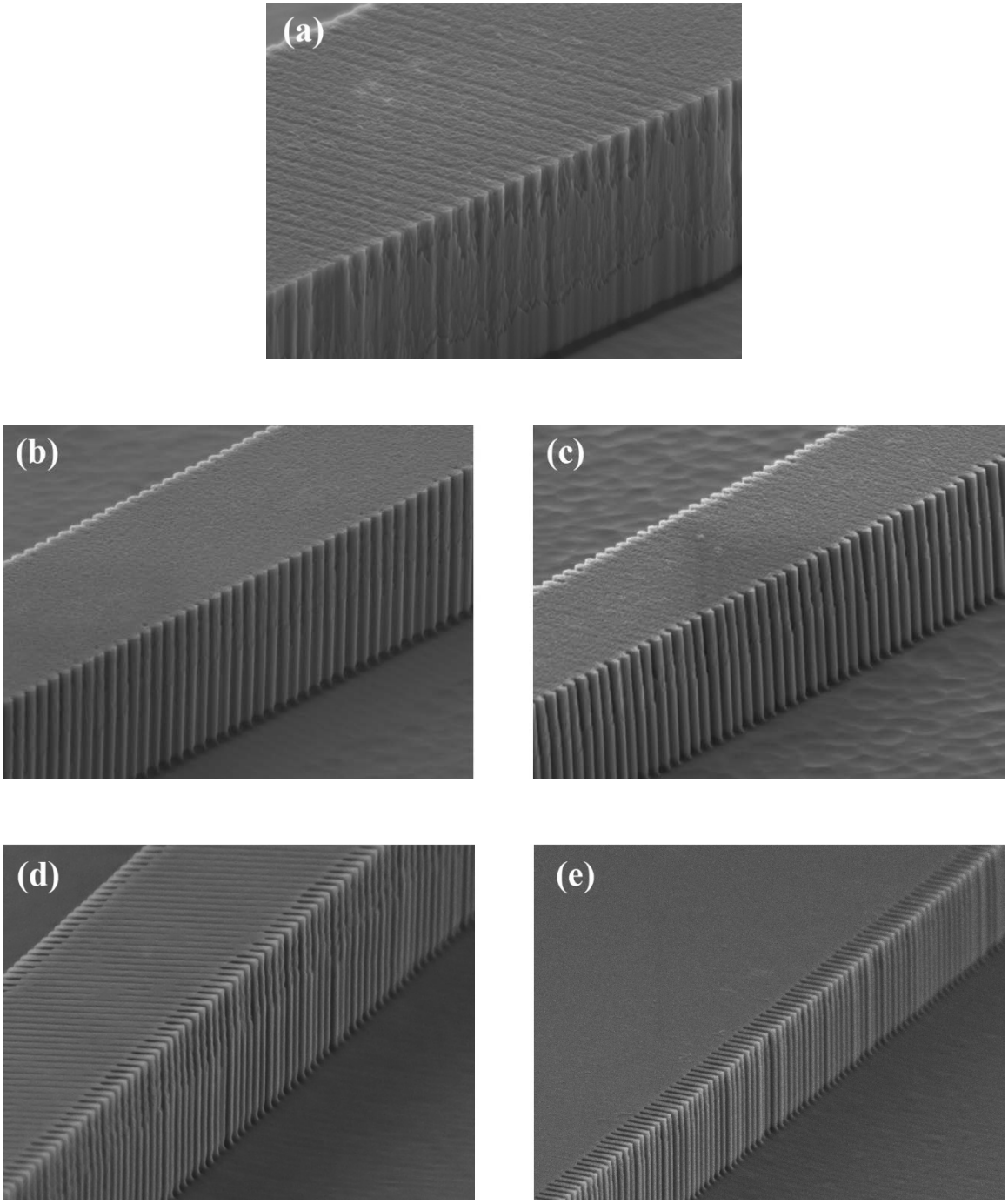

Figure 58. No RIE photoresist removal, and no gratings is formed on the sidewalls; (b) 100 nm wide sidewall gratings; (c) 200 nm wide sidewall gratings; (d) 300 nm wide sidewall gratings; (e) 500 nm wide sidewall gratings.

4.2 PERFORMANCE OF LC-DFB LASERS

Based on the fabrication method described in Chapter 3, LC-DFB lasers with first-order gratings fabricated by optical interference lithography [65] have been demonstrated experimentally. As mentioned earlier, the first-order grating is first defined and patterned into a SiO_2 dielectric mask on the top planar wafer surface, and is then transferred to both sidewalls of the ridge by a two-layer mask and self-aligned etch process during the etching of the ridge waveguide sidewalls.

The lateral gratings can be etched down to a depth of more than 2 μm, and the lateral width of the gratings can be controlled precisely from 100 nm to 500 nm. For grating features with a half-pitch of ~100 nm, the etching aspect ratio can be as high as 20:1 due to the widely open ridge trench region that allows reactants and reaction bi-products to escape.

Using this technique, LC-DFB ridge-waveguide lasers with an AlGaInAs/InP multi-quantum well (MQW) epi-structure have been fabricated [73]. The laser cavity length is 650 μm, the ridge width is 2.6 μm / 2 μm with/without lateral gratings. Both ridge and gratings are etched to a depth of 2 μm, which is 150 nm above the Quantum Wells (QWs) for optimized performance.

These LC-DFB lasers achieved continuous-wave (CW) lasing operation with stable single-longitudinal mode operation at a wavelength of 1.55 μm over a wide temperature range. At room temperature (~25 °C), the threshold current density is 1.7 kA / cm^2, and single longitudinal mode lasing is achieved with a side-mode suppression ratio (SMSR) of 37 dB.

The grating pitch is defined according to the Bragg reflection condition Eqn. 4. For the laser, λ is selected to be 241 nm for λ = 1550 nm lasing.

The wafer used is an AlGaInAs/InP epiwafer designed for 1550 nm RWG lasers, and is grown by Metalorganic Vapor Phase Epitaxy (MOVPE) in a single growth run on a (100) n-doped InP substrate. The epilayer structure contains an n-doped InP buffer layer, followed by a 500 nm n-doped InP cladding layer, an active region, a 1.8 μm p-doped InP cladding layer, and a 200 nm contact layer. The active region consists of a Graded-Index (GRIN) separate confinement heterostructure (SCH), in which 5/6 AlGaInAs QW/barrier layers are bounded between p-doped and n-doped GRIN layers that include p-doped and n-doped InAlAs carrier confinement layers. The photoluminescence (PL) gain peak of the QWs is at 1535nm. The 200 nm contact layer contains a 50 nm p-doped InGaAsP layer and a 150 nm p-doped InGaAs layer.

The laser has a cavity length of 650 μm with cleaved and uncoated facets. The ridge width is designed to be 2.6 μm including 300 nm gratings on both sidewalls. Figure 59 shows a SEM picture of an actual device at the cleaved facet. Ti-Au is used for both p- and n- contact metals. The p-contact is deposited and patterned on the top surface, while the N-contact is deposited on the backside of the substrate. Some vestiges of the gratings on the ridge top and sidewalls are still visible after the metallization.

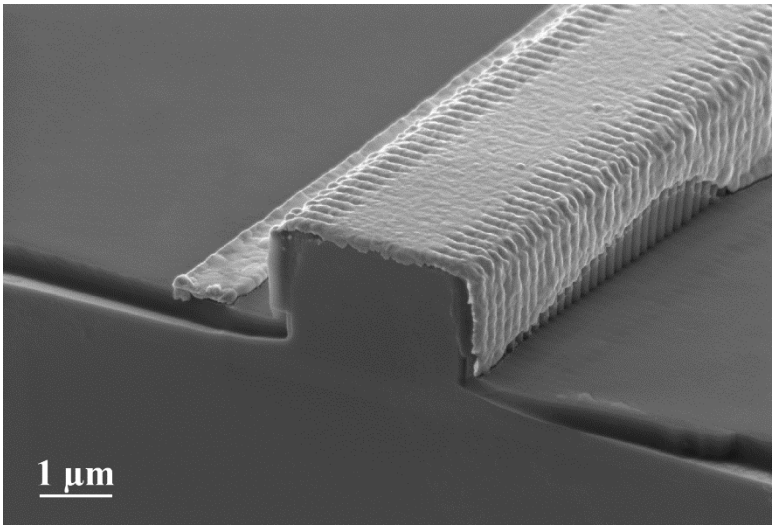

Figure 59. SEM picture of an actual DFB laser at a cleaved facet.

CW lasing is achieved over a wide range of temperatures. At room temperature, the threshold current is 28 mA, corresponding to a threshold current density of 1.7 kA/cm^2. Fig. 3.5 shows the lasing spectrum of the laser at twice the threshold current (56 mA) at room temperature (~25°C). Single longitudinal mode lasing is observed at 1552.8 nm, with a side mode suppression ratio (SMSR) of 37 dB.

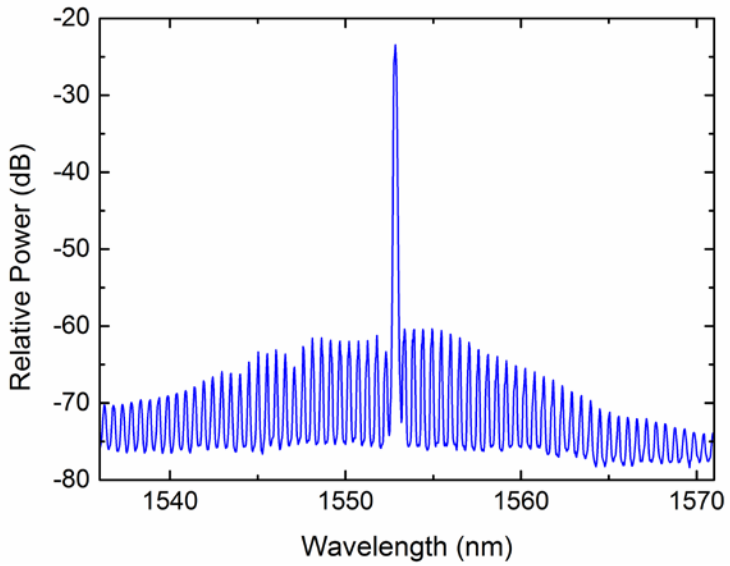

Figure 60. Lasing spectrum of a LC-DFB laser with first-order gratings made by optical interference lithography. The spectrum is taken at an injection current of 56 mA at room temperature. The lasing wavelength is 1552.8 nm with an SMSR of 37 dB. (The measurement is taken by an Agilent 86140B Optical Spectrum Analyzer, with an resolution of 0.07nm.)

Figure 61 shows the light-current-voltage (LIV) characteristics of the DFB laser at room temperature. The slope efficiency (S.E.) is 0.14 mW/mA per facet. The threshold voltage is ~1.0 V, with a series resistance of about 6 Ω. No substrate thinning or heatsinking were performed or used.

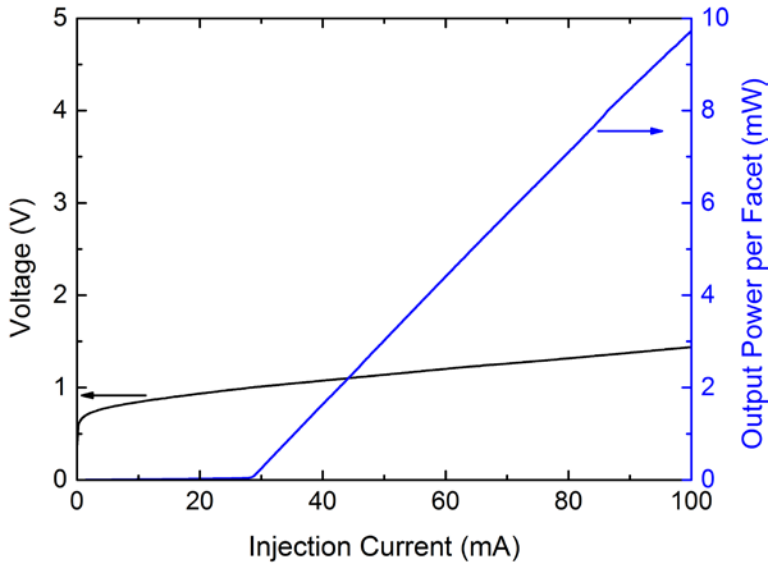

Figure 61. The cw lasing and electrical characteristics of the LC-DFB laser at room temperature. The output power is 9.73 mW per facet at 100 mA bias current.

The laser operates in a single longitudinal mode, with SMSR > 30 dB at an injection current ranging from 35 mA to 74 mA, and the SMSR stays above 35 dB from 45 mA to 63 mA (Figure 62). At higher injection currents, due to the red shift of the gain peak, another mode at a longer wavelength will be competitive and begin lasing, causing the SMSR to drop.

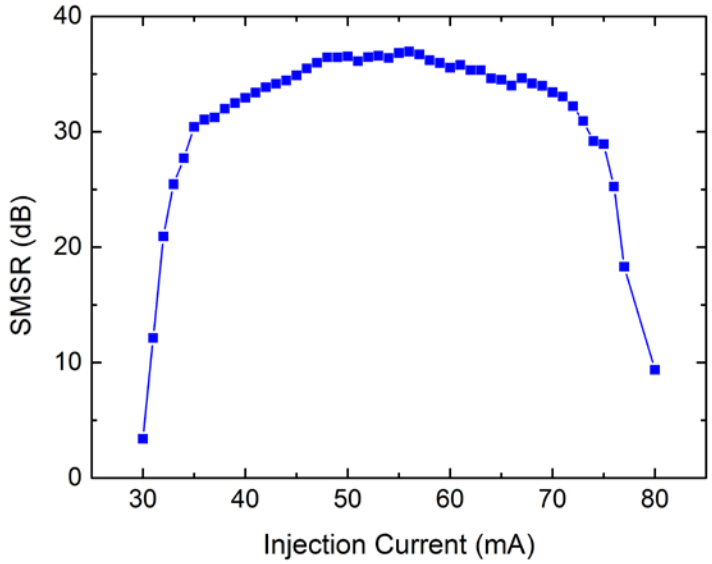

Figure 62. SMSR vs. Injection Current. The laser operates in a single mode, with an SMSR > 30 dB at the injection current from 35 mA to 74 mA, and the SMSR stays above 35dB from 45 mA to 63 mA.

The CW lasing (light *vs.* current) characteristics of the LC-DFB laser have been measured as a function of ambient temperature up to 89 °C (Figure 63).

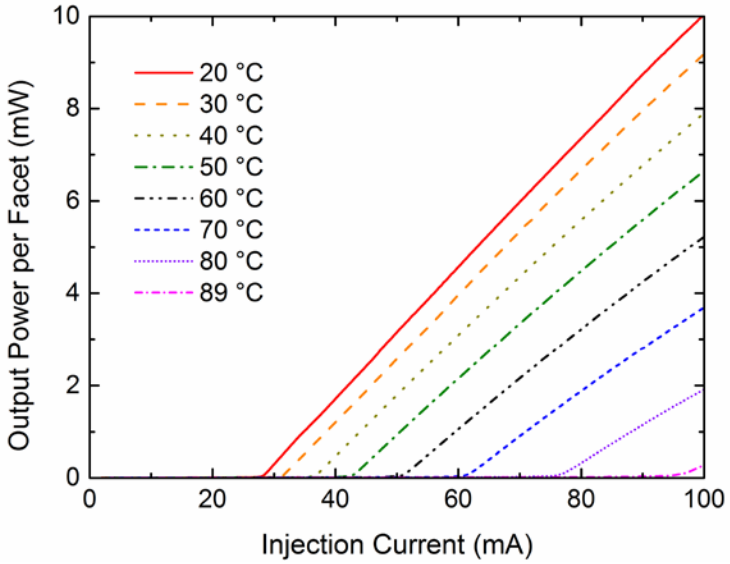

Figure 63. The temperature dependence of the light vs. current (LI) characteristics. Under 100 mA injection current, CW lasing can operate up to 89 °C.

Figure 64 shows the threshold slope efficiency at different temperatures. The laser is estimated to lase up to an ambient temperature T_{max} ~115 °C.

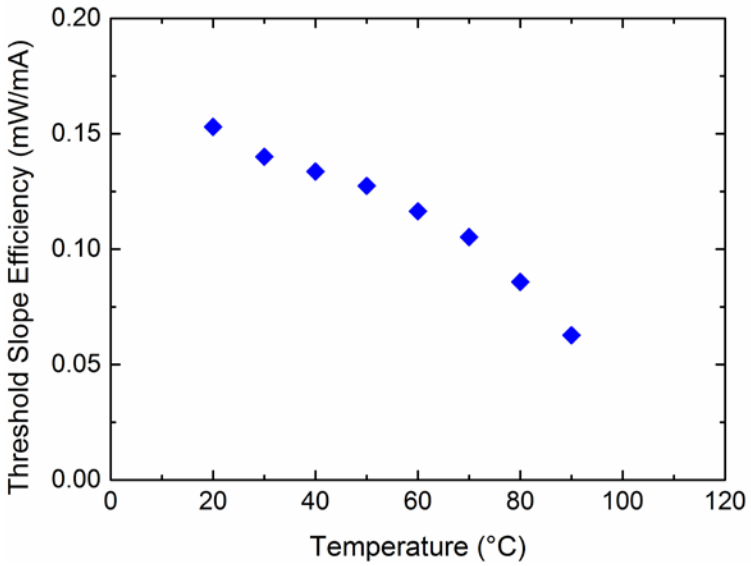

Figure 64. The threshold slope efficiency of the laser at different temperatures.

Using a thermal-electric cooler (TEC), the CW lasing wavelength is measured as a function of current and temperature (Figure 65). The wavelength shifts with current at a rate of $d\lambda/dI = 33$ pm/mA, which agrees with previously reports for DFB lasers (30 pm/mA) [26]. Also, the CW lasing wavelength shifts with the ambient temperature at a rate of $d\lambda/dT = 0.12$ nm/°C.

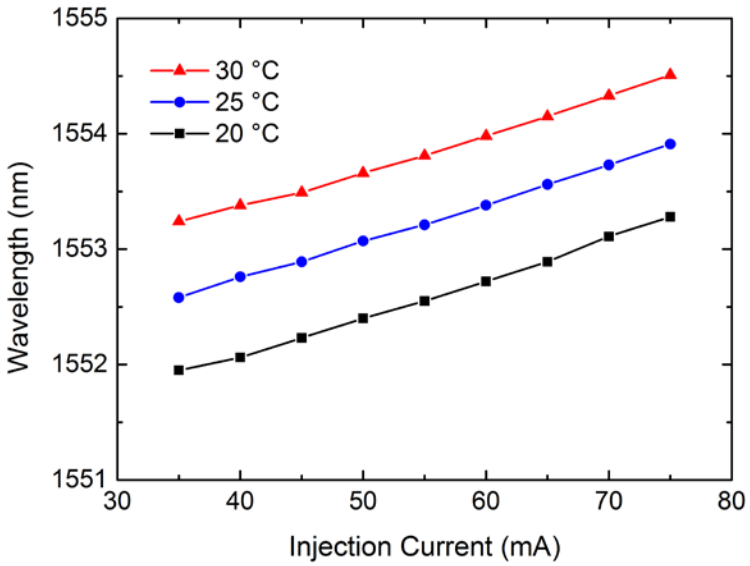

Figure 65. Lasing wavelength vs. injection current at different temperatures. The wavelength shift rate with injection current is 33 pm/mA. The wavelength shift rate with substrate temperature is 0.12 nm/°C.

To the best of our knowledge, we have achieved the first laterally coupled DFB laser with a first-order grating that is fabricated by interference lithography. DFB lasers with a 2.6 μm wide ridge including 300 nm wide lateral gratings on both sidewalls of the ridge have been fabricated. They achieved CW lasing over a wide temperature range (up to 89 °C under 100 mA), a threshold current density of 1.7 kA/cm^2, and single longitudinal mode operation with a SMSR of 37 dB. The method provides a practical approach to fabricate DFB lasers with strong first-order grating coupling, without using EBL and requiring no epitaxial regrowth. It offers a cost-effective and scalable path for high-volume DFB laser production for optical communication networks.

Chapter 5: Laterally-Coupled DFB Lasers and Laser Arrays with Equivalent Phase Shifts

As described in Chapter 2, index-coupled DFB lasers with uniform gratings are potentially prone to lase in uncontrollable wavelength modes. A quarter-wavelength phase shift region is necessary to pin the lasing mode exactly at the Bragg wavelength for controllable and stable single-mode lasing. In this chapter, an Equivalent Phase Shift approach is employed in laterally-coupled DFB lasers and laser arrays to ensure controllable single-mode lasing at the designated wavelengths.

Based on the principle described in Chapter 2, the sampled grating structure of the LC-DFB laser with EPS can be designed. A LC-DFB laser with EPS has been demonstrated [74]. The grating pitch, Λ, is set to be 254.8 nm. The sampling pitch, P, is designed to be 6.5 μm, and an EPS region of 3.25 μm is inserted at the center of the cavity (by extending one period to 9.75 μm), leading to a phase-matched resonant wavelength at λ_p = 1,571 nm. The Bragg wavelength will be at ~1,630 nm, which is sufficiently far away from the gain peak to eliminate the possibility of lasing at the Bragg wavelength. The EPS section with an additional length of 3.25 μm at the center of the cavity is designed to contain gratings, although the presence or absence of gratings in the EPS region will not affect the equivalent phase shift.

5.1 Fabrication of LC-DFB lasers with EPS

The wafer used, which contains an AlGaInAs/InP epi-structure designed for ridge-waveguide (RWG) lasers, was grown by Metal-Organic Vapor Phase Epitaxy (MOVPE)

in a single growth run on a (100) n-InP substrate. The gain peak occurs at 1,560 nm. The epi-layer structure contains an n-InP buffer layer, an n-InP cladding layer, an active region, a p-InP cladding layer and a contact layer. The active region consists of a Graded-Index (GRIN) separate confinement heterostructure (SCH), in which five AlGaInAs QWs are bounded between p-doped and n-doped GRIN layers, each of which contains an InAlAs carrier confinement layer.

In the fabrication process, a SiO_2 mask layer is first deposited on the surface of the epi-wafer by plasma-enhanced chemical vapor deposition (PECVD). Then a 20 nm thick Cr mask layer is evaporated onto the SiO_2 surface. The sampling pattern containing the specially designed EPS region is first transferred from the photomask to the Cr layer by conventional photolithography followed by a Cl_2/O_2 Inductively-Coupled Plasma (ICP) etch (Figure 66 (a)).

Tool	Oxford PlasmaLab System 100
Temperature	20 ºC
Pressure	40 mTorr
RF Power	50 mW
ICP Power	500 mW
Gas flow: O_2	20
Gas flow: Cl_2	80
Etch rate	>20 nm per 1 min
Notes:	Sample size not critical

Table 8. Chrome etch recipe by ICP using Cl_2 / O_2.

Regions in the SiO_2 layer covered by Cr define the non-grating regions, while the exposed SiO_2 will define the patterned grating regions. Optical interference lithography is used to pattern the gratings on top of the entire planar SiO_2/Cr surface. Since the Cr layer is much thinner than the photoresist layer (160 nm), the surface flatness variation (20 nm) has a negligible effect on the IL grating patterning. The grating quality in the photoresist is equally good with or without the Cr sampling layer. The IL gratings are then transferred to the SiO_2 mask by reactive-ion etching (RIE). The SiO_2 that is covered by Cr is totally protected, giving rise to the non-grating regions (Figure 66 (b)). Another photolithography step is then performed to pattern the 2.2 μm wide ridge waveguides (Figure 66 (c)). Cl_2/O_2 ICP and RIE etching processes are used to remove the Cr and the SiO_2 masks from regions where the ridge waveguide trenches will be etched (Figure 66 (d)). Before etching the ridge trenches, an oxygen RIE process [10] is used to remove a 200 nm wide region of photoresist from each edge of the ridge photoresist mask, thereby exposing a 200 nm wide region of sampled SiO_2 gratings along each sidewall of the ridge (Figure 66 (e)). The remaining photoresist now acts as a mask for etching the ridge in regions without gratings (W_r = 1.8 μm), while the narrow but exposed 200 nm wide sampled SiO2 gratings provide a mask for etching the deep lateral sampled grating (W_g = 200 nm) along both sidewalls as the trenches are etched. ICP etching with a $Cl_2/CH_4/H_2$ gas mixture is used for anisotropic etching of the III-V semiconductor materials (Figure 66 (f)). The grating aspect ratio is controlled to 0.5 for a maximized coupling efficiency.

The ridge and the gratings are both etched to a depth D = 2 μm, which is ~150 nm above the quantum well active region. Then the photoresist and Cr masks are removed,

using O_2 RIE for the photoresist, and a Buffered Oxide Etch (BOE) wet etch for the SiO_2, leaving the etched ridge and sampled gratings along both sidewalls of the ridge (Figure 66 (g)).

Following definition of the ridge waveguides and the sampled gratings, another SiO_2 layer is deposited by PECVD for electrical isolation, followed by opening of the contact window on top of each ridge (Figure 66 (h)). Ti-Pt-Au is used as the p-contact metal, and Ti-Au is used as the n-contact metal, deposited on the top and back side of the device, respectively (Figure 66 (i)). The contacts are annealed by a rapid thermal annealing (RTA) process at 450 ºC. After the wafer is cleaved into 900 µm long laser bars, a single-layer anti-reflection optical coating is deposited onto laser's output facet to suppress lasing in the Fabry-Perot (FP) modes.

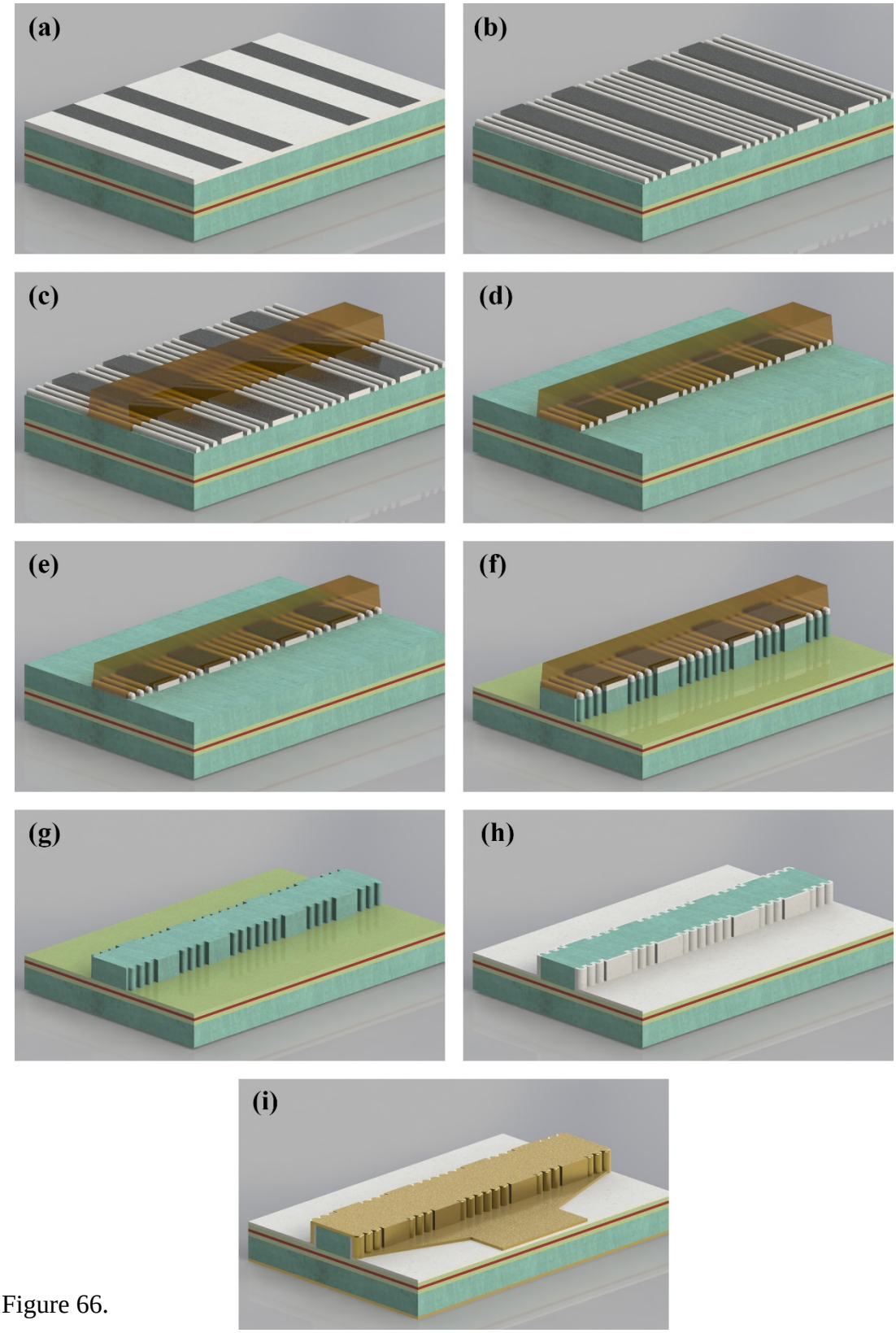

Figure 66.

Figure 66. Illustration of the fabrication process of the first-order lateral sampled gratings and LC-DFB lasers. (a) SiO_2 grating mask on the planar epi-wafer surface; (b) The ridge patterned on photoresist; (c) Removal of SiO_2 on open ridge trench area; (d) Oxygen RIE removal of photoresist to expose the SiO_2 grating mask on sidewalls of ridge; (e) ICP etch of ridge and sidewall gratings; (f) Photoresist and SiO_2 grating mask removal; (g) SiO_2 electric isolation and contact window opening; (h) Metallization.

Figure 67 shows the SEM image of an etched ridge with sampled gratings before etch mask removal. On this sample, a thicker Cr layer is intentionally deposited for good visibility.

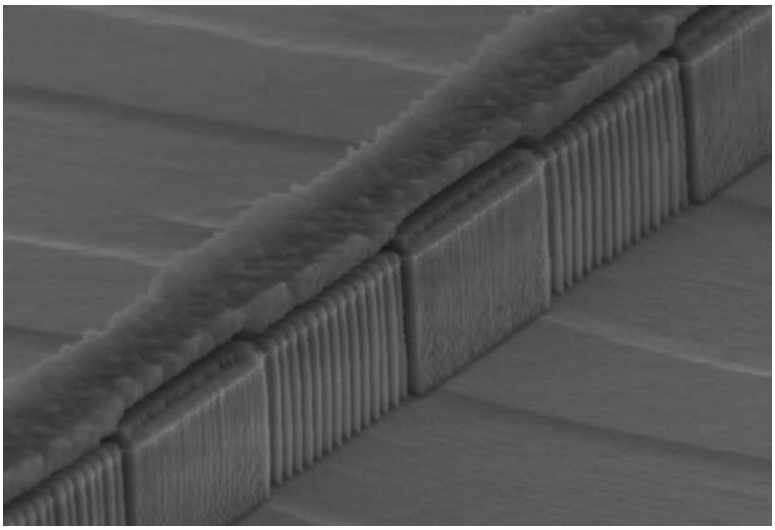

Figure 67. SEM image of etch ridge with sampled gratings before etch mask removal. Etch mask contains a SiO_2 layer, a Cr layer, an omnicoat adhesion layer, and a photoresist layer.

Figure 68 shows a scanning electron microscope (SEM) image of the ridge at the center of the laser cavity, where the quarter-wave EPS exists. It can be seen that the non-grating ridge sidewalls are very smooth, without any vestiges of gratings. It is due to the ultra-high etching selection ratio of SiO_2 to Cr. The sampling pattern is still visible on the bottom of the etched ridge trench. The pattern was partially transferred into the epi-wafer contact layer during etching and removal of the SiO_2 sampling mask, and propagates to the bottom of the ridge trench during ICP etching of the trench regions.

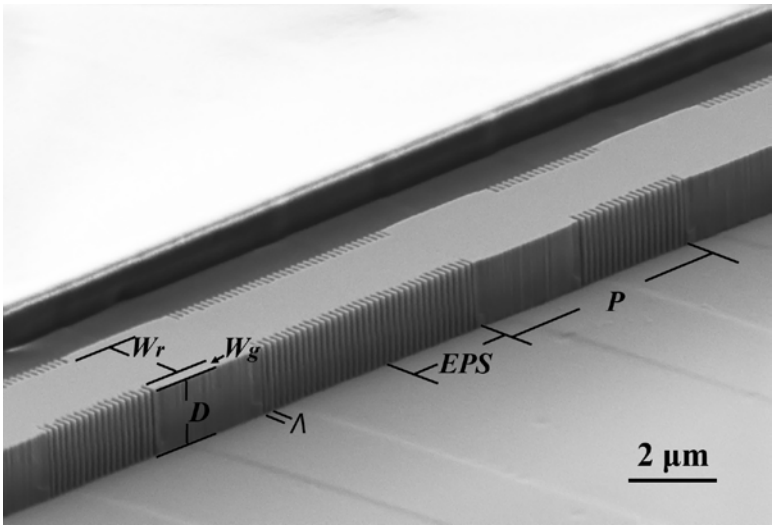

Figure 68. SEM image of the LC-DFB laser with the EPS region at the center of the laser cavity after etching the ridge trench.

The SEM images in Figure 69 (a) and Figure 69 (b) show the side-view and top-view of the LC-DFB laser with the EPS section after metallization.

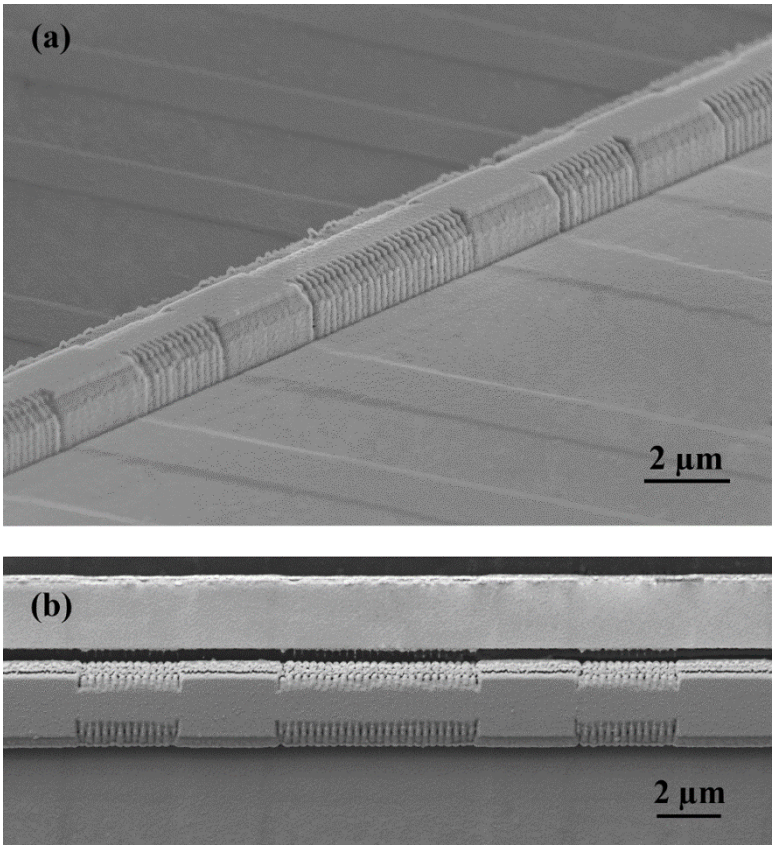

Figure 69. SEM image showing the side view (a) and top view (b) of a LC-DFB laser with an EPS region after metallization.

The coupling coefficient κ of such a device is strongly related to W_g, D, and W_r. The value of κ is very small when the etch is stopped at over 300 nm above the QWs, but increases dramatically as etching approaches the QWs. The value of κ drops rapidly as W_r becomes wider [14], and goes up as W_g is increased, but the rate of increase slows significantly when the grating width exceeds 500 nm. The estimated value of κL for this device is 1.03.

Figure 70 shows a photo to processed wafer (before cleaving into bars) of size ~ 1cm by 1cm.

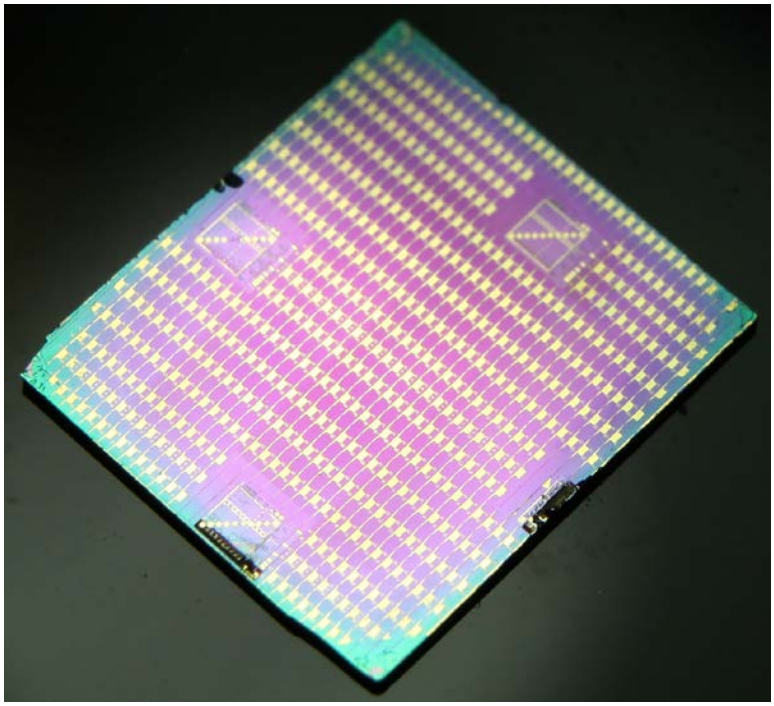

Figure 70. Finished sample before cleaving into bars.

5.2 PERFORMANCE OF LC DFB LASER WITH EPS

Continuous-wave (CW) lasing is achieved over a wide range of temperatures and injection currents. At room temperature (~25 ˚C), the threshold current is 27 mA, corresponding to a threshold current density of 1.5 kA / cm^2. The output power is 14 mW at a 100 mA injection current, and is 23.5 mW at a 200 mA injection current.

Figure 71 shows the lasing spectrum at 100 mA bias current under room temperature, CW operation. Single longitudinal mode lasing is obtained at 1,571.2 nm, with a side mode suppression ratio (SMSR) of 41.1 dB.

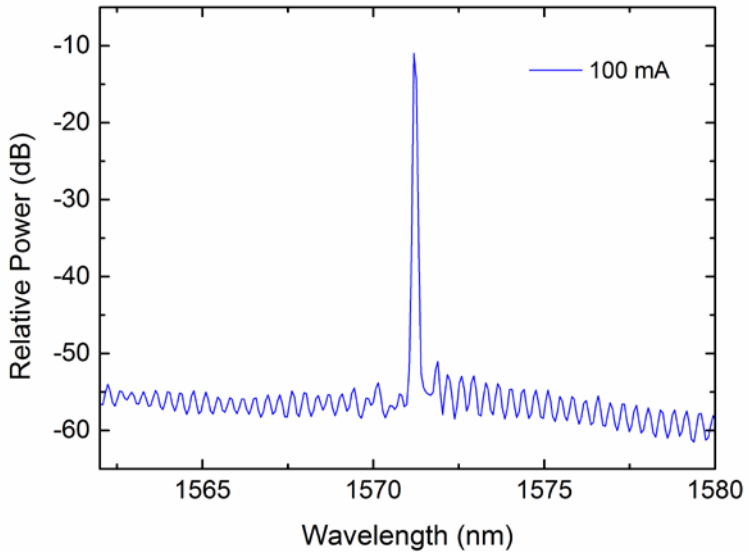

Figure 71. Lasing spectrum of the LC-DFB laser with a quarter-wave EPS region under an injection current of 100 mA. A SMSR of 41.1 dB is obtained.

The suppressed Bragg wavelength at ~1,630 nm can be seen clearly in an extended spectrum in.

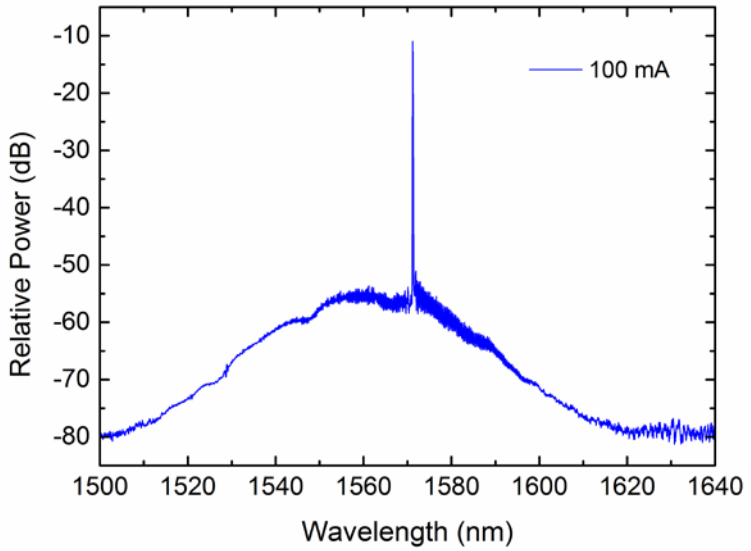

Figure 72. Extended spectrum of Figure 71.

For lasers with an EPS, the possibility of lasing at the Bragg wavelength needs to be examined. If the Bragg wavelength is too close to the gain peak, as the injection current increases, and the gain spectrum shifts towards longer wavelengths, lasing at the Bragg wavelength becomes competitive [26]. For the device design shown here, the Bragg wavelength does not lase at any temperature or injection current. The device exhibits a SMSR above 35 dB at up to 240 mA injection current.

The lasing mode shifts towards longer wavelengths with increasing bias current at the rate of ~ 10 pm/mA, under temperature control by a Thermoelectric Cooler (TEC). As the injection current is increased, even with TEC, the junction temperature still rises, causing the refractive index to increase [75]. However, for phase-shifted lasers the optical field intensity peaks at the phase shift region, where the higher carrier density under high injection current causes the effective refractive index to decrease [76], which partially

reduces the temperature-induced red-shift, although the overall shift is still towards a longer wavelength.

The light-current-voltage (LIV) characteristics of the LC-DFB laser under different ambient temperatures has been measured and are shown in Figure 73.

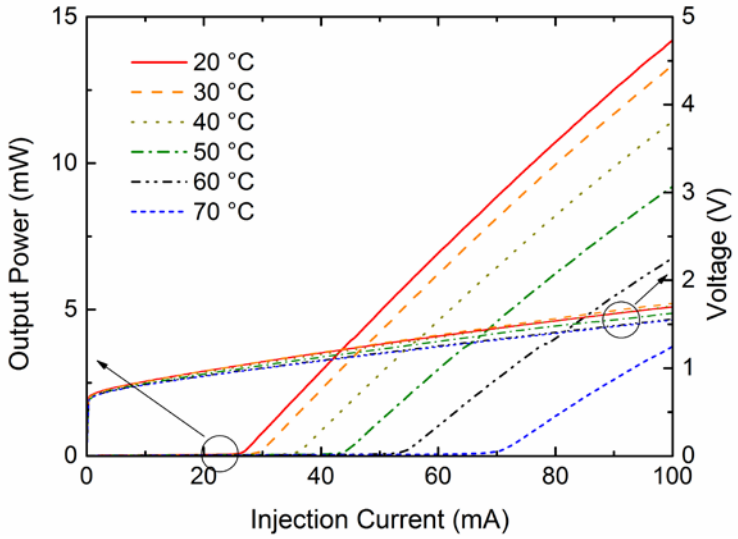

Figure 73. LIV curves of the LC-DFB laser with EPS at different ambient temperatures.

In the same experiment, another laser is designed and fabricated. The sampling period *P* is designed to be 4.0 μm with an EPS region of 2.0 μm in the center of the cavity. The measured lasing wavelength is at 1,535.6 nm, which is very close to the designed wavelength of ~ 1,536 nm, and represents a wavelength blue-shift of 35 nm from the previous DFB laser. The lasing spectrum at 40 mA is shown in Figure 74.

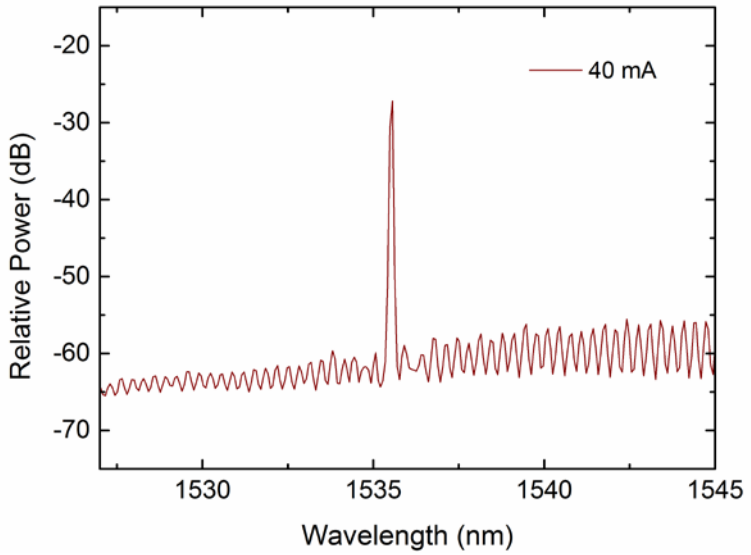

Figure 74. Lasing spectrum of another LC-DFB laser with another sampling period which is designed for 1536 nm operation.

In conclusion, LC-DFB lasers with equivalent phase shift have been demonstrated. The lasers operate in a single longitudinal mode over a very wide range of injection currents. A SMSR of 41.1 dB is achieved under a 100 mA DC bias. At room temperature (~25 ˚C), and under 100/200 mA bias current, a 14.0/23.5 mW optical output power is obtained. This method provides a scalable and low-cost approach to fabricating quarter-wave phase-shifted DFB lasers using e-beam-free and regrowth-free processes, which may be useful for the fabrication of DFB lasers with stable and precise wavelengths, as single devices or as arrays in photonic integrated circuits both in academic research and for industrial production.

5.3 Performance of LC EPS DFB Laser arrays

Based on the previous work on single lasers, a LC-DFB laser array with equivalent phase shift has been demonstrated.

The cavity length is designed to be 600 μm. Grating pitch is designed to be 255.5 nm, with a Bragg wavelength located at 1,628.27 nm. The front facet is coated with a single layer of SiO_2 for low reflection. The contiguous laser array has 5 wavelength channels with sampling periods varying from 4.4 μm to 6.64 μm. The lasing wavelength ranges from 1545.57 nm to 1574.76 nm under 80 mA injection current, with an average wavelength spacing of 7.3 nm. Lasing spectra of the 5-wavelength LC DFB laser array with equivalent phase shift is shown in Figure 75. The average SMSR is 37.34 dB with a minimum of 32.33 dB for Channel 4.

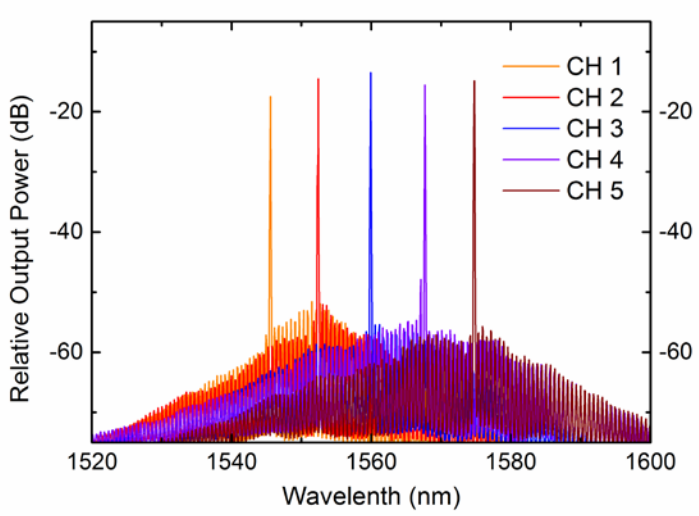

Figure 75. Lasing spectrum of a 5-wavelength laterally-coupled DFB laser array with equivalent phase shifts under an injection current of 80 mA.

Figure 76 shows the L-I characteristics of the laser array. The thresholds range from 24 mA to 29 mA. The output power under 100 mA bias current ranges from 11.4 mW to 14.1 mW.

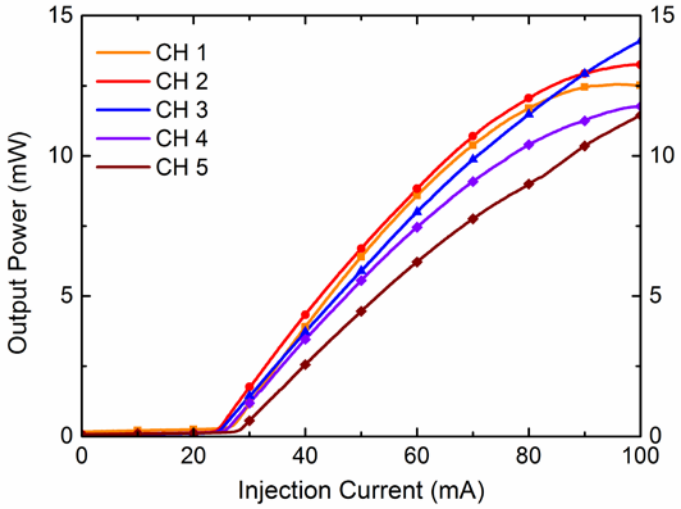

Figure 76. LI characteristics of all 5 channels in the DFB laser array at room temperature.

The non-uniformity of the L-I curve in Figure 76 is caused by several reasons. Different wavelength channels share the same gain spectrum, but have different modal gain according to the wavelength location relative to the gain spectrum. Also, variations in the fabrication process(such as thickness of photoresist, position of laser related to sample edge and corner, *etc*.) will affect the yield and performance of the laser array, causing some non-uniformity in device characteristics. Yield problem can be improved when whole wafers are processed.

The experimental lasing wavelengths compared to the design and fitted wavelengths are shown in Figure 77. As discussed in Chapter 3, the deviation in slope is

mostly from the estimation error in index dispersion. When designing the laser array, 1550 nm is used as the design reference wavelength. So to fit the wavelengths, the first step is to estimate error in grating pitch, can be roughly obtained from channel 2 (most close to 1550 nm). Then, by adjusting refractive index dispersion, a fitted wavelength can be obtained. Here, the fitted wavelengths have an adjusted grating pitch to 255 nm (original design is 255.5 nm) and a adjusted dispersion coefficient to 1.5×10^{-4} / nm (original design is 4×10^{-4} / nm). The fitted wavelengths agree well with experimental wavelengths with a maximum wavelength deviation of 0.5 nm at channel 4. Fitted wavelengths looks almost overlap with experimental results is because the wavelength spacing is large (6.4 nm). So a deviation of 0.5 nm is not significant.

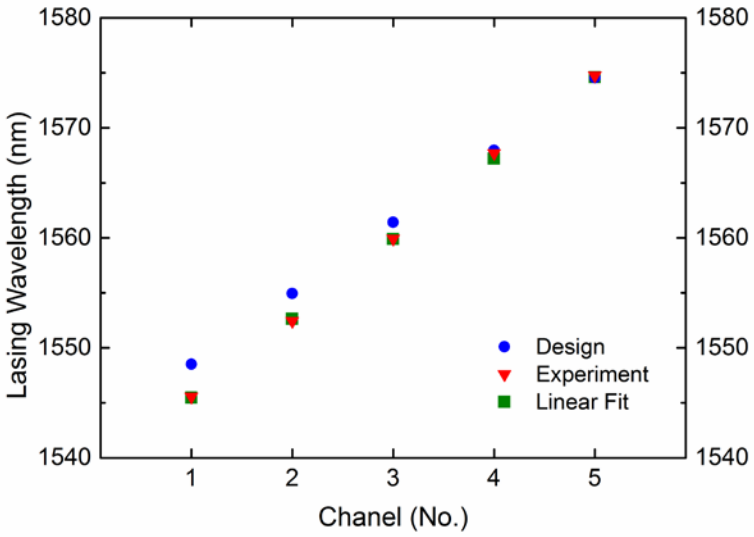

Figure 77. Experimental lasing wavelength of the laser array compared to design.

To achieve a better laser array, several aspects need to be considered.

A 800-GHz channel spacing at 1550 nm corresponds to a wavelength difference of 6.4 nm. For an 8-wavelength laser array, the total wavelength span is ~ 45 nm. If the quantum wells are not specifically designed for this wavelength band, each of the 8 channels will experience different optical gain, which leads to non-uniform lasing performance.

Optimized facet coatings are very important for DFB lasers to achieve good performance. Usually an anti-reflection (AR) coating with a reflectivity of $< 1\times10^{-4}$ is needed to ensure the elimination of FP ripples in the optical gain spectrum. A high quality AR coating with low reflectivity over a 45 nm-wide band requires multi-layer dielectric coatings with accurate thickness and index control, which is not easily achievable using our available coating tools. The low-reflection coating used in the LC-DFB laser array fabrication consists of a single layer of SiO_2, which has at best a reflectance of 4%, which is far from being optimum.

Also, the size of samples processed in this experiment are always smaller than 1 cm × 1 cm, for which the non-uniformity problems in fabrication are severe.

Chapter 6: Buried Heterostructure DFB Lasers and Laser Arrays with Equivalent Phase Shifts

6.1 Introduction to Buried Heterostructure Lasers

Buried Heterostructure (BH) lasers have many advantages compared to RWG and LC lasers. BH lasers can be fabricated with a narrower active region width, which reduces both driving current and power consumption [29, 77, 78]. Also, the BH laser usually has a lower threshold current, a near-circular and stable output beam, and lower thermal resistance [79-81]. Also, BH lasers have better current confinement and optical confinement via index guiding compared to the weakly index-guided RWG lasers [82].

Recently, a lot of research has focused on the fabrication of InP/AlInGaAs BH lasers. But unlike the RWG lasers, BH lasers always need to etch through the QWs, so the aluminum-containing materials tend to have an aluminum oxidation problem [83], which also makes regrowth difficult. Therefore, BH lasers are more likely to be made using the InP/InGaAsP material system rather than the InAlGaAs/InP material system.

To achieve single transverse mode operation, BH lasers should have an active region width less than 2 μm [84], which is usually narrower than the ridge width of RWG lasers. RWG lasers use etched trenches with dielectric isolation to confine the optical field, which have a very high index contrast (3.2 : 1.5), and therefore good optical confinement. In BH lasers, the index contrast is between the quaternary material (InGaAsP) and InP, which is much smaller (3.4 : 3.2) than the RWG lasers. So a narrower active region is needed to confine the optical modes. A narrower active region also results in a smaller

active area (with the same device length), so the threshold current is always lower compared to the RWG lasers.

A unique aspect of BH Lasers is that the BH structure contains all-semiconductor materials. Electrical isolation and effective current confinement are needed for currents to be efficiently injected into the active region. There are two main types of electrical isolation methods: (1) by using a p-n-p-n type of blocking layer [84], or by using an Fe-doped, semi-insulating layer. When a forward voltage is applied to the p-n-p-n materials, the junction between the first n layer and the second p layer is reverse biased, forming a current blocking junction. The Fe acts as a deep acceptor in InP that compensates the low n-type doping, thus rendering semi-insulating while pinning the Fermi level near the center of the band gap (~0.65 eV below the conduction band edge). Usually, a thick Fe-doped InP layer has lower parasitic capacitance, which is more suitable for high-speed modulation. In the work presented in this thesis, a p-n-p-n type current confinement layer is regrown.

In this chapter, BH-DFB laser arrays with EPS are demonstrated.

6.2 Design and Fabrication of Buried Heterostructure DFB laser arrays

In pursuing better lasing performance, we also designed and fabricated BH-DFB laser arrays, which operate at the 1.31 μm wavelength region. A 350 μm thick (100) InP substrate is used, with sulfur-doping of 5×10^{18} / cm^3. Then a 200 nm n-InP buffer with 10^{18} / cm^3 doping was grown. An active region is embedded between the upper and lower cladding layers, which consist of undoped 1.1Q InGaAsP materials. The active region contains 8 quantum wells, each consisting of a 6 nm thick 1.4Q InGaAsP gain layer with 1% compressive strain, bounded between barrier layers consisting of 10 nm thick 1.1Q

InGaAsP with 0.3% tensile strain for compensation. Above the upper InGaAsP cladding layer, an p-InP spacer was grown, followed by a grating layer. The first growth stops here.

A wafer mapping of the photoluminescence (PL) spectra characteristics (center wavelength, spectral FWHM, and peak intensity) of the as-grown epi-wafer is shown in Figure 78:

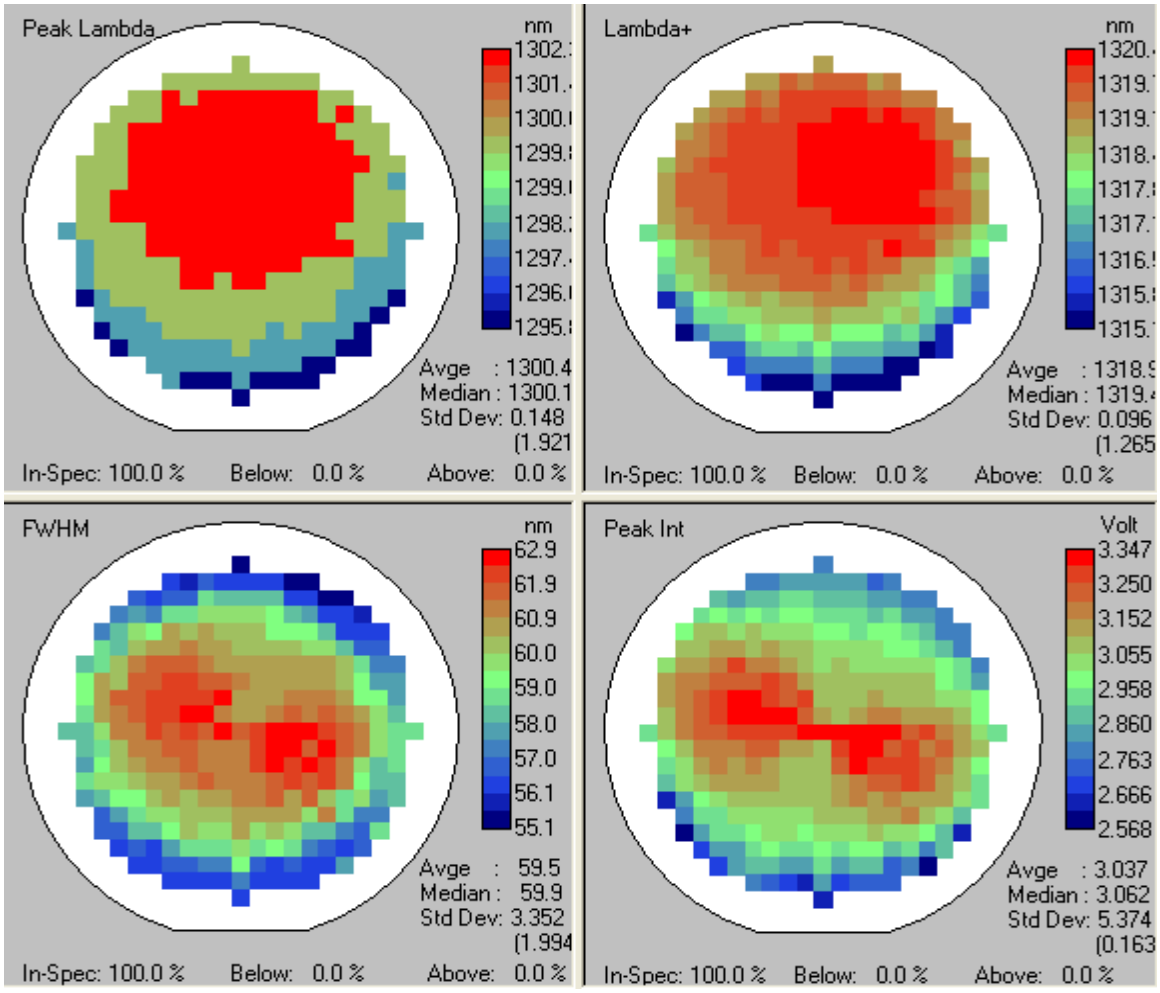

Figure 78. PL mapping of 1.3 µm InP/InGaAsP wafer for BH lasers.

The sampled grating was first patterned on the planar top surface of the epi-wafer, and then transferred and etched into the grating layer by wet chemical etching. There are basically two ways to wet etch the InGaAsP gratings. One uses a non-selective etch, consisting of bromine - methanol (Br_2 : CH_3OH), which gives a good sinusoidal-shaped grating with smooth side walls for regrowth. For selective wet etching, a sulfuric acid - hydrogen peroxide - deionized water (H_2SO_4 : H_2O_2 : H_2O) solution can be used, which selectively etches the InGaAsP materials against InP. In this work, the non-selective solution is used with pre-calibration.

After grating etch, the uniform gratings are patterned into sampled gratings with designed pitches and phase shifts. In the sampled periods, the high index materials (InGaAsP) were etched away during the sampling patterning (Figure 79), which is different from the laterally-coupled lasers.

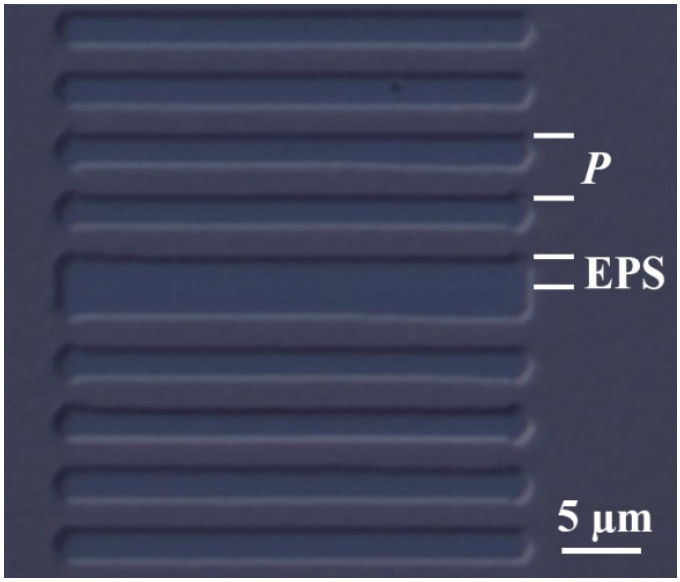

Figure 79. Microscope image of the sampled grating with an EPS region inserted at the center of the cavity for buried heterostructure DFB lasers.

A layer of SiO_2 was then grown on top of the wafer, which is later patterned into a 1.3 µmwide ridge stripe oriented perpendicular to the grating direction. Wet etching with a bromine – methanol solution is performed to etch away the III-V material on both sides of the ridge.

Without removing the SiO_2 stripes, the wafer was sent back to the MOCVD chamber for the regrowth of the current blocking layers. In this regrowth step, a layer of n-doped InP, doping to 1×10^{18} / cm^3, and a layer of p-doped InP, doping to 1×10^{18} / cm^3, were selectively regrown around the oxide-coated stripes. MOCVD growth is a surface pyrolysis and chemical nucleation process. Where the SiO_2 layer exists, the III-V atoms cannot nucleate on the SiO_2 surface and grow, so the reverse p-n junction does not exist above the active regions.

After the first regrowth, the SiO_2 stripes are selectively removed by wet etching. Then a third growth (or second regrowth) is performed non-selectively on the entire wafer, including a 1.7 μm thick p-doped InP cladding layer and a 200 nm p-doped InGaAs contact layer.

Figure 80 shows an enhanced SEM image of the cross section of the BH-DFB lasers after the third growth.

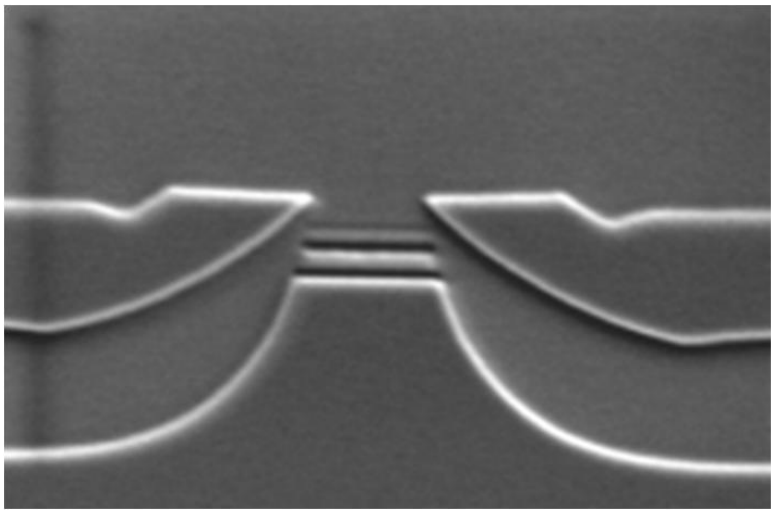

Figure 80. Cross section SEM image of BH-DFB lasers after third growth.

Two isolation trenches were patterned and etched along the active region to reduce the parasitic capacitance of the devices. A SiO_2 layer is then deposited globally for passivation, followed by opening of the contact windows above the active regions.

The back side of the InP substrate is thinned down to ~100 μm to reduce thermal resistance. Then Ti/Pt/Au metal layers are e-beam evaporated on the top epi-side for p-

contact formation, while AuGe/Ni/Au metal layers are e-beam deposited on the back side for the n-contact.

6.3 BH-DFB LASER ARRAY PERFORMANCE

Monolithically integrated multi-wavelength DFB laser arrays with a buried heterostructure have been demonstrated [85]. The laser cavity length is cleaved to 300 µm, with anti-reflection (AR) and high-reflection (HR) coatings deposited on the front and back facets, respectively. The lasing and electrical characteristics of a monolithic six-element DFB laser array, shown in Figure 81, indicate fairly uniform performance characteristics. The threshold current ranged from 7 to 9 mA, the differential slope efficiency (S.E.) near threshold ranged from 0.50 to 0.53 mW / mA and the output power at 80 mA injection current bias is 28 to 35 mW.

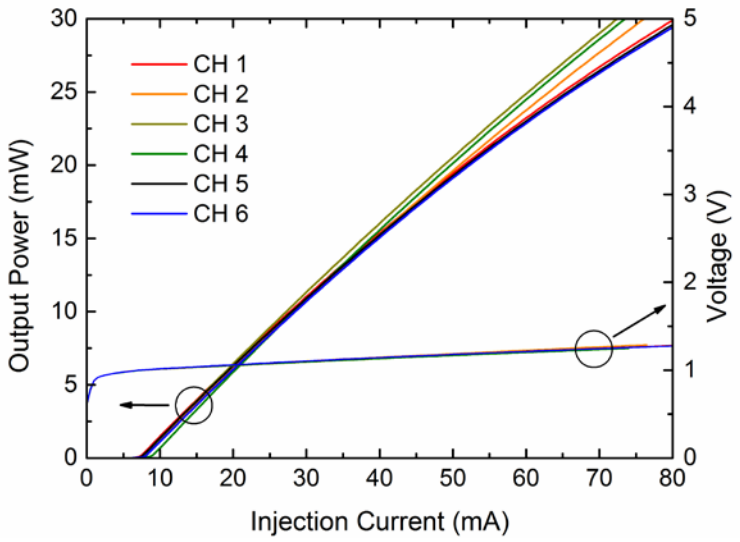

Figure 81. LIV characteristics of a six-wavelength BH laser array fabricated with sampled gratings and equivalent phase shifts. Cavity length is 300 µm.

All 6 channels, with a designed wavelength spacing of 4.8 nm (800 GHz / channel), lased in a single longitudinal mode. The maximum deviation from the design wavelength is 0.6 nm. No lasing was observed at the Bragg wavelength (at ~1380 nm) at any injection current.

Figure 82 shows the lasing spectra of the DFB laser array at an injection current of 60 mA. The average SMSR is 45.3 dB, with a minimum of 40.3 dB.

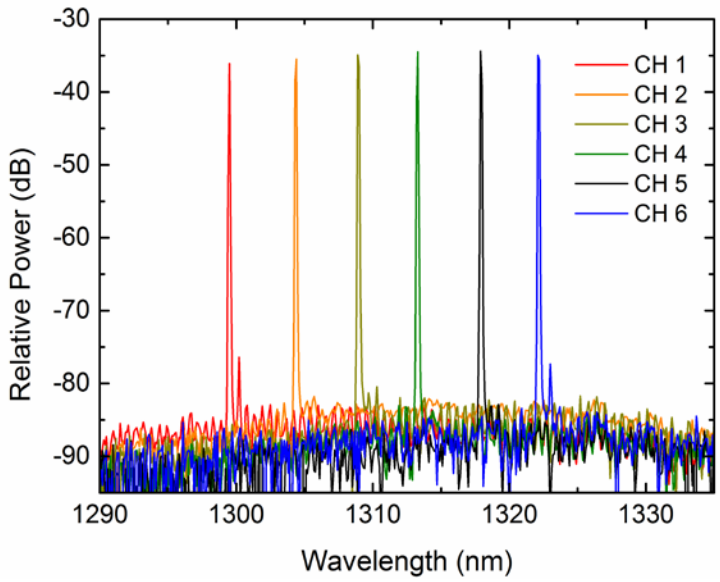

Figure 82. Spectrum of the 6-wavelength BH-DFB laser array.

6.4 BH-DFB LASER ARRAY WITH IMPROVED PERFORMANCE

Further improvements have been carried out for better results. As stated in Chapter 2, DFB lasers with equivalent phase shift inherently have a lower coupling efficiency due to the employment of sampled gratings and a non-Bragg wavelength channel. Therefore, lasers with EPS usually have longer cavities compared to standard uniform grating DFB

lasers. For lasers with the BH structure, there are usually three ways to improve the coupling efficiency.

The first way is to place the grating layer closer to the quantum-well region, which leads to a bigger optical overlap between the gratings and the optical field. However, there's always a limit of how close the grating layer can be. For better laser performance, a separate confinement heterostructure is usually needed. An upper GRIN layer 50 nm thick is needed for optical confinement, and a 50 nm spacer is needed for the electron confinement layer In addition, a 10-20 nm thick InP etch-stop layer is needed under the InGaAsP grating layers. So there is very tight lower limit to placing the grating layer closer to the quantum-well region.

The second way is to have a grating with a higher refractive index contrast. As mentioned before, in the grating layer the lower index is always InP, but the higher index layer can be made of a higher Q layer with a longer wavelength and higher index. However, as the Q value gets closer to the lasing wavelength, the Q layer will eventually become absorbing, and thus impair laser performance. The highest Q layer that can be safely used as a grating layer is 1.25Q for 1.3 μm lasers, and 1.45Q layer for 1.55 μm lasers.

The third way is to use a thicker grating layer, which essentially enhances the optical overlap. The maximum thickness can be used in making a BH laser is limited by two factors: wet etch capability and regrowth quality. When regrowth over grating is needed, dry etching is always avoided due to the resulting surface damage and roughness. Also, the surface topology is an important factor to consider in regrowth. Deep gratings

with angled facets give rise to competing nucleation along different crystal facets, which creates dislocations and are difficult to planarize.

First-order Bragg gratings usually have a grating pitch around 200 nm to 250 nm, so the opening is 100 nm to 125 nm. When wet etching is used, it is very difficult to etch to a deep distance with high aspect ratio. As the etch depth increases, the material in the upper layers will eventually be etched away, then the total grating thickness will stop increasing.

In the new design, a 60 nm thick 1.25Q InGaAsP is used to achieve a κL value of 1.64, which is for an industrial standard 250 μm long cavity. The effective refractive index is calculated to be 3.2477 with a dispersion coefficient of 3.00×10^{-4} / nm. The value of κ is calculated to be 206.592 / cm. An 8-wavelength laser array is designed with a spacing of 800 GHz / channel (4.6 nm / channel), and is centered at 1310 nm, the location of the optical gain peak. The sampling pitch varies from 3.275 μm to 5.836 μm. Figure 89 shows the SEM image of sampled gratings for BH-DFB lasers. In a sampling period, InGaAsP material in regions without grating has been etched away. The grating pitch is 212.2 nm, resulting in a Bragg wavelength of 1370.61 nm which is far away from gain and is not possible to lase. The HR / AR facets coatings are deposited, with HR = 90% and AR < 0.5%.

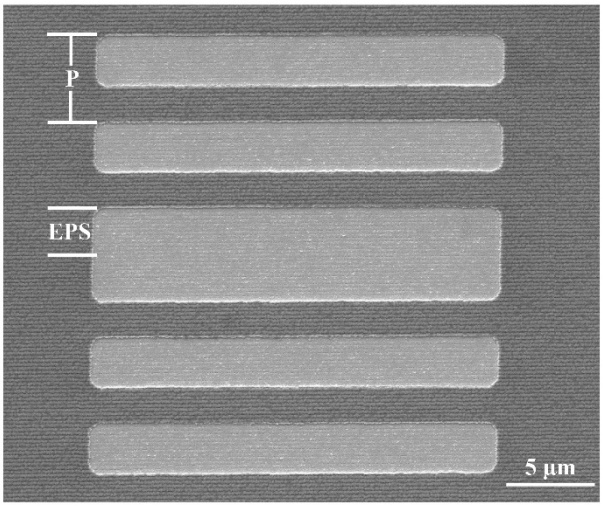

Figure 83. SEM image of sampled gratings on a planar surface for BH-DFB laser fabrication.

Figure 84 shows a finished BH-DFB laser with EPS close to the facet region in an angled view. The device is stained with H_2SO_4 : H_2O_2 : H_2O at 3:1:1 to differentiate different layers. The two trenches on both side of the active region is non-selectively wet etched (isotropically etched).

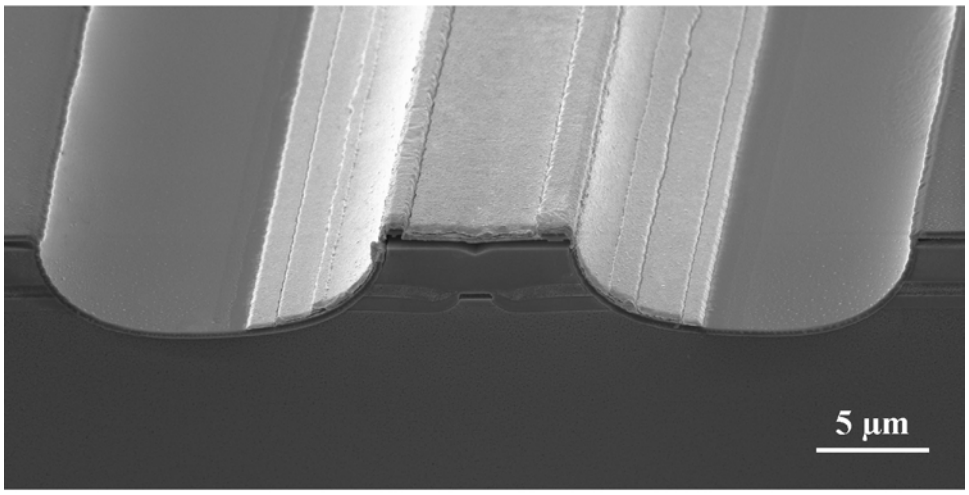

Figure 84. SEM images of BH-DFB laser at the output facet with isotropically etched trenches.

Figure 85 show the SEM image of the active region of BH-DFB lasers with EPS.

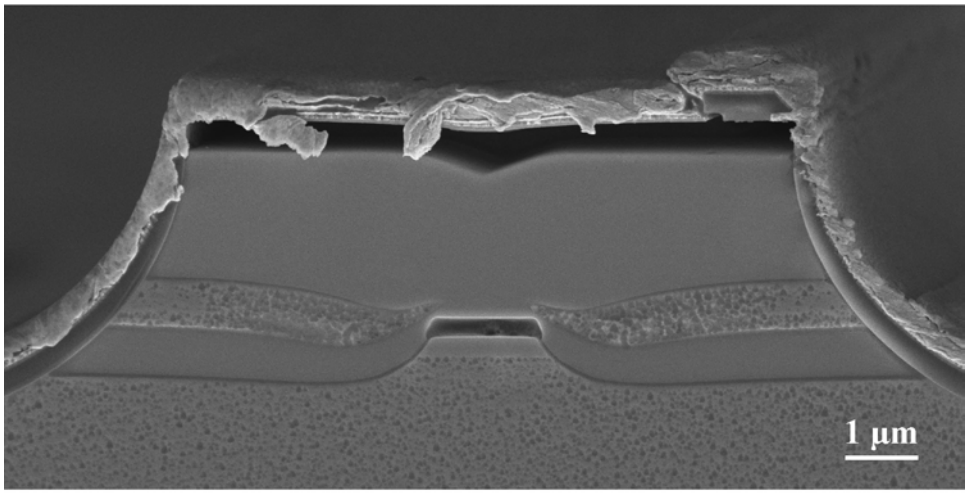

Figure 85. SEM image of the active region of BH-DFB lasers with EPS. Device is stained by H_2SO_4 : H_2O_2 : H_2O at 3:1:1, which etches InGaAsP material and causes roughness to n-doped InP layers.

The monolithically integrated 8-wavelength BH-DFB laser array demonstrates good lasing performance under a wide range of temperatures and injection currents. Figure 86 shows the continuous-wave (CW) lasing spectra of the laser array under 60 mA injection current, and tested at room temperature (~22 °C). The average CW output power and SMSR are 22.5 mW and 47.4 dB, respectively.

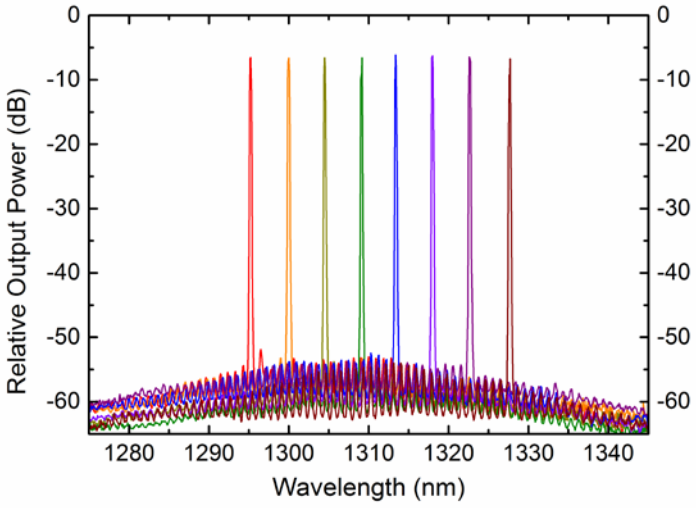

Figure 86. Lasing spectra of the 8-wavelength BH-DFB laser array with equivalent phase shifts under 60 mA injection current at room temperature. The average output power is 22.5 mW. An average SMSR of 47.4 dB is achieved. The maximum wavelength deviation from design is 0.4 nm, < 9% of the wavelength spacing.

All 8 channels exhibit relatively uniform light-current (L-I) characteristics, as shown in Figure 87. The threshold currents are between 6 to 9 mA. The output powers at 100 mA injection current are between 28.8 mW to 34.2 mW. The maximum wavelength

deviation observed is 0.4 nm, between Channels 7 and 8, which is < 9% of the 800 GHz design.

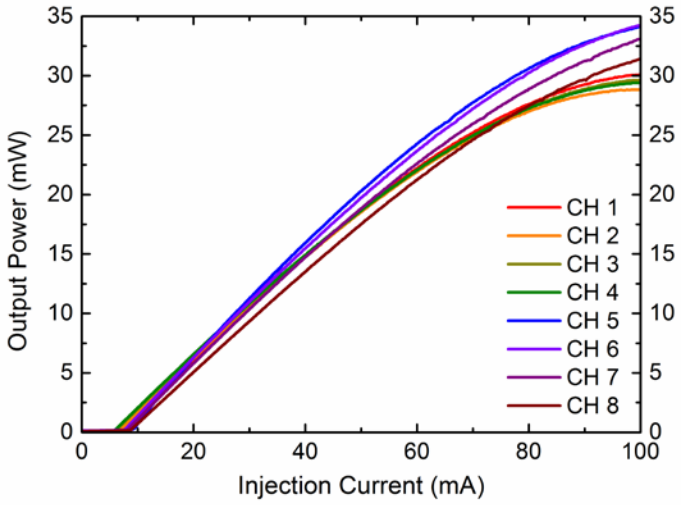

Figure 87. LI curves of all 8 channels of the laser array - at room temperature. Thresholds are within 6 to 9 mA. Output powers are from 28.8 mW to 34.2 mW under 100 mA injection current. All 8 channels exhibit relatively uniform light-current (LI) characteristics.

The laser array performance has been tested under different injection currents at room temperature. Figure 88 and Figure 89 show the lasing wavelengths and SMSRs of all 8 channels at bias currents of 20, 40, 60, 80 and 100 mA (at room temperature). Stable single mode lasing operation is achieved without mode hopping under all tested injection currents. The wavelength shift rate with injection current is ~33 pm/mA. Every channel within the array achieved a SMSR above 45 dB under bias currents between 60 mA to 100 mA.

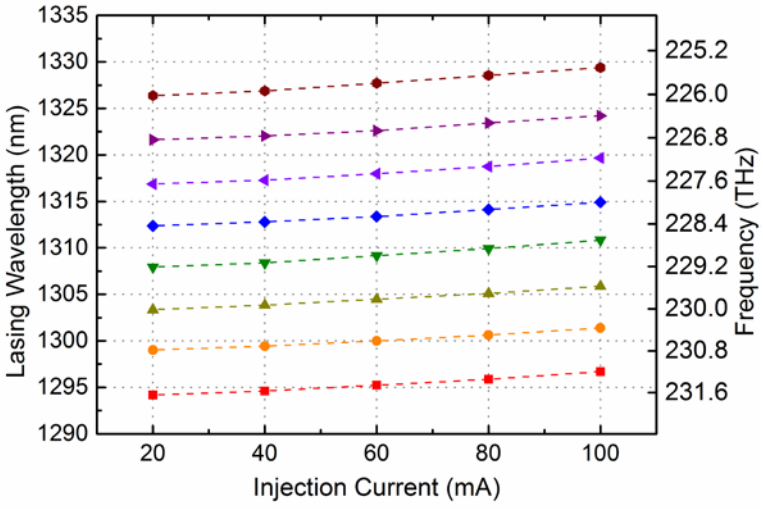

Figure 88. Lasing wavelength *vs.* injection current of all 8 channels at 22 °C. The wavelength shift rate with injection current is ~33 pm/mA (without TEC).

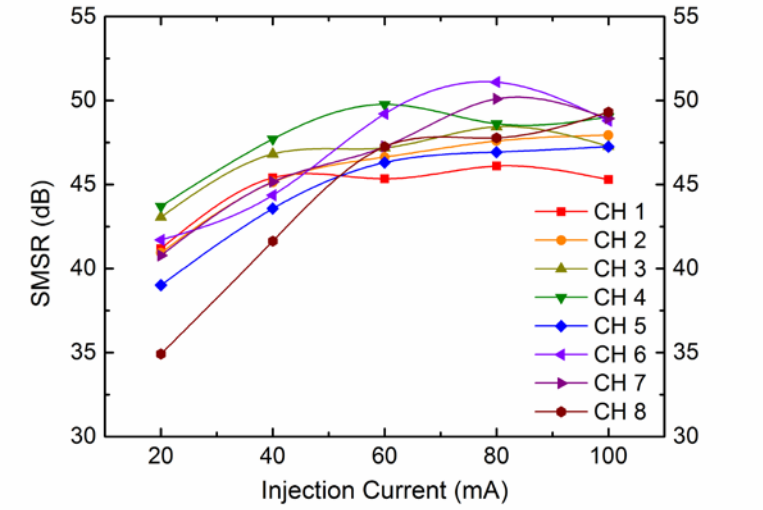

Figure 89. SMSR *vs.* injection current of all 8 channels at 22 °C. Every channel within the array achieved a SMSR above 45 dB under bias currents between 60 mA to 100 mA.

The laser array performance at different temperatures has also been examined under a fixed 60 mA injection current. A thermoelectric Cooler (TEC) is used to control the

substrate temperature of the device. Fig. 85 shows the temperature dependence of the lasing wavelength of all 8 laser channels. The wavelength shifting rate with temperature is ~ 0.11 nm / °C.

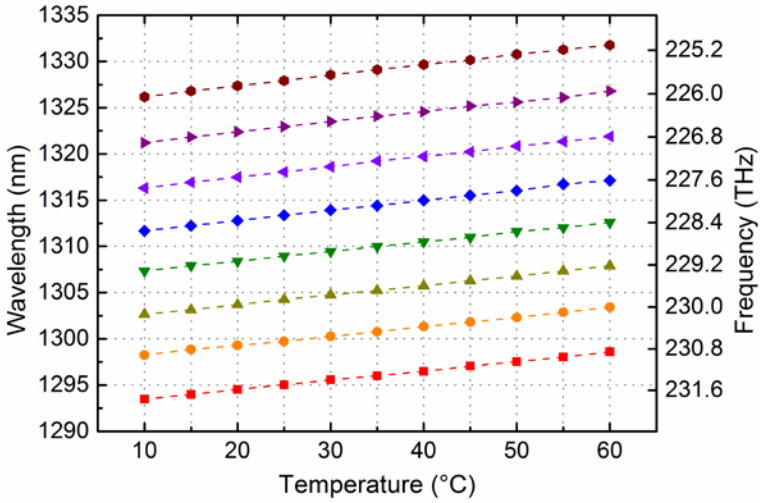

Figure 90. Lasing wavelength *vs*. temperature of all 8 channels at 60 mA injection current.

Figure 86 shows the SMSRs of the laser array at different temperatures. All channels exhibit a SMSR above 35 dB at temperatures ranging from 10 °C to 60 °C.

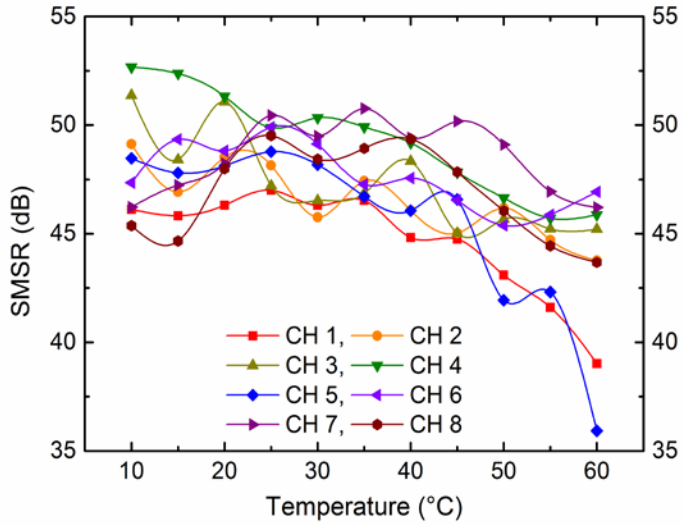

Figure 91. SMSRs *vs.* temperature of all 8 channels at 60 mA injection current.

Figure 92 shows the output power of all 8 channels at 60 mA under different temperatures. The minimum output power is >7.4 mW.

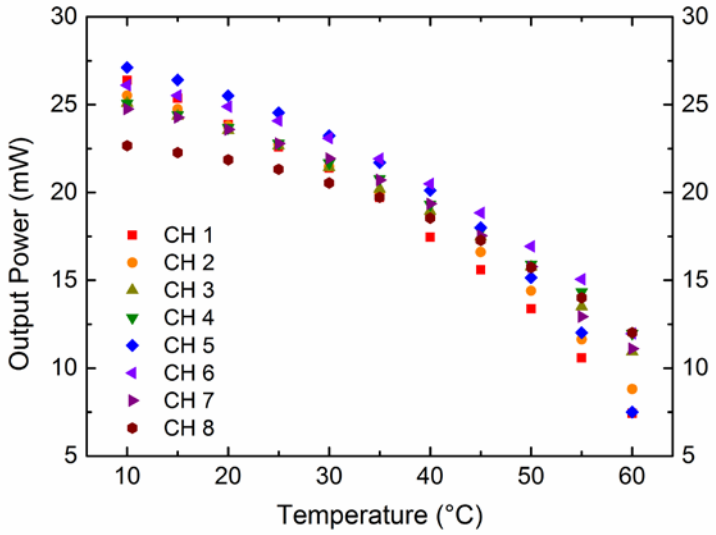

Figure 92. Output power of all 8 channels at 60 mA under different temperature.

Figure 93 plots threshold currents change with temperature from 10 ºC to 60 ºC of all 8 channels.

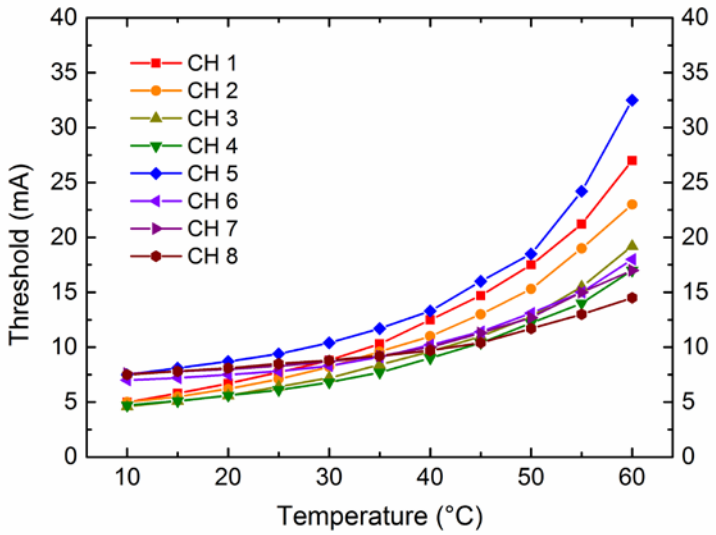

Figure 93. Threshold currents change with temperature from 10 ºC to 60 ºC of all 8 channels.

By turning on different lasers of the array sequentially, the lasing wavelength can be thermally tuned over a very wide wavelength range without mode-hopping, with a minimum output power of 7.4 mW over the whole tuning range. This form of wavelength tuning can be very useful in the WDM multiplexing and de-multiplexing grid, and provides a practical and relatively simple method in the design and fabrication of widely tunable DFB lasers.

By selecting appropriate temperature and channel, continuous tuning can be realized (Figure 94). Under the same injection current of 60 mA., this laser array can be tuned from 231.9 THz to 225 THz with 100 GHz spacing (1292.77 nm to 1332.41 nm),

covering 70 channels (39.64 nm). The minimum output power is 9.8 mW which occurs at Channel 8 under 65.1 ºC.

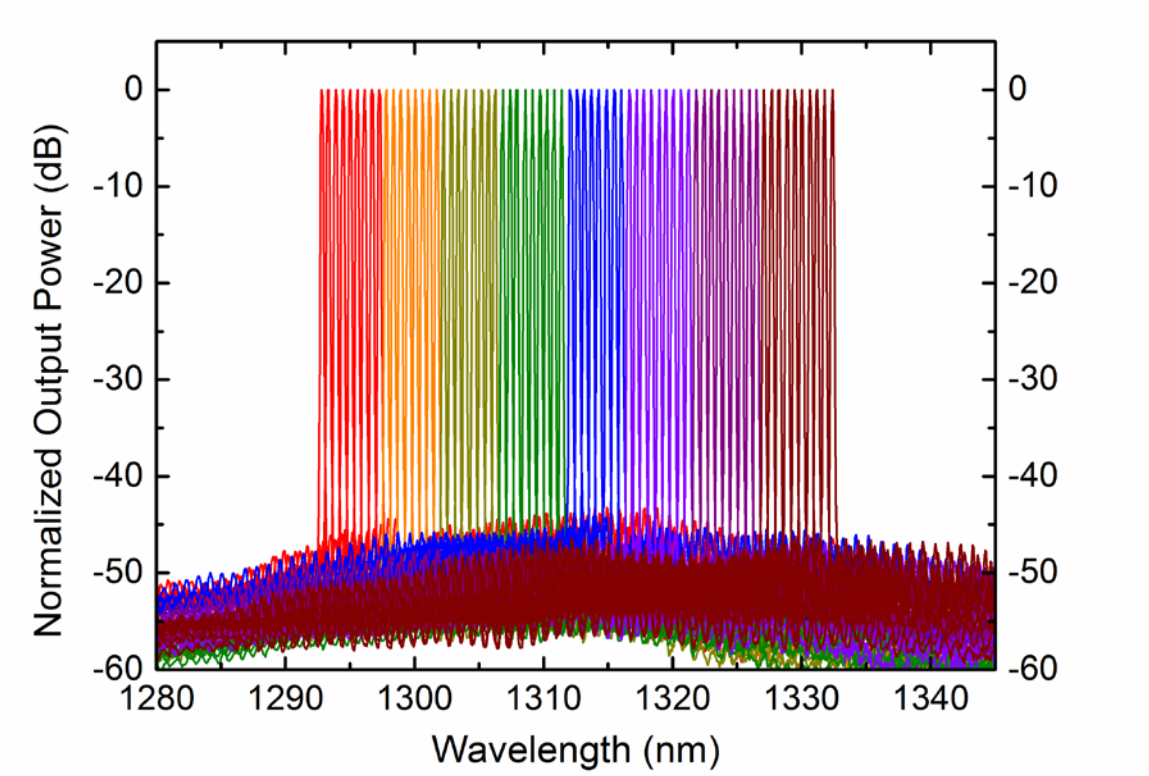

Figure 94. Wavelength continuous tuning from 231.9 THz to 225 THz with 100 GHz spacing (1292.77 nm to 1332.41 nm), covering 70 channels (39.64 nm).

The detailed tuning temperature and channel switch frequency is shown in Figure 95. The temperature tuning range is from 2.8 ºC (Channel 1, 231.9 THz) to 65.1 ºC (Channel 8, 225 THz).

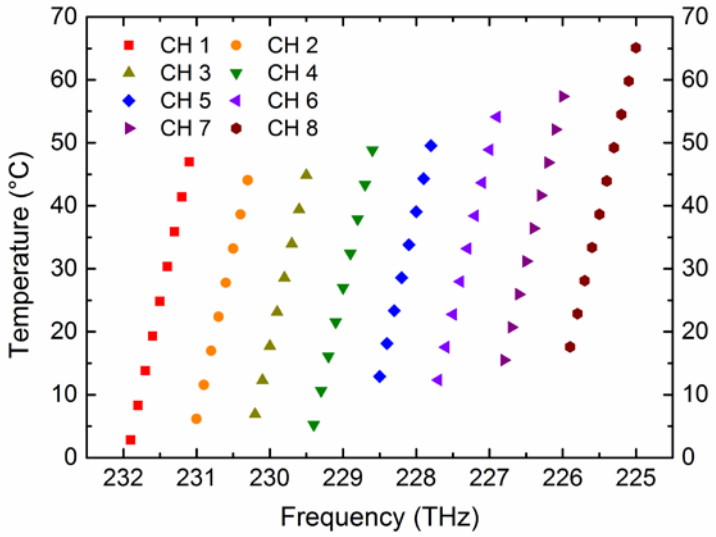

Figure 95. Detailed tuning temperature and channel switch frequency of the tunable laser array.

The average SMSR is 47.57 dB with a minimum of 43.23 dB at Channel 1 at 47 ºC (Figure 96).

In conclusion, an 8-wavelength monolithically integrated BH-DFB laser array with equivalent phase shifts was realized. The 1.3 μm DFB laser array with a 800 GHz wavelength grid achieved precise wavelength control, with a maximum wavelength deviation less than 9% of wavelength spacing. Uniformly good lasing characteristics were achieved under a wide range of injection currents and temperatures. It is also shown that the wavelength of an integrated DFB laser array can be continuously tuned over 70 channels with 100 GHz channel spacing, while maintaining a minimum output power of 9.8 mW. The proposed method offers a practical and cost-effective solution for the manufacture of high-performance, monolithic WDM DFB laser arrays as well as widely wavelength-tunable DFB lasers for integrated WDM systems.

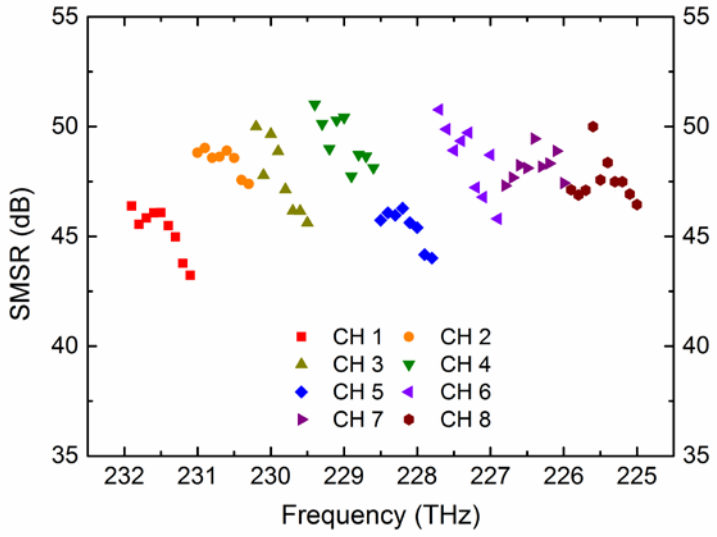

Figure 96. SMSR of all 70 frequencies of the tunable laser array. The average SMSR is 47.57dB with a minimum of 43.23 dB.

In conclusion, the 1.3 μm DFB laser array with a 800 GHz wavelength grid achieved precise wavelength control, with a maximum wavelength deviation less than 9% of wavelength spacing. Uniformly good lasing characteristics were achieved under a wide range of injection currents and temperatures. It is also shown that the wavelength of an integrated DFB laser array can be continuously tuned thermally over 40 nm, while maintaining a minimum SMSR and output power of 43.23 dB and 9.8 mW, respectively. The proposed method offers a practical and cost-effective solution for the manufacture of high-performance, monolithic WDM DFB laser arrays as well as widely wavelength-tunable DFB lasers for integrated WDM systems.

Chapter 7: Conclusion, Discussion and Perspective

7.1 CONCLUSION

This thesis mainly focused on the design and fabrication of Distributed Feedback Lasers and Integrated Laser Arrays for Wavelength-Division Multiplexing Systems.

Laterally Coupled DFB lasers with first-order sidewall gratings were realized by interference lithography for the first time. DFB lasers with a 2.6 μm wide ridge including 300 nm wide lateral gratings on both sidewalls of the ridge have been fabricated. They achieved CW lasing over a wide temperature range, a threshold current density of 1.7 kA/cm^2, and single longitudinal mode operation with a SMSR of 37 dB.

Then LC-DFB laser and LC-DFB laser arrays with equivalent phase shifts are proposed and demonstrated. The LC-DFB laser with equivalent quarter-wave phase shift operate in a single longitudinal mode over a very wide range of injection currents. A SMSR of 41.1 dB is achieved under a 100 mA DC bias. At room temperature (~25 ˚C), and under 100/200 mA bias current, a 14.0/23.5 mW optical output power is obtained. The LC-DFB laser array with EPS with 5 wavelength channels has been demonstrated. The lasing wavelength span is from 1545.57 nm to 1574.76 nm, with uniform wavelength spacing under 80 mA injection current. The threshold currents are from 24 mA to 29 mA, and the output power under 100 mA bias ranges from 11.4 mW to 14.1 mW. The average SMSR is 37.34 dB with a minimum of 32.33 dB.

For better performance, buried heterostructure DFB laser and laser arrays are also demonstrated using the same technology. A 6-wavelenth laser array with a 300 μm cavity length and a 8-wavelength laser array with 250 μm cavity length are successively

demonstrated with good performance. The BH laser arrays demonstrated uniformly good lasing characteristics achieved under a wide range of injection currents and temperatures. Also, it has been demonstrated that an 8-wavelength laser array can be continuously tuned over 70 channels with 100 GHz channel spacing, while maintaining a minimum output power and SMSR of 9.8 mW, and 43.23 dB, respectively.

The proposed method offers a practical and cost-effective solution for the manufacture of high-performance, monolithic WDM DFB laser arrays as well as widely wavelength-tunable DFB lasers for integrated WDM systems.

7.2 PERSPECTIVE

The works discussed in this thesis focused on the laser and laser arrays design and fabrication. In future works, the integration of more complex active devices and with passive devices can be investigated. The integration of one or more lasers with multiplexer, modulator, SOA, and monitors are all important research areas for photonic integrated circuits.

Appendix

FIRST AUTHOR JOURNAL PUBLICATIONS:

[1] Jingsi Li and Julian Cheng, "Laterally-coupled distributed feedback laser with Equivalent quarter wave phase shift," ***Optics Express***, 21, (22), pp. 26936–26941 (2013).

[2] Jingsi Li and Julian Cheng, "Laterally-coupled distributed feedback laser with first-order gratings by interference lithography," ***Electronics Letters***, 49, (12), pp. 764-766, 2013.

[3] Jingsi Li, Song, Tang, Jeffery Wang, Yue Liu, Xiangfei Chen, and Julian Cheng, "An Eight-Wavelength BH DFB Laser Array with Equivalent Phase Shifts for WDM Systems", ***IEEE Photonics Technology Letters***, In Press.

[4] Jingsi Li and Julian Cheng, "Monolithically-Integrated Wavelength-Multiplexed DFB Laser Array with Laterally-Coupled Quarter-Wave Phase-Shift Gratings defined by Interference Lithography", submitted.

FIRST AUTHOR CONFERENCE PAPERS:

[1] Jingsi Li, Song Tang, Jeffery Wang, Yue Liu, Haiming Xu, Qi Tang, Xiangfei Chen, and Julian Cheng, "Monolithic Buried Heterostructure DFB Laser Array for Integrated Optical Interconnects and WDM systems," ***OFC 2014***, Th3A.6, March 9 -13, 2014, San Francisco, USA.

[2] Jingsi Li and Julian Cheng, "Monolithic Single-Mode DFB Laser Array with Precise Wavelength Control for Opto-electronic Integration using an Equivalent Phase Shift Method," ***APS March Meeting 2013***, W21.00013, (2013).

Reference

[1] S. E. Miller, "Integrated optics- An introduction(Laser beam circuitry miniaturization facilitating laser circuit assembly isolation from thermal, mechanical and ambient changes)," *Bell System Technical Journal*, vol. 48, pp. 2059-2069, 1969.

[2] *Infinera Photonic Integration White Paper: Key to the Terabit Age*. Available: http://www.infinera.com/pdfs/whitepapers/Infinera-WP-Photonic_Integration.pdf

[3] I. P. Kaminow, "Optical integrated circuits: A personal perspective," *Journal of Lightwave Technology*, vol. 26, pp. 994-1004, 2008.

[4] A. Banerjee, Y. Park, F. Clarke, H. Song, S. Yang, G. Kramer, *et al.*, "Wavelength-division-multiplexed passive optical network (WDM-PON) technologies for broadband access: a review [Invited]," *Journal of optical networking*, vol. 4, pp. 737-758, 2005.

[5] D. K. Mynbaev and L. L. Scheiner, *Fiber-optic communications technology*: Prentice Hall New York, 2001.

[6] *ITU-T G.694.2 : Spectral grids for WDM applications: CWDM wavelength grid*. Available: http://www.itu.int/rec/T-REC-G.694.2

[7] *Motorola White Paper: WDM/CWDM/DWDM Segmentation Primer - Maximizing Capacity for Revenue*. Available: http://www1.arrisi.com/staticfiles/Video-Solutions/_Documents/static%20files/WDM%20CWDM%20DWDM%20Segmentation%20Primer.pdf

[8] J. Darja, M. J. Chan, M. Sugiyama, and Y. Nakano, "Four channel DFB laser array with integrated combiner for 1.55μm CWDM systems by MOVPE selective area growth," *IEICE Electronics Express*, vol. 3, pp. 522-528, 2006.

[9] *ITU-T G.694.1 : Spectral grids for WDM applications: DWDM frequency grid*. Available: http://www.itu.int/rec/T-REC-G.694.1

[10] M. Funabashi, H. Nasu, T. Mukaihara, T. Kimoto, T. Shinagawa, T. Kise, *et al.*, "Recent advances in DFB lasers for ultradense WDM applications," *Selected Topics in Quantum Electronics, IEEE Journal of*, vol. 10, pp. 312-320, 2004.

[11] H. Nasu, T. Mukaihara, T. Takagi, M. Oike, T. Nomura, and A. Kasukawa, "25-GHz-spacing wavelength-monitor integrated DFB laser module for DWDM applications," *Photonics Technology Letters, IEEE*, vol. 15, pp. 293-295, 2003.

[12] *IEEE 802.3ba Task Force: Compact Optical Multiplexers for LAN WDM*. Available: http://www.ieee802.org/3/ba/public/jul08/paatzsch_01_0708.pdf

[13] *Illustration of Wavelength-Division Multiplexing*. Available: http://www.fiber-optics.info/fiber_optic_glossary/dense_wavelength-division_multiplexing_dwdm

[14] L. A. Coldren. *Tunable Semiconductor Lasers -- a tutorial*. Available: http://ece.ucsb.edu/Faculty/Coldren/papers/TSL.pdf

[15] J. Buus and E. J. Murphy, "Tunable lasers in optical networks," *Journal of Lightwave Technology*, vol. 24, p. 5, 2006.

[16] H. Ishii, K. Kasaya, H. Oohashi, Y. Shibata, H. Yasaka, and K. Okamoto, "Widely wavelength-tunable DFB laser array integrated with funnel combiner," *Selected Topics in Quantum Electronics, IEEE Journal of*, vol. 13, pp. 1089-1094, 2007.

[17] B. Pezeshki, E. Vail, J. Kubicky, G. Yoffe, S. Zou, J. Heanue, *et al.*, "20-mW widely tunable laser module using DFB array and MEMS selection," *Photonics Technology Letters, IEEE*, vol. 14, pp. 1457-1459, 2002.

[18] *Online source, Chapter 12: Visible-spectrum LEDs*. Available: http://www.ecse.rpi.edu/~schubert/Light-Emitting-Diodes-dot-org/chap12/F12-06%20III-V%20bandgap%20energie.jpg

[19] M. Allovon and M. Quillec, "Interest in AlGaInAs on InP for optoelectronic applications," in *Optoelectronics, IEE Proceedings J*, 1992, pp. 148-152.

[20] C. Zhang, S. Liang, H. Zhu, B. Wang, and W. Wang, "A modified SAG technique for the fabrication of DWDM DFB laser arrays with highly uniform wavelength spacings," *Optics Express*, vol. 20, pp. 29620-29625, 2012.

[21] N. H. Zhu, H. G. Zhang, J. W. Man, H. L. Zhu, J. H. Ke, Y. Liu, *et al.*, "Microwave generation in an electro-absorption modulator integrated with a DFB laser subject to optical injection," *Optics Express*, vol. 17, pp. 22114-22123, 2009.

[22] Q. Lu, W. Guo, M. Nawrocka, A. Abdullaev, C. Daunt, J. O'Callaghan, *et al.*, "Single mode lasers based on slots suitable for photonic integration," *Optics Express*, vol. 19, pp. B140-B145, 2011.

[23] L. Hou, M. Haji, J. Akbar, J. H. Marsh, and A. C. Bryce, "AlGaInAs/InP monolithically integrated DFB laser array," *Quantum Electronics, IEEE Journal of*, vol. 48, pp. 137-143, 2012.

[24] T. Maruyama, T. Okumura, S. Sakamoto, K. Miura, Y. Nishimoto, and S. Arai, "GaInAsP/InP membrane BH-DFB lasers directly bonded on SOI substrate," *Optics Express,* vol. 14, pp. 8184-8188, 2006.

[25] H. Zhu, L. Ma, S. Liang, C. Zhang, B. Wang, L. Zhao, *et al.*, "InP based DFB laser array integrated with MMI coupler," *Science China Technological Sciences,* vol. 56, pp. 573-578, 2013.

[26] J. Li, H. Wang, X. Chen, Z. Yin, Y. Shi, Y. Lu, *et al.*, "Experimental demonstration of distributed feedback semiconductor lasers based on reconstruction-equivalent-chirp technology," *Optics Express,* vol. 17, pp. 5240-5245, 2009.

[27] Y. Takino, M. Shirao, N. Sato, T. Sato, T. Amemiya, N. Nishiyama, *et al.*, "Improved regrowth interface of AlGaInAs/InP-buried-heterostructure lasers by in-situ thermal cleaning," *Quantum Electronics, IEEE Journal of,* vol. 48, pp. 971-979, 2012.

[28] J. Kreissl, V. Vercesi, U. Troppenz, T. Gaertner, W. Wenisch, and M. Schell, "Up to 40 Gb/s directly modulated laser operating at low driving current: buried-heterostructure passive feedback laser (BH-PFL)," *Photonics Technology Letters, IEEE,* vol. 24, pp. 362-364, 2012.

[29] C.-L. Tsai, Y.-L. Chou, Y. Wang, S.-J. Chang, M.-C. Wu, and W. Lin, "1.3 μm Strain-Compensated InGaAsP Planar Buried Heterostructure Laser Diodes with a TO-Can Package for Optical Fiber Communications," *Journal of The Electrochemical Society,* vol. 156, pp. H903-H907, 2009.

[30] S. Park, S. Park, and J. Yu, "Fabrication and modulation characteristics of InGaAsP/InGaAsP MQW DCPBH lasers at λ∼ 1.57 μm," *Applied Physics B,* vol. 90, pp. 55-59, 2008.

[31] C.-L. Tsai, C.-T. Yen, C.-Y. Chou, S. Chang, and M.-C. Wu, "1.3-μm InGaAsP planar buried heterostructure laser diodes with AlInAs electron stopper layer," *Optics & Laser Technology,* vol. 44, pp. 1026-1030, 2012.

[32] H.-S. Kim, D. K. Oh, and I.-H. Choi, "Effect of p-doping profile on performance of strained InGaAs/InGaAsP multiple quantum well buried heterostructure laser diodes with Fe-or p/n/p-doped InP current blocking layer," *Materials Science and Engineering: B,* vol. 77, pp. 202-206, 2000.

[33] L. Miller, J. Verdeyen, J. Coleman, R. Bryan, J. Alwan, K. Beernink, *et al.*, "A distributed feedback ridge waveguide quantum well heterostructure laser," *Photonics Technology Letters, IEEE,* vol. 3, pp. 6-8, 1991.

[34] R. Martin, S. Forouhar, S. Keo, R. Lang, R. Hunsperger, R. Tiberio, *et al.*, "CW performance of an InGaAs-GaAs-AlGaAs laterally-coupled distributed feedback (LC-DFB) ridge laser diode," *Photonics Technology Letters, IEEE,* vol. 7, pp. 244-246, 1995.

[35] J. Viheriälä, J. Tommila, T. Leinonen, M. Dumitrescu, L. Toikkanen, T. Niemi, *et al.*, "Applications of UV-nanoimprint soft stamps in fabrication of single-frequency diode lasers," *Microelectronic Engineering,* vol. 86, pp. 321-324, 2009.

[36] H. Su and L. F. Lester, "Dynamic properties of quantum dot distributed feedback lasers: high speed, linewidth and chirp," *Journal of Physics D: Applied Physics,* vol. 38, p. 2112, 2005.

[37] S. Jang, J. Yu, and Y. Lee, "Laterally coupled DFB lasers with self-aligned metal surface grating by holographic lithography," *Photonics Technology Letters, IEEE,* vol. 20, pp. 514-516, 2008.

[38] K. Dridi, R. G. Maldonado-Basilio, A. Benhsaien, X. Zhang, and T. J. Hall, "Low-Threshold and Narrow Linewidth Two-Electrode MQW Laterally Coupled Distributed Feedback Lasers at 1550 nm," in *European Conference and Exhibition on Optical Communication*, 2012.

[39] M. Kamp, J. Hofmann, F. Schäfer, M. Reinhard, M. Fischer, T. Bleuel, *et al.*, "Lateral coupling–a material independent way to complex coupled DFB lasers," *Optical Materials,* vol. 17, pp. 19-25, 2001.

[40] V. Tolstikhin, C. Watson, K. Pimenov, R. Moore, Y. Logvin, and F. Wu, "Laterally coupled DFB lasers for one-step growth photonic integrated circuits in InP," *Photonics Technology Letters, IEEE,* vol. 21, pp. 621-623, 2009.

[41] J. Telkkala, J. Viheriala, A. Aho, P. Melanen, J. Karinen, M. Dumitrescu, *et al.*, "Narrow linewidth laterally-coupled 1.55 μm DFB lasers fabricated using nanoimprint lithography," *Electronics Letters,* vol. 47, pp. 400-401, 2011.

[42] K. Adachi, K. Shinoda, D. Kawamura, T. Kitatani, Y. Matsuoka, T. Sugawara, *et al.*, "Multiple-wavelength 25-Gb/s surface-emitting laser array for short-reach WDM links," in *Lasers and Electro-Optics (CLEO), 2011 Conference on*, 2011, pp. 1-2.

[43] T. L. Koch, "OFC tutorial: III-V and silicon photonic integrated circuit technologies," in *Optical Fiber Communication Conference and Exposition (OFC/NFOEC), 2012 and the National Fiber Optic Engineers Conference*, 2012, pp. 1-45.

[44] B. Pezeshki and G. Yoffe, "High performance laser arrays for tunable and parallel link applications," in *Proceedings of SPIE, the International Society for Optical Engineering*, 2008, pp. 69090B. 1-69090B. 5.

[45] C. Zah, F. Favire, B. Pathak, R. Bhat, C. Caneau, P. Lin, *et al.*, "Monolithic integration of multiwavelength compressive-strained multiquantum-well distributed-feedback laser array with star coupler and optical amplifiers," *Electronics Letters*, vol. 28, pp. 2361-2362, 1992.

[46] G. Li, T. Makino, A. Sarangan, and W. Huang, "16-Wavelength gain-coupled DFB laser array with fine tunability," *Photonics Technology Letters, IEEE*, vol. 8, pp. 22-24, 1996.

[47] T. Cockerill, R. Lammert, D. Forbes, M. Osowski, and J. Coleman, "Twelve-channel strained-layer InGaAs-GaAs-AlGaAs buried heterostructure quantum well laser array for WDM applications by selective-area MOCVD," *Photonics Technology Letters, IEEE*, vol. 6, pp. 786-788, 1994.

[48] R. Nagarajan, M. Kato, J. Pleumeekers, P. Evans, S. Corzine, S. Hurtt, *et al.*, "InP photonic integrated circuits," *Selected Topics in Quantum Electronics, IEEE Journal of*, vol. 16, pp. 1113-1125, 2010.

[49] L. A. Coldren, S. W. Corzine, and M. L. Mashanovitch, *Diode lasers and photonic integrated circuits* vol. 218: Wiley. com, 2012.

[50] K. Sekartedjo, N. Eda, K. Furuya, Y. Suematsu, F. Koyama, and T. Tanbun-Ek, "1.5 μm phase-shifted DFB lasers for single-mode operation," *Electronics Letters*, vol. 20, pp. 80-81, 1984.

[51] W. K. Chan, J. Chung, and R. J. Contolini, "Phase-shifted quarter micron holographic gratings by selective image reversal of photoresist," *Applied Optics*, vol. 27, pp. 1377-1380, 1988.

[52] K. Utaka, S. Akiba, K. Sakai, and Y. Matsushima, "λ/4-shifted InGaAsP/InP DFB lasers by simultaneous holographic exposure of positive and negative photoresists," *Electronics Letters*, vol. 20, pp. 1008-1010, 1984.

[53] B. Eggleton, P. Krug, L. Poladian, and F. Ouellette, "Long periodic superstructure Bragg gratings in optical fibres," *Electronics letters*, vol. 30, pp. 1620-1622, 1994.

[54] X.-f. Chen, Y. Luo, C.-c. Fan, T. Wu, and S.-z. Xie, "Analytical expression of sampled Bragg gratings with chirp in the sampling period and its application in dispersion management design in a WDM system," *Photonics Technology Letters, IEEE*, vol. 12, pp. 1013-1015, 2000.

[55] Y. Dai, X. Chen, L. Xia, Y. Zhang, and S. Xie, "Sampled Bragg grating with desired response in one channel by use of a reconstruction algorithm and equivalent chirp," *Optics letters,* vol. 29, pp. 1333-1335, 2004.

[56] Y. Dai, X. Chen, D. Jiang, S. Xie, and C. Fan, "Equivalent phase shift in a fiber Bragg grating achieved by changing the sampling period," *Photonics Technology Letters, IEEE,* vol. 16, pp. 2284-2286, 2004.

[57] J. Sun, C. W. Holzwarth, and H. I. Smith, "Phase-Shift Bragg Grating in Silicon Using Equivalent Phase-Shift Method," *Photonics Technology Letters, IEEE,* vol. 24, pp. 25-27, 2012.

[58] J. Sun, E. S. Hosseini, J. D. Bradley, T. N. Adam, G. Leake, D. Coolbaugh, *et al.*, "Uniformly spaced λ/4-shifted Bragg grating array with wafer-scale CMOS-compatible process," *Optics Letters,* vol. 38, pp. 4002-4004, 2013.

[59] J. Li, Y. Cheng, Z. Yin, L. Jia, X. Chen, S. Liu, *et al.*, "A multiexposure technology for sampled Bragg gratings and its applications in dual-wavelength lasing generation and OCDMA en/decoding," *Photonics Technology Letters, IEEE,* vol. 21, pp. 1639-1641, 2009.

[60] H. Kogelnik and C. Shank, "Coupled - Wave Theory of Distributed Feedback Lasers," *Journal of Applied Physics,* vol. 43, p. 2327, 1972.

[61] J.-S. Huang, "Design-in Reliability for Modern Wavelength-division Multiplex (WDM) Distributed Feedback (DFB) InP Lasers," *Applied Physics Research,* vol. 4, p. p15, 2012.

[62] B. Broberg and S. Lindgren, "Refractive index of InGaAsP layers and InP in the transparent wavelength region," *Journal of Applied Physics,* vol. 55, p. 3376, 1984.

[63] P. Martin, L. Chusseau, C. Alibert, and H. Bissessur, "Accurate refractive index measurements of doped and undoped InP by a grating coupling technique," *Applied Physics Letters,* vol. 67, p. 881, 1995.

[64] F. Fiedler and A. Schlachetzki, "Optical parameters of InP-based waveguides," *Solid-state electronics,* vol. 30, pp. 73-83, 1987.

[65] C. P. Fucetola, H. Korre, and K. K. Berggren, "Low-cost interference lithography," *Journal of Vacuum Science & Technology B: Microelectronics and Nanometer Structures,* vol. 27, pp. 2958-2961, 2009.

[66] J. Zhao, X. Chen, N. Zhou, K. Qian, L. Wang, X. Huang, *et al.*, "Experimental demonstration of a 16-channel DFB laser array based on nanoimprint technology," *Semiconductor Science and Technology,* vol. 28, p. 055015, 2013.

[67] H. van Wolferen and L. Abelmann, "Laser Interference Lithography," in *Lithography: Principles, Processes and Materials.*, ed Hauppauge NY, USA: Nova Publishers, 2011, pp. 133-148.

[68] H.-C. Kim, H. Kanjo, T. Hasegawa, S. Tamura, and S. Arai, "1.5-μm wavelength narrow stripe distributed reflector lasers for high-performance operation," *Selected Topics in Quantum Electronics, IEEE Journal of,* vol. 9, pp. 1146-1152, 2003.

[69] J. Wang, J.-B. Tian, P.-F. Cai, B. Xiong, C.-Z. Sun, and Y. Luo, "1.55-μm AlGaInAs-InP laterally coupled distributed feedback laser," *Photonics Technology Letters, IEEE,* vol. 17, pp. 1372-1374, 2005.

[70] J. Coleman, "The development of the semiconductor laser diode after the first demonstration in 1962," *Semiconductor Science and Technology,* vol. 27, p. 090207, 2012.

[71] A. Laakso, M. Dumitrescu, J. Viheriälä, J. Karinen, M. Suominen, and M. Pessa, "Optical modeling of laterally-corrugated ridge-waveguide gratings," *Optical and quantum electronics,* vol. 40, pp. 907-920, 2008.

[72] *Cauchy's Equation*. Available: http://en.wikipedia.org/wiki/Cauchy's_equation

[73] J. Li and J. Cheng, "Laterally-coupled distributed feedback laser with first-order gratings by interference lithography," *Electronics Letters,* vol. 49, 2013.

[74] J. Li and J. Cheng, "A laterally-coupled distributed feedback laser with equivalent quarter-wave phase shift," *Optics express,* vol. 21, pp. 26936-26941, 2013.

[75] J. McCaulley, V. Donnelly, M. Vernon, and I. Taha, "Temperature dependence of the near-infrared refractive index of silicon, gallium arsenide, and indium phosphide," *Physical Review B,* vol. 49, p. 7408, 1994.

[76] J. E. Whiteaway, G. Thompson, A. J. Collar, and C. J. Armistead, "The design assessment of λ/4 phase-shifted DFB laser structures," *Quantum Electronics, IEEE Journal of,* vol. 25, pp. 1261-1279, 1989.

[77] K. Otsubo, M. Matsuda, K. Takada, S. Okumura, M. Ekawa, H. Tanaka, *et al.*, "Uncooled 25 Gbit/s direct modulation of semi-insulating buried-heterostructure 1.3 μm AlGaInAs quantum-well DFB lasers," *Electronics Letters,* vol. 44, pp. 631-632, 2008.

[78] K. Otsubo, M. Matsuda, K. Takada, S. Okumura, M. Ekawa, H. Tanaka, *et al.*, "1.3um AlGaInAs Multiple-Quantum-Well Semi-insulating Buried-Heterostructure Distributed-Feedback Lasers for High-Speed Direct Modulation,"

Selected Topics in Quantum Electronics, IEEE Journal of, vol. 15, pp. 687-693, 2009.

[79] K. Takemasa, M. Kubota, T. Munakata, and H. Wada, "1.3-μm AlGaInAs buried-heterostructure lasers," *Photonics Technology Letters, IEEE,* vol. 11, pp. 949-951, 1999.

[80] S. Pralgauskaite, J. Matukas, V. Palenskis, G. Letal, R. Mallard, and S. Smetona, "Low-frequency noise and quality prediction of MQW buried-heterostructure DFB lasers," in *Advanced Optical Devices, Technologies, and Medical Applications*, 2003, pp. 85-93.

[81] W. Z. Jie, C. S. Jin, Z. Fan, W. X. Jie, W. Wei, and W. R. Han, "Native-oxidized InAlAs blocking layer buried heterostructure InGaAsP-InP MQW laser for high-temperature operation," *Photonics Technology Letters, IEEE,* vol. 11, pp. 3-5, 1999.

[82] J. Matukas, V. Palenskis, Č. Pavasaris, E. Šermukšnis, J. Vyšniauskas, S. Pralgauskaitė, *et al.*, "Optical and electrical characteristics of InGaAsP MQW BH DFB laser diodes," in *Materials science forum*, 2002, pp. 91-96.

[83] I. Mito, M. Kitamura, K. Kobayashi, S. Murata, M. Seki, Y. Odagiri, *et al.*, "InGaAsP double-channel-planar-buried-heterostructure laser diode (DC-PBH LD) with effective current confinement," *Lightwave Technology, Journal of,* vol. 1, pp. 195-202, 1983.

[84] M. Hirao, A. Doi, S. Tsuji, M. Nakamura, and K. Aiki, "Fabrication and characterization of narrow stripe InGaAsP/InP buried heterostructure lasers," *Journal of Applied Physics,* vol. 51, p. 4539, 1980.

[85] J. Li, S. Tang, J. Wang, Y. Liu, X. Chen, and J. Cheng, "Monolithic Buried Heterostructure DFB Laser Array for Integrated Optical Interconnects and WDM systems," in *Optical Fiber Communication Conference*, San Francisco, California, 2014, p. Th3A.6.